11-13-2019

High Power and Optomechanics in Advanced LIGO Detectors

Terra Christine Hardwick

Louisiana State University and Agricultural and Mechanical College

Recommended Citation

Hardwick, Terra Christine, "High Power and Optomechanics in Advanced LIGO Detectors" (2019). *LSU Doctoral Dissertations*. 5107.
https://digitalcommons.lsu.edu/gradschool_dissertations/5107

HIGH POWER AND OPTOMECHANICS IN ADVANCED LIGO DETECTORS

A Dissertation

Submitted to the Graduate Faculty of the
Louisiana State University and
Agricultural and Mechanical College
in partial fulfillment of the
requirements for the degree of
Doctor of Philosophy

in

The Department of Physics & Astronomy

by
Terra Hardwick
B.S. Physics, University of Oregon, 2014
B.S. Mathematics, University of Oregon, 2014
December 2019

Acknowledgments

Gaby, my advisor, for paving the way and for leading broadly and personally.

Robert S., for introducing me to *Atta cephalotes* and LIGO and for being my role model in all aspects of life.

Daniel S., for pushing me to think deeper, eat better, hike slower, and for pizza nights and all the relationships grown there.

Brian O., for being my daily advisor and advocate.

Peter F., for demonstrating an incredible attention to detail that never loses sight of the larger picture.

The leaders around me who have demonstrated immense discipline and passion for one's work and offered me assistance at all levels: Valera F., Joe G., Catherine D., R. Rau, Geoff C., and many others.

Anamaria, for being my mentor and friend from day one, and for letting me clean up cables even when you knew there was no point.

The commissioners at all four sites who were colleagues, teachers, and friends all in one. Adam, Marie, Evan H., Corey, Arnaud, Shiva, TVo, Sheila, Jenne, Nutsinee, Craig, Dan B., Keiko, Annalisa, Aidan, Danny, Jeff, Gautam, and so many others. Thank you for your guidance, wisdom, patience, arguments, game nights, and adventures. 80 hour weeks in the control room and I still want to go get a drink with you after.

Shania, Graeme, Tyler, Guillermo, Alex, and so many other LSU colleagues that made my time there enjoyable.

Kelsie, for steady friendship, deep wisdom, and the next stage of our lives in a new city.

Ali, for our late-blooming friendship that has become invaluable to me. Your perspective, conversations, and laughs have helped me through difficult decisions and the darkest days. Also: Charlie.

Erin, for being my best friend, homework buddy, adventure partner, and lifting bro for over 5 years now. You are a constant inspiration and joy to me; grad school without you

would've been lame. If you kick hard enough, the gators wont come near you.

Nadia, for constant joy and companionship and for being the most adorable cockroach killing machine.

Mom, for teaching me from childhood that boredom is unnecessary, for setting a precedent of constant striving for more from life, and for the deep value of selflessness and genuine interest in others. Dad, for introducing me to logical thought and the reality of grey areas, for patiently debating me during all stages of life, and for the precedent of balancing a dedicated work ethic with the greater scope of life. To both of you, for growing a vegetable garden in the suburbs, for fostering dinner conversations that covered all topics, and for giving me space to grow beyond any gender norm box.

Jamie, for every day. For growth, for time, for debate, for coffee stops around the world, for mountain tops and waterfall pools. For everything. And for pulling me through.

Table of Contents

Abstract

In September 2015, a new era of astronomy began with the first direct detection of gravitational waves from a binary black hole coalescence. The event was captured by the Laser Interferometer Gravitational-wave Observatory, comprised of two long-baseline interferometers, one in Livingston, LA and one in Hanford, WA. At the time of the first detection, the interferometers were part way through an upgrade to an advanced configuration and were operating with a strain sensitivity of just better than $10^{-23}/\mathrm{Hz}^{1/2}$ around 100 Hz. The full Advanced LIGO design calls for sensitivity of a few parts in $10^{-24}/\mathrm{Hz}^{1/2}$.

This thesis covers the detector upgrade to double the input power, thereby reducing quantum shot noise, which currently limits LIGO strain sensitivity above 100 Hz. First, it presents the design of the interferometer and the noises – fundamental, technical, and environmental – which contribute to the full sensitivity curve, motivating the need for high power. The details of the high power laser upgrade are discussed. Second, it presents select side effects of high power, which can result in overall losses and heighten specific classical noise couplings. The work particularly focuses on a three-mode opto-mechanical interaction that can become unstable at high power, threatening the operational ability of the detector; multiple successful mitigation technique are presented and compared.

The results of this work, combined with the collaborative work of many others, allow the Advanced LIGO detectors to achieve a strain sensitivity better than $5 \times 10^{-24}/\mathrm{Hz}^{1/2}$ during the third observation run.

1 Introduction

Regular detection of gravitational waves requires extremely sensitive instruments that are stable over long periods of time. The Advanced LIGO detectors have achieved a length displacement sensitivity better than $2 \times 10^{-20}\,\mathrm{m/Hz^{1/2}}$, several orders of magnitude smaller than the width of a proton and sufficient to detect gravitational waves from binary black holes and neutron stars. Currently in the third observing run together with the Virgo detector, the gravitational-wave detector network has at least two eyes on the sky at least 80% of the time.

While the detectors are subject to a host of noises that cause length displacement and sensing limitations, their sensitivity is fundamentally limited by quantum uncertainty. In particular, Advanced LIGO is limited by uncertainty in photon counting statistics at the output photo-diodes (shot noise) above 100 Hz. Increasing laser power decreases shot noise and theoretically provides an immediate strain sensitivity improvement. To generate increased power, an upgrade of the laser system was necessary; this successfully resulted in 50 W input power available to the interferometer for the third observing run.

The optical topology of the Advanced LIGO design amplifies the input power to ∼270 kW circulating power in the arms. Such high power brings strong thermal consequences. Even with low absorption, the mirrors that form the arm cavities distort with the central heat load, altering their effective radius of curvature. Changing cavity parameters effect mode matching between the coupled cavities of the interferometer and increase laser noise coupling to the gravitational-wave readout. Thermal compensation must be tuned to optimize optical gain and decrease noise couplings. High power also increases the rate and severity of a three-mode opto-mechanical interaction that can become unstable and render the detector inoperable. Effective mitigation strategies must be found that don't add excess noise.

In Chapter 2, we provide an overview of gravitational radiation generation and detection. The optical topology of a ground-based interferometer for gravitational-wave detection is built up, culminating with the Advanced LIGO detectors. Detector noise is discussed, including quantum noise which fundamentally limits the detector sensitivity. The need for higher laser power to increase sensitivity is understood. Chapter 3 lays out the laser power amplification system the author and others installed and commissioned to increase power during the third observing run. Measurements the author performed to quantify and reduce ambient motion and laser jitter noise from the new system are also reviewed. In Chapter 4, we introduce high power thermal effects in the interferometer, specifically deformation of the test masses due to the increased heat load and the subsequent mode mismatch between the coupled cavities of the interferometer. The relationship between thermal lensing and laser noise coupling is established. The hardware system in place to compensate these effects is reviewed, followed by results of the author's work implementing the system for decreasing laser noise coupling with high power. The chapter ends with a new compensation system the author and others installed and tested to shape the output beam. In Chapter 5, we introduce an optomechanical instability that can occur with high power circulating in the interferometer. The theory of three-mode parametric instability is introduced, followed by the various mitigation schemes the author and others have implemented over the past few years; this work comprises a large bulk of the thesis. Chapter 6 travels outside of the LIGO detector to Caltech's 40 m prototype interferometer. The author and others develop and carry out an experiment to measure the relationship between mirror surface deformations and cavity mode content. While the analysis is still underway, the motivation, experimental set-up, and initial results are included for future reference. Lastly, Chapter 7 summarizes these findings.

2 Gravitational Waves and LIGO

In this chapter, we review the basics of general relativity and gravitational waves. We build up the optical topology necessary for interferometer gravitational-wave detectors sensitive and stable enough for regular event detection. We introduce the Advanced LIGO detectors and discuss noises that set or pollute their fundamental sensitivity.

2.1 Gravitational waves in general relativity

When describing space, it's easiest to first imagine it as 3-dimensional and flat (straight and stiff) in each dimension. In this picture, the space interval ds between any two points is defined straightforwardly as

$$ds^2 = dx^2 + dy^2 + dz^2 \tag{2.1}$$

where x, y, z are the three spacial dimensions. This is called Euclidean space. To then include time, we need to add a fourth dimension t. If the speed of light is constant, then now our space interval is defined as

$$ds^2 = -c^2dt^2 + dx^2 + dy^2 + dz^2. \tag{2.2}$$

This is called Minkowski space-time and is used in the Special Theory of Relativity. To then incorporate gravity, we no longer restrain space-time to be flat; rather it curves with the presence of matter, and the space-time interval is not so simple. Such is the case in the General Theory of Relativity.

Fortunately, for the purposes of this paper, we don't have to go far beyond the niceness of Minkowski space-time. Imagine instead that the straightness of space wiggles a bit. If the wiggle is small enough, then we can just write this as a perturbation to the flat space-time above and remain in the linear regime. First lets rewrite eq. 2.2 in Einstein notation:

$$ds^2 = \eta_{\mu\nu}dx^\mu dx^\nu \tag{2.3}$$

$$\eta_{\mu\nu} = \begin{pmatrix} -c^2 & 0 & 0 & 0 \\ 0 & 1 & 0 & 0 \\ 0 & 0 & 1 & 0 \\ 0 & 0 & 0 & 1 \end{pmatrix} \tag{2.4}$$

Then a small perturbation to this would simply be

$$ds^2 = (\eta_{\mu\nu} + h_{\mu\nu} + O([h_{\mu\nu}]^2))dx^\mu dx^\nu = g_{\mu\nu} dx^\mu dx^\nu \tag{2.5}$$

where $g_{\mu\nu}$ is the metric and $|h_{\mu\nu}| << 1$ tells us the curvature of local space-time (relative to the totally flat Minkowski metric $\eta_{\mu\nu}$).

Ultimately our goal is to find solutions to the Einstein field equations, which describe the relationship between mass and its gravitational effect. If we assume the metric given in eq. 2.5 and we impose the transverse-traceless gauge condition (only spacial components are non-zero and sum of the diagonal components is zero) –

$$h_{\mu\nu} = \begin{pmatrix} 0 & 0 & 0 & 0 \\ 0 & a & b & 0 \\ 0 & b & -a & 0 \\ 0 & 0 & 0 & 1 \end{pmatrix} \tag{2.6}$$

– then the field equations in vacuum reduce (from very complicated) to a simple wave equation

$$\left(\nabla^2 - \frac{1}{c^2}\frac{\partial^2}{\partial t^2}\right) h_{\mu\nu} = 0. \tag{2.7}$$

Thus much like the analogous electromagnetic field, eq. 2.7 has gravitational-wave solutions where the gravitational plane wave traveling in the z direction has metric perturbations of the form

$$h_{\mu\nu} = \Re[A_0 e^{-i\omega(t-z)} e_{p\mu\nu}] \tag{2.8}$$

where A_0 is amplitude and p can be $+$ or $\times$ such that $\boldsymbol{e}_+ \equiv \boldsymbol{e}_\times \otimes \boldsymbol{e}_\times - \boldsymbol{e}_y \otimes \boldsymbol{e}_y$ and $\boldsymbol{e}_\times \equiv \boldsymbol{e}_\times \otimes \boldsymbol{e}_y - \boldsymbol{e}_y \otimes \boldsymbol{e}_\times$. Interpreting this, gravitational waves propagate at the speed of light deforming space-time transversely to the direction of propagation with two independent modes of polarization with amplitudes a and b that deform at 45-degrees with respect to one another [1] [2].

2.2 Astrophysical sources of gravitational waves

Gravitational radiation is generated by the time-varying gravitational quadrupole moment $I_{\mu\nu}$,

$$h_{\mu\nu} = \frac{2G}{Rc^4}\ddot{I}_{\mu\nu}, \tag{2.9}$$

where R is the distance from the source to the detector, i.e. accelerating matter with broken spherical or cylindrical symmetries. Thus a perfectly spherical black hole (or star) does not radiate but a binary system does. LIGO is only sensitive enough to measure gravitational radiation from very massive objects. A summary of gravitational wave sources studied by LIGO is outlined below:

Stochastic background

A large number of independence and unresolved sources produce a random continuous gravitational-wave background spectrum with a roughly constant amplitude [3]. Part of this background comes from the superposition of the gravitational radiation emitted from the background compact binary population. Additionally, according to the inflation model, a large number of gravitational-waves were produced approximately 10^{36} to 10^{32} seconds after the Big Bang. As the waves would then stretch during the following expansion of the universe, the stochastic background would provide information about the early stages of the universe.

Pulsars

An axisymmetric pulsar rotating with a near-constant frequency emits gravitational radiation that can be considered monochromatic. These neutron stars have a rotational period ranging from from a few seconds to a few milliseconds; only a small fraction (~ 350) could be detected within the LIGO frequency band. Gravitational radiation emitted by pulsars is of order

$$h \sim \frac{4\pi^2 G}{Rc^4} \epsilon I \omega^2 \tag{2.10}$$

where ϵ is the equatorial ellipticity (a measure of the relative deformation from symmetric) and ω is the rotational angular frequency [1]. To date, gravitational-waves from pulsars have not been detected, but upper limits on parameters have been set [4] [5].

Bursts

Short transient signals ($<1\,\mathrm{s}$) such as those from supernovae have been observed by electromagnetic and neutrino observatories; such event sources are expected to produce gravitational waves as well [6]. The shape of the waveform is not fully predictable, as it depends on the mass distribution and signal frequency of the exploding star; detection relies on multiple gravitational-wave and electromagnetic or gamma ray detector coincidences. The supernova event rate in a Milky Way-type galaxy is expected to be of order $10^{-2}\,\mathrm{yr}^{-1}$.

Compact binary systems

As two compact objects orbit around their common center of mass, they radiate gravitational-waves. As they lose energy, their orbital radius decreases and their orbital frequency increases, resulting in a 'chirp'-like gravitational waveform. Compact binary systems can consist of two black holes, two neutron stars, or a mix. If we consider a simple binary system source consisting of two masses m_1 and m_2 in a circular orbit in the $x-y$ plane, then the components of the quadrupole moment are

$$I_{xx} = \mu r^2 cos^2(\omega t), I_{yy} = \mu r^2 sin^2(\omega t), I_{xy} = I_{yx} = \mu r^2 cos(\omega t) sin(\omega t) \tag{2.11}$$

where $\mu = \frac{m_1 m_2}{m_1 + m_2}$, $\omega = 2\pi f_{orbital}$, r is the radius of the orbit, and I_{zz} is a constant. This yields the second time derivatives

$$\ddot{I}_{xx} = -Acos(2\omega t), \ddot{I}_{yy} = Acos(2\omega t), \ddot{I}_{xy} = \ddot{I}_{yx} = -Asin(\omega t) sin(2\omega t) \tag{2.12}$$

where $A = 2\mu r^2 \omega^2$ [1]. As a simple example, consider a binary neutron star system ($m_1 = m_2 = 1.4M\odot$, $r = 20km$, $f_{orbital} = 400Hz$) in the Virgo Cluster ($R \approx 15Mpc$, where $1Mpc = 3.262 \times 10^6$ light-years). Then $h \approx 1 \times 10^{-21}$ [1].

2.3 Interferometric gravitational-wave detectors

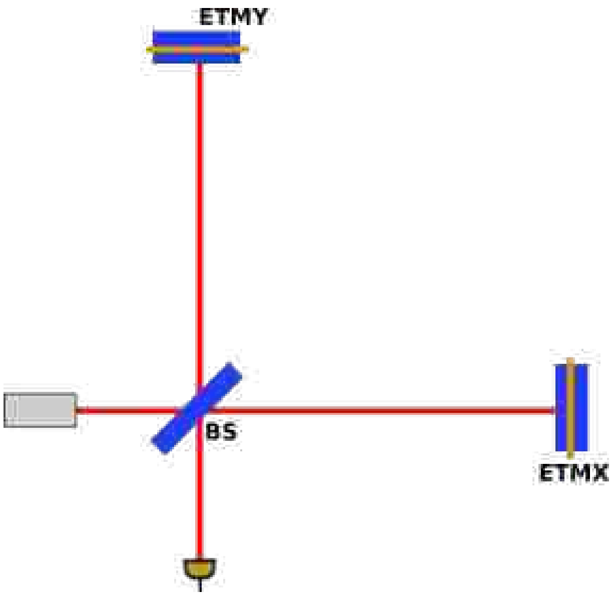

Figure 2.1. Michelson interferometer with end test masses and a photodiode at the antisymmetric output port.

Long-baseline interferometer gravitational-wave detectors have been developed to measure these small fluctuations in space-time. They utilizes the fact that the speed of light is constant even as space-time deforms: the arms of the interferometer act as a ruler in space-time and the travel time of light in the interferometer tells us how this ruler changes. As a gravitational wave passes through the earth, it will stretch and compress space-time, including the interferometer arms. However, the light traveling in the arms continues at the same speed, so the round trip travel time of the light in each arm will be longer or shorter as that arm is stretched or compressed.

For example, consider a simple Michelson interferometer, consisting of an input beam, a beam splitter, and two simple non-cavity arms. A gravitational wave with + polarization and traveling in the direction orthogonal to both arms, with a sinusoidal metric perturbation h_+, would simultaneously stretch one arm of this interferometer while equally compressing the other arm. The difference between the phase of light hitting a photodiode at the anti-symmetric port from the beam which traveled in one arm compared to the other arm will be

$$\Delta\phi = h_+ \frac{4\pi L}{\lambda} \tag{2.13}$$

where L is the length of the interferometer arm, λ is the wavelength of the gravitational wave, and we've assumed $h_+(t) \approx h_+$. If the interferometer arm length is much smaller than the gravitational wavelength, then the arm length difference is proportional to the metric perturbation, $\Delta L = h_+ L$.

The following sections build up the optical topology of an interferometer gravitational-wave detector and, along the way, define some concepts used throughout the rest of this thesis. A detailed discussion has already been presented by many, but in particular the presentation by Hall [7] and Martynov [8] are referenced here.

2.3.1 Michelson interferometer

Again consider a simple Michelson with a beam splitter (BS) and two highly reflective end test masses (ETMs) at the end of each arm. A laser is injected via the input (symmetric) port; this laser has frequency $\omega_0/2\pi$ and field amplitude E_0. The light traveling in each arm picks up a round-trip phase $\phi_{X,Y} = 2\omega_0 l_{X,Y}/c$, where l_X, l_Y refer to the length of each

Michelson arm, respectively. Defining $\phi_\pm = (\phi_X \pm \phi_Y)/2$, then the field at the output (antisymmetric) port is

$$\begin{aligned} E_{AS} &= \frac{E_0}{2}(e^{i\phi_X} - e^{i\phi_Y}) \\ &= iE_0 e^{i\phi_-}\sin(\phi_-) \end{aligned} \tag{2.14}$$

and power at the antisymmetric port is

$$\begin{aligned} P_{AS} &= |E_{AS}|^2 \\ &= P_0 \sin^2\phi_- \\ &\approx P_0(\phi_-)^2 \end{aligned} \tag{2.15}$$

Thus, the photodiode at the output port senses the differential arm length signal. A similar argument can be made showing that the signal common to both arms appears only at the symmetric port. This is referred to as common-mode rejection (as common phase fluctuations are not seen at the gravitational-wave readout) and is referred to throughout this work.

2.3.2 Fabry-P$\acute{e}$rot michelson

From equations 2.13 and 2.15, we see that sensitivity of the detector is improved by longer arms L and greater power P_0. Additionally, the signal is improved if it is linearly responsive to differential arm motion, as opposed to the quadratic relationship in Eq. 2.15. In this section, we walk through cavity dynamics and how the addition of input test masses (ITMs) to create a Fabry-Pérot cavity in each arm effectively lengthens the arm and increases the circulating power, enhancing the gravitational wave effect. Additionally, we introduce cavity control techniques that result in a linear control signal and hold the interferometer at a stable, controlled operating point.

Optical cavity response

An optical cavity is defined by its length L and the reflectively (and transmissivity) of the optics forming it, r_a and r_b (and t_a, t_b). The field circulating in a cavity pumped by E_1 is

$$E_{circ}(\omega) = E_1(\omega)\frac{t_a}{1 - r_a r_b e^{2i\omega L/c}}. \tag{2.16}$$

Resonance occurs periodically, when $e^{2i\omega L/c} = 1$; the spacing between successive resonances is the free spectral range (FSR), where $f_{FSR} = c/2L$. On resonance, the cavity gain is

$$G = \left(\frac{|t_a|}{1 - r_a r_b}\right)^2. \tag{2.17}$$

. The finesse $\mathcal{F}$ of a cavity is a measure of the width of the resonance relative to the FSR:

$$\begin{aligned} \mathcal{F} &= \frac{f_{FSR}}{f_{FWHM}} \\ &= \frac{\pi(r_a r_b)^{1/2}}{1 - r_a r_b} \end{aligned} \tag{2.18}$$

where f_{FWHM} is the full-width half-max frequency of the resonance.

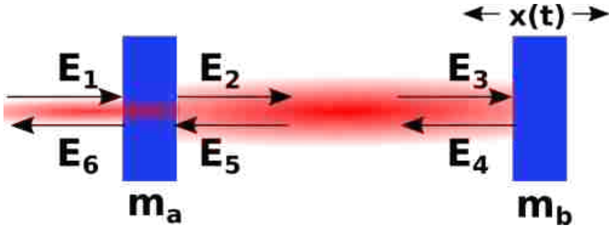

Figure 2.2. Simple cavity with labeled fields.

To consider the frequency response of a cavity to a gravitational-wave signal, we can consider the relative motion between the mirrors as a sinusoidal signal $x(t) = x_0\cos(\omega_s t)$ applied to one mirror m_b. The field reflected from m_b is

$$\begin{aligned} E_4 &= -r_b E_3 e^{-2ikx(t)} \\ &= -r_b E_3 - 2\pi\frac{x_0}{\lambda}(e^{-i\omega_s t} + e^{i\omega_s t})E_3 \end{aligned} \tag{2.19}$$

where we've assume $x_0 \ll \lambda$. Thus we see that a sinusoidal perturbation on a test mass creates sidebands at the perturbation frequency on the cavity field. The cavity response is characterized by its cavity pole $f_p = c/4L\mathcal{F}$; a sideband with a frequency below the cavity pole experienced optical gain, while frequencies above the pole are filtered out by the cavity.

Cavity sensing and control

In order to measure such small changes in length from a gravitational-wave, the cavity length must be kept otherwise constant relative to the laser frequency. The laser frequency can be locked to the cavity length using the Pound-Drever-Hall (PDH) control scheme, in which input light is RF phase-modulated and the error signal is made by demodulating the cavity's reflected field [7].

If light from the laser is phase modulated at $f_{RF} = \Omega/2\pi$ with modulation depth Γ, then the field incident on the cavity is

$$\begin{aligned} E_1 &= E_0 e^{\omega t + \Gamma \sin\Omega t} \\ &\approx E_0[J_0(\Gamma)e^{i\omega t} + J_1(\Gamma)e^{i(\omega+\Omega)t} - J_1(\Gamma)e^{i(\omega-\Omega)t}] \end{aligned} \tag{2.20}$$

where the exponential was expanded in terms of the Bessel functions J_0 and J_1. Thus we've written the input beam in terms of the carrier and two sidebands at $(\omega \pm \Omega)/2\pi$. Assuming the carrier is resonant in the cavity and the sidebands are not, then the reflected power, demodulated at the same f_{RH}, can be shown to be an error signal linearly proportional to δL:

$$\epsilon \propto \sqrt{P_c P_s}\frac{\mathcal{F}}{\lambda}\delta L \tag{2.21}$$

where $P_{c,s}$ is the power in the carrier and sidebands, respectively.

2.3.3 Dual-recycled Fabry-P$\acute{e}$rot michelson

The interferometer is operated near a dark fringe, controlled to where the beams coming back from the two arms nearly perfectly interfere and most of the returning light is directed back towards the symmetric port. Thus the sensitivity is further enhanced by placing a partially transmitting mirror between the laser and beamsplitter, creating the power recycling cavity (PRC) formed by the power recycling mirror (PRM) and ITMs. This recaptured light increased the power incident on the beamsplitter by the power recycling gain factor. This also narrows the arm linewidth for common-mode signals, thus passively filtering laser noises.

A signal recycling mirror (SRM) is placed between the beamsplitter and the gravitational-wave readout. Sidebands arising from differential displacement of the arms are transmitted to the antisymmetric port while the carrier field is reflected to the symmetric port; the presence of the SRM creates an additional recycling cavity seen only by the sidebands. The detector frequency response can be shaped by tuning the length of this signal recycling cavity with the tuning phase is given by

$$\phi_{SRC} = kl_{SRC} + \frac{\pi}{4} \tag{2.22}$$

where l_{SRC} is the cavity length (SRM$\leftrightarrow$ ITM). If $\phi_{SRC} = 0$, the detector bandwidth is increased, but optical gain is decreased. If $\phi_{SRC} = \pi/2$, low frequency sensitivity is increased, but at the cost of a narrowed bandwidth.

2.4 Laser Interferometer Gravitational-wave Observatory

The Laser Interferometer Gravitational-Wave Observatory (LIGO) consists of two dual-recycled Fabry Michelson interferometer detectors, LIGO Livingston Observatory (LLO) and LIGO Hanford Observatory (LHO). After a series of upgrades from their initial configuration, the second generation Advanced LIGO (aLIGO) detectors came online for the first observing run (O1) in September 2015 through January 2016 [9]. On September 14, 2015, LIGO made the first direct detection of gravitational waves from a black hole coalescence, GW150914 [10]. The system consisted of two black holes of about 30 solar masses each, which merged about 400 Mpc away.

During the rest of O1 and the second observing run (O2), 11 events in total were detected, including the first detection of gravitational waves from a binary neutron star inspiral. The full catalog of O1, O2 events is published in [11]. At the time of this writing, dozens of gravitational-wave candidates have been reported during the first half of O3, started April 2019 [12].

2.4.1 Advanced LIGO topology

The optical configuration of the LIGO interferometer optimizes strain sensitivity for gravitational wave detection between 10 Hz - 5 kHz, achieving a sensitivity around $5\times10^{-24}/\sqrt{\mathrm{Hz}}$ during O3. In LIGO, this strain sensitivity is often referred to as DARM (differential arm motion). A schematic of the main components of the aLIGO topology is shown in Fig. 2.4. A thorough discussion of the aLIGO optical parameters and detailed motivations behind the choices are found in [13] and [7].

Advanced LIGO utilizes a Nd:YAG 1064 nm laser; prior to O3, an additional amplification stage was installed to bring the power injected into the symmetric port >40 W (see Chpt. 3). The full aLIGO configuration calls for 125 W input power. For frequency stabilization, the laser is PDH-locked to three different optical cavities in series. First, the laser is stabilized to a 20.3 cm long reference cavity on the laser table, then to the suspended input mode cleaner (IMC) ring cavity. Finally, the laser is locked to the common-mode arm length. For intensity stabilization, an error signal from the pre-modecleaner (PMC) bowtie cavity and from the IMC are fed back to an acousto-optic modulator (AOM) in the high power laser path [7]. The PMC and IMC also filter laser pointing noise, polarization, and input beam shape.

The Fabry-Pérot arm cavities are approximately 4 km long. The transmissivity ($T_{\mathrm{ITM}} = 1.4\%$) of the ITMs are chosen such that the aLIGO Fabry-Pérot arm cavities have $\mathcal{F}_a = 450$,

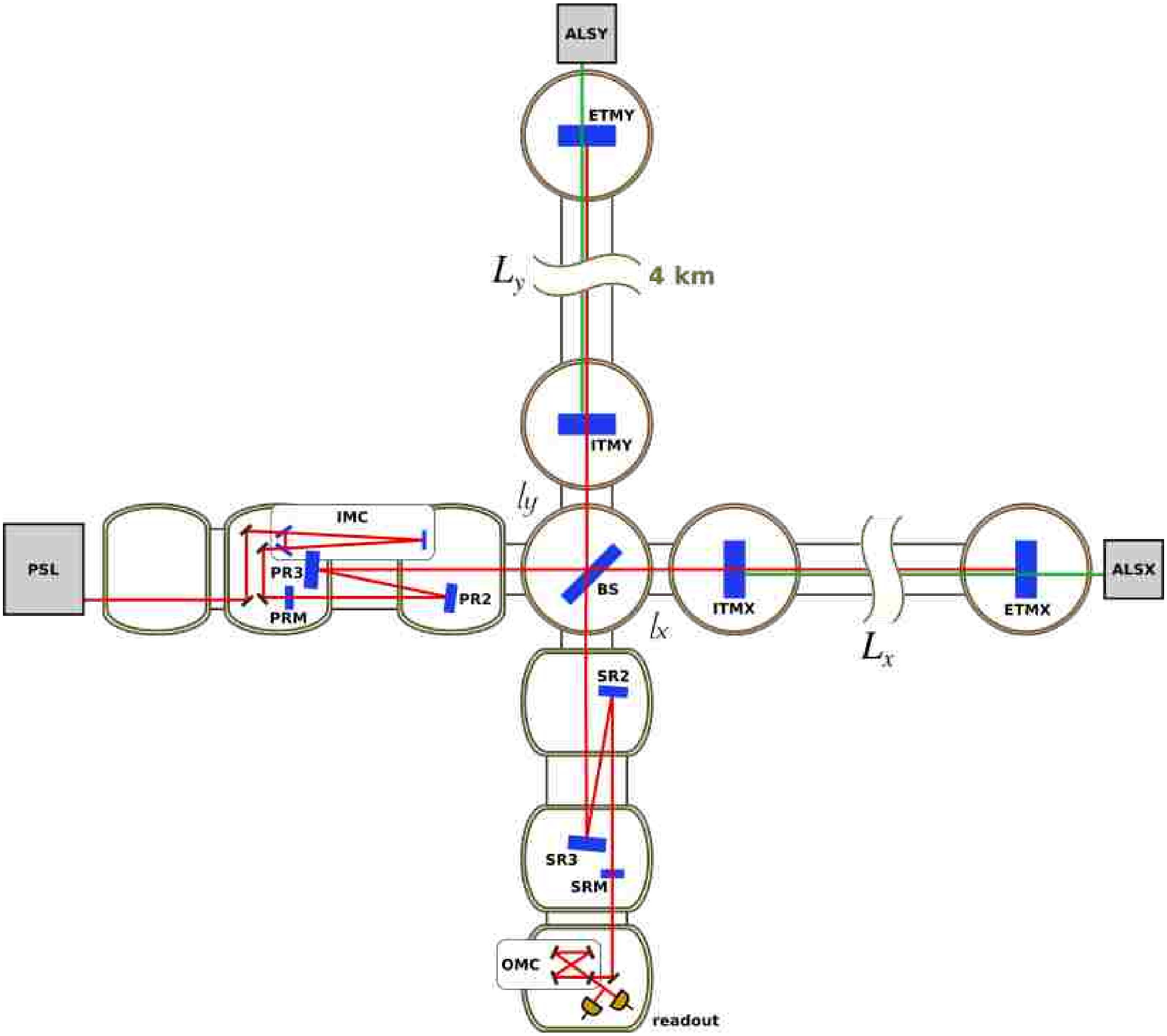

Figure 2.3. Layout of Advanced LIGO optical path. Pre-stabilized laser (PSL) light passes through the input mode cleaner (IMC) and the power recycling cavity (PRC; formed between the power recycling mirror - PRM - and input test masses) before impinging on the beam splitter (BS). The split beam travels through the respective input test mass (ITM) and resonates in the 4 km arm cavity formed by the input test mass (ITM) and end test mass (ETM). The two beams recombine at the BS and pass through the signal recycling cavity (SRC; formed between the signal recycling mirror - SRM - and the input test masses) and output mode cleaner (OMC). The beam transmitted through the OMC hits two photodiodes, which are the final gravitational wave signal readout. An auxiliary laser system (ALS) on each arm injects green light for lock acquisition assistance. Core components are housed within a vacuum system (double outline) and reside on optics tables with active seismic isolation within individual chambers.

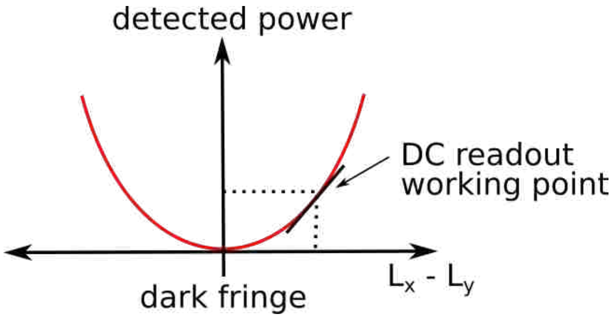

Figure 2.4. Advanced LIGO DC readout scheme.

cavity pole $f_a = 42\,\mathrm{Hz}$, providing an arm cavity optical gain ~ 270. The power recycling cavity gives an additional gain ~ 40.

To have individual sensing and control for the arms and recycling cavities, two sets of radio frequency sidebands are generated such that one set – at $f_1 = 9.1\,\mathrm{MHz}$ – resonate in the PRC and another set – at $f_2 = 45.5\,\mathrm{MHz}$ – resonate in the SRC. The short arms l_x and l_y are intentionally held at different lengths by l_S, where l_S is a macroscopic length offset ($0.8\,m >> \lambda_{laser}$) called the Schnupp asymmetry; this allows for transmission of control sidebands to the antisymmetric port. Macroscopic cavity lengths are chosen such that both sidebands are non-resonant in the arm cavities, the carrier and f_1 sidebands are simultaneously resonant in the PRC, and the f_1 sidebands are non-resonant in the SRC. The length of the IMC is chosen such that the f_1 RF sideband resonates.

On the output side, between the SRM and the gravitational-wave readout, the output mode cleaner (OMC) filters out unwanted spacial and frequency components of the light prior to the gravitational-wave readout photodiodes.

Advanced LIGO employs a 'dc readout' scheme [14] [9]. A microscopic differential arm length ($\sim$10 pm) is introduced, allowing a small amount of carrier light to leak to the antisymmetric port. The laser field impinging on the OMC contains the carrier, the audio-band gravitational-wave sidebands, the radio frequency control sidebands, and carrier light that is not mode-matched to the arm cavities. The radio frequency sidebands used for auxiliary cavity control are filtered out by the output mode cleaner. From Eq. 2.19, we see that a gravitational-wave modulates the carrier field in the arms by ω_s; these sidebands *are* transmitted through the OMC and directly modulate the power on the readout photodiodes with the gravitational-wave signal. The dc readout detection is advantageous as the carrier is filtered by the arm cavities, removing high frequency noise.

2.5 Noise in LIGO detectors

The signal at the output of the detector is a sum of the gravitational-wave signal $h(t)$ and noise $n(t)$. The sum of all noises as a function of frequency that creates a differential length readout signal defines the strain sensitivity curve for the detectors. Noise sources can be classified as fundamental, technical, and environmental. Fundamental noises - quantum and thermal - are calculated from first principles and, short of major upgrades, set the design sensitivity for the detector. Advanced LIGO design calls for technical noises (control loops, electronics, charge, etc.) and environmental noises (seismic, acoustic, magnetic, etc.) to contribute less than fundamental noises, but in practice noises and noise couplings can be high enough to pollute the fundamental strain sensitivity. The coupling contribution of each noise to the gravitational-wave readout is found by directly measuring or modeling the noise spectrum via an auxiliary witness sensor, then multiplying this spectrum by the measured or modeled transfer function between the witness sensor and DARM. Advanced LIGO noises during O1 have been previously discussed in [7] [13] [8]. For the purposes of this work, we split the noise discussion into quantum and classical noises.

A noise budget is a collection of modeled or measured strain caused by all known noise sources. The sum of the noise budget strain spectra components can be compared to design and measured. A LLO noise budget at the start of O3 is shown in Fig. 2.5. A fundamental noise budget for the same time is shown in Fig. 2.6.

2.5.1 Quantum noise

Quantum noise arises from the fundamental uncertainty in the vacuum field entering the unused (i.e. antisymmetric) ports of the interferometer [15]. It can be understood as

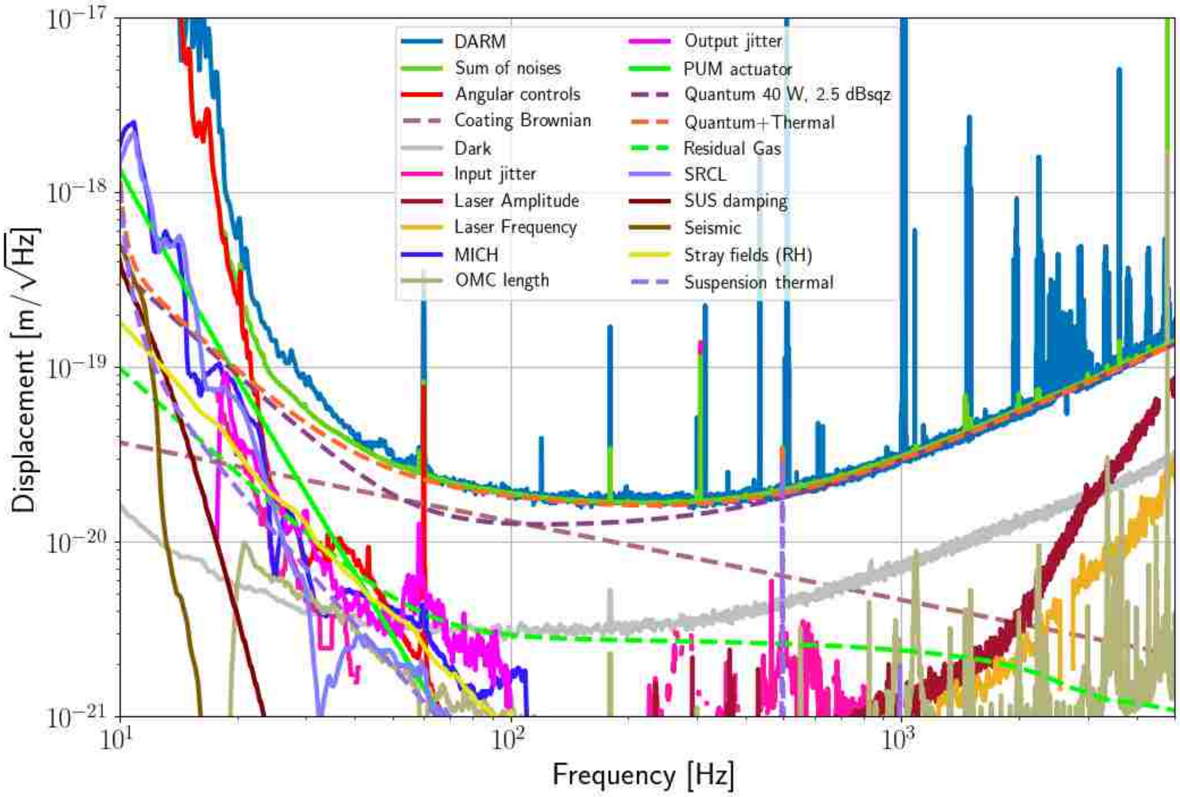

Figure 2.5. LLO noise budget at the start of the third observing run, including fundamental and known technical and environmental noises.

contributions of shot noise and radiation pressure noise

$$h_q(f) = \sqrt{h^2_{shot}(f) + h^2_{rp}(f)}. \tag{2.23}$$

The following sections will introduce both and discuss the upgrades that can be made to reduce quantum noise in different frequency regions.

Quantum noise coupling is amplified and shaped by the coupled cavity response of the interferometer. In particular, it depends on gains of various cavities G_{cav} and on the response

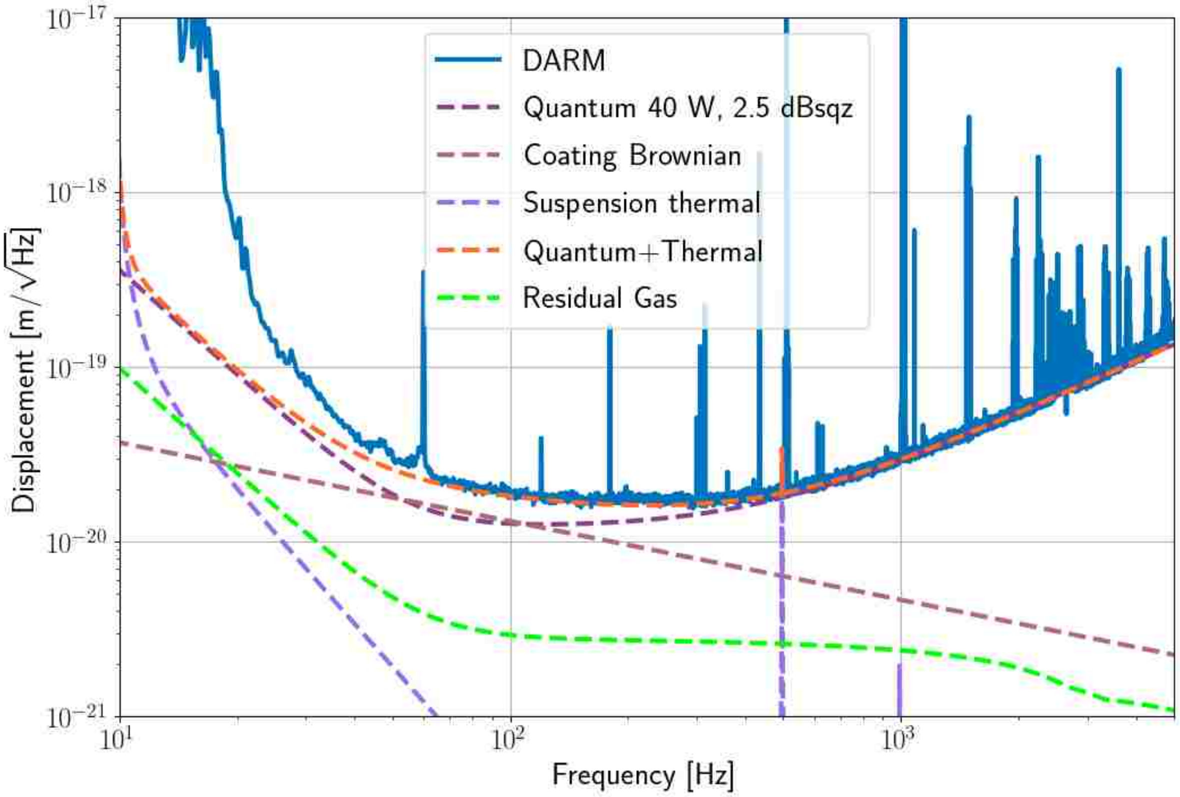

Figure 2.6. LLO fundamental noise budget at the start of the third observing run.

$\mathcal{K}_-$ to the differential coupled cavity pole f_-:

$$\mathcal{K}_-(f) = \frac{f_-}{if + f_-} \tag{2.24}$$

Shot noise

Statistical variations in photon arrival time result in phase variations of the field. This results in fluctuations of the power impinging on the readout photodiodes: while the average number of photons hitting the photodiodes at a given time is fixed, they follow a Poisson statistic. This effect - known as photon shot noise - causes power fluctuations of

$$\sigma_{power} = \sqrt{n_{photons}} = \sqrt{\frac{\lambda\tau}{4\pi\hbar c}P} \tag{2.25}$$

where τ is the interval over which the number of photons is averaged. Considering the full interferometer, this fluctuation in power - calibrated in effective strain - has strain noise

$$h_{shot}(f) = \frac{\lambda}{4\pi G_{arm}}\sqrt{\frac{2h\nu G_{SRC}}{G_{PRC}P_{in}\eta}} \times \frac{1}{\mathcal{K}_{-}(f)} \tag{2.26}$$

where η accounts for loss between the output beam and the photodiodes and in the photodiodes themselves [13]. Shot noise in inversely proportional to the square root of the power; increasing the laser power – as well as the optical gain of the arm cavities and the PRC – reduces the shot noise contribution. From Fig. 2.5, we see that aLIGO is currently limited at high frequency by shot noise.

Radiation pressure

As photons hit the test mass, they exert a force on it, imparting momentum and causing a recoil reaction. Variations in photon arrival time (as discussed above) cause variations in this force:

$$\sigma_{force} = \frac{1}{c}\sigma_{power} \tag{2.27}$$

The fluctuations in force variably move the test mass, injecting noise into the final length readout. This radiation pressure noise is given by

$$h_{rp}(f) = \frac{2}{cM\pi^2 f^2}\sqrt{h\nu G_{-}P_{arm}} \times \mathcal{K}_{-}(f) \tag{2.28}$$

where M is the mass of the test mass, ν is the laser carrier frequency, and G_{-} is the differential coupled cavity build up [13].

Note that this is frequency dependent, where the slope is set by the pendulum response

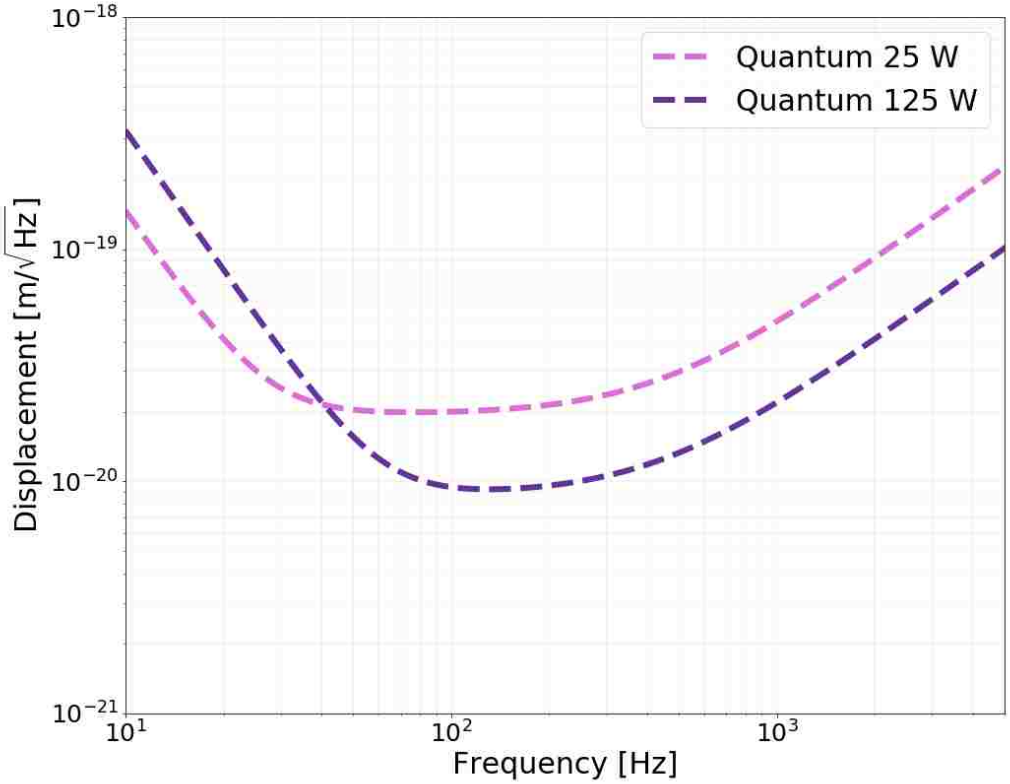

Figure 2.7. Quantum noise at two different input power levels; shot noise reduces as the square root of power, while radiation pressure increases with the square root of power. The crossover sits around 100 Hz.

of the test mass suspension ($1/f^2$), dominating the strain sensitivity at low frequency. Radiation pressure is inversely proportional to the mass M of the test mass, so heavier test masses decrease radiation pressure contribution. Unlike shot noise, radiation pressure noise increases as the square root of the power. The amplitude spectral density of the combined quantum noise at different powers is shown in Fig 2.7. However, from Fig. 2.5, we see that other noises currently dominate over quantum noise at low frequency; an increase in power would immediately increase sensitivity above 60 Hz but would not significantly add noise at lower frequencies.

Squeezing

As previously mentioned, quantum noise is fundamentally explained by quantum vacuum fluctuation. These vacuum fluctuations have an amplitude and phase relationship:

$$\sigma_{amp}\sigma_{phase} \geq \frac{\hbar}{2} \tag{2.29}$$

such that there is a limit on the combined decrease of amplitude and phase noise. The quantum noise floor is where $\sigma_{amp}\sigma_{phase} = \frac{\hbar}{2}$; the combined fluctuations of amplitude and phase are as low as possible. Squeezing works on the principle that either can be reduced at the cost of raising the other: phase noise (shot noise) can be lowered if amplitude noise (radiation pressure noise) is raised and vice versa.

As LIGO is currently limited only by shot noise at high frequency, phase squeezing was implemented for both LLO and LHO for O3. Nominal operation sees 2.7 dB of squeezing at LLO - increasing the expected detection rate by 50% - and 2.0 dB, 40% at LHO during the first half of the run. The maximum squeezing observed was 3.2 dB. A full discussion can be found in [16].

2.5.2 Classical noise

A summary of classical noises contributing to aLIGO sensitivity follows. Hardware and control systems designed to address each noise source are discussed along the way, with upgrades prior to O3 specifically highlighted.

Laser frequency and intensity

As discussed, high power is advantageous to reduce shot noise limited strain. Common mode rejection along with multiple stages of frequency and intensity noise stabilization nominally suppress laser noise to well below design sensitivity. However, mismatches in arm power and input test mass effective lenses can increase laser noise coupling to impactful

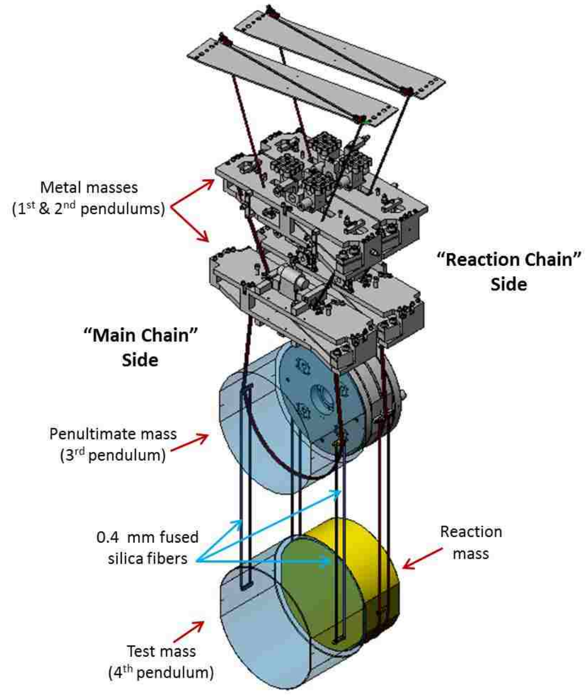

Figure 2.8. Quadruple test mass and reaction mass suspension system. Figure from [17].

levels. Further discussion in Chpts. 3 and 4.

Jitter

Laser pointing and beam size fluctuations cause jitter on the input beam. Input beam interaction with the resonant motion of input steering mirrors can induce jitter peaks that pollute DARM between 200 - 600 Hz. Further discussion in Chpt. 3.

Seismic

On average, the ground moves $\times 10^{10}$ more than design sensitivity at 10 Hz [18]. Quadruple pendulum suspension systems (see Fig. 2.8) provide $1/f^8$ passive isolation for the test masses and the active seismic isolation platforms on which the pendulums are mounted provide three more orders of isolation up to 10 Hz. This isolation provides enough attenuation such that the interferometer can remain stable enough for cavity controls during nominal conditions. However, there is still significant displacement noise at low frequencies above fundamental sensitivity levels.

Newtonian

Fluctuation in local gravity fields close to the test mass can exert force on the test mass and couple to the gravitational wave readout. Gradient fluctuations can come from ground motions, nearby structures vibrating, or fluctuations in atmospheric pressures [19]. Newtonian noise is expected to limit design sensitivity between 10 - 20 Hz, though other noise sources currently dominate in this range.

Thermal

The aLIGO test masses are 40 kg polished fused silica cylinders suspended by fused silica fibers from identical penultimate masses. Silica (SiO2) and titania-doped tantala (Ta2O5) are deposited onto the HR surface of the test masses as low noise reflective coatings. Brownian thermal noise in the high-Q fiber suspensions couples to the test mass length displacement. Active feedback to the penultimate mass is used to damp the fiber resonances but residual motion (kT) creates peaks in the DARM strain around 500 Hz and harmonics. Of the thermal noise in the test mass, Brownian noise in the coatings – particularly the doped tantula – dominates. Direct measurements of noise in mirror samples with the same coatings predict coating thermal noise to limit aLIGO between 10 - 500 Hz [20]. Further discussion in Chpt. 5.

Electric charge

To control the test masses, aLIGO employs a second suspension system directly behind the test mass suspension to serve as a reaction mass system; see Fig. 2.8. The lowest suspension stage (i.e. the test mass) is controlled with low-noise electrostatic actuation. Non-uniform residual additional electrostatic charge results in coupling between voltage fluctuations around the test mass and longitudinal test mass motion.

Residual gas

Gas molecules inside the vacuum system couple in two ways: they hit the test mass and impart momentum to it, and they scatter light as they drift through the beam path. The former is amplified by the 5 mm gap between the test mass and reaction mass due to squeezed film damping below 100 Hz [21]. Prior to O3, the reaction masses were replaced with annular reaction masses, decreasing the gas noise contribution below 100 Hz (where the squeezed film damping noise dominated). Scatter from gas molecules has a flat noise spectrum (up to a cutoff) that depends on the density of molecules, type of molecule, and beam size [22].

Controls

aLIGO has 7 length and 20 angular degrees of freedom which are sensed interferometrically [23]. Angular motion in particular is difficult to control; radiation-pressure induces torque, creating power-dependent test mass motion coupling. Feedback control loops for auxiliary degrees of freedom can reinject sensing noise and couple directly to DARM. Residual current in photodiodes (dark noise), ADCs, DACs, and whitening boards all contribute noise nominally below quantum noise.

Scatter

Light that strays from the main beam path and backscatters off of non-seismically isolated components (beam tube wall, etc.) can re-enter the main beam and introduce significant phase and amplitude noise. Since O2, a large number of baffles have been installed to catch stray light. Anthropomorphic-driven scatter continues to impact DARM sensitivity between 20 - 200 Hz during the day. Additionally, prior to O3 the end test mass coatings had a spiral pattern with up to 1 nm variation in coating height, inducing increased scatter off of the

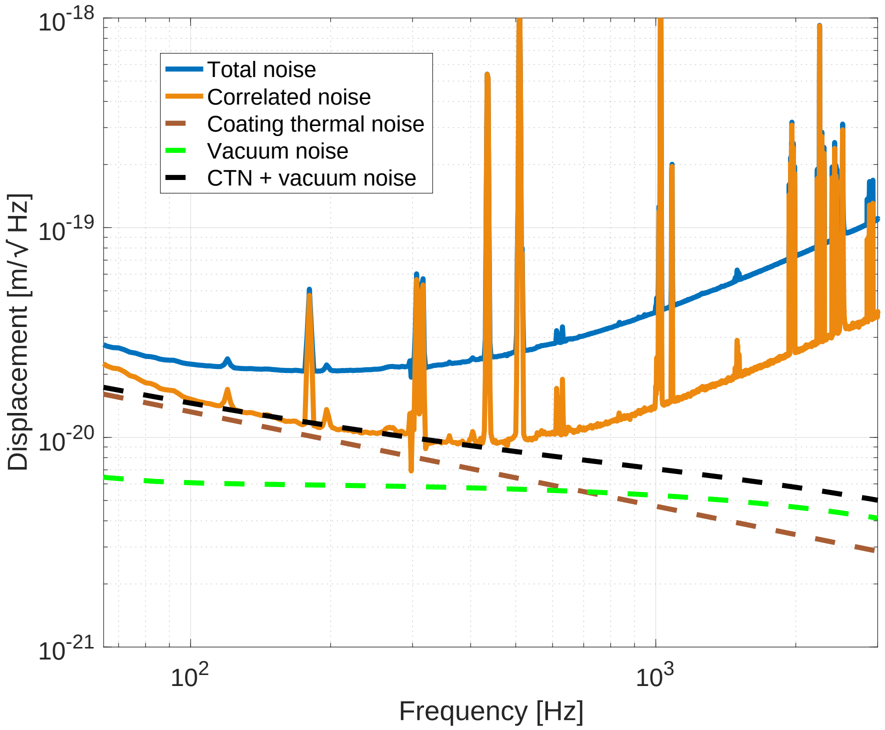

Figure 2.9. Total noise (DARM) and correlated noises (cross-spectral density) at the start of O3 at LLO. Also shown are vacuum (residual gas) noise and coating thermal noise. The classical noise sensitivity is limited by the sum of vacuum and coating noise between 100 - 400 Hz. Coating thermal noise is from [20] and vacuum noise is adjusted to account for a leak present in the vacuum system at the time. High frequency correlated noise is limited by laser frequency noise and cross-spectrum integration time.

mirror surface. The optics were replaced by new ETMs that are coated more uniformly, effectively increasing the power buildup in the arms by 10%.

2.5.3 Cross correlation

As the aLIGO strain sensitivity spectrum is limited by quantum noise at high frequencies ($>$ 100 Hz), the classical noise spectrum is not directly visible. The so-called cross correlation technique can be used to remove shot and dark noise contributions from the spectrum and reveal the classical noise buried underneath. A detailed description of the technique was first presented in [24].

The beam transmitted through the OMC is split between two photodiodes that read out the gravitational-wave signal. The shot and dark noise on each of these photodiodes is uncorrelated, while all other noises (classical and radiation pressure) arriving from the interferometer are common to both. The cross power spectral density $S_{AB}(f)$ of PD_A and PD_B gives an estimate of the spectrum of correlated interferometer noise. Given two series x_A and y_A, the cross spectral density is

$$S_{AB}(f) = \int_{-\infty}^{\infty} \left[\int_{-\infty}^{\infty} x(\tau) \cdot y(\tau + t) d\tau \right] e^{-ift/2\pi} dt. \tag{2.30}$$

Fig. 2.9 shows LLO DARM and cross spectral density at the start of O3. By removing the shot noise, we are able to reveal the classic noise limit and compare to measured and modeled fundamental noises.

3 High Power Input

As we saw in Sec. 2.5.1, LIGO is limited by shot noise at high frequency; this strain sensitivity limit can be reduced by $\sqrt{P}$ with higher power P. This chapter discusses the testing, installation, and results of the high power amplifier installed prior to O3. Testing and installation was completed by the author and A. Spencer under the lead of LLO laser engineer M. Heintze. Noise investigations, including jitter coupling characterization and reduction, was led by the author, with assistance from other commissioners and input from R. Schofield.

3.1 70 W amplifier

The 25 W input power of the second observing run (O2) was the maximum power available from the laser configuration at that time. This consisted of an InnoLight© NPRO 2 W output laser seeding a 35 W amplifier. The original Advanced LIGO high power plan was to send the 35 W output into a high power oscillator capable of producing 200 W output. During O2, the LHO detector ran using this high power oscillator (though tuned to only output 30 W) while LLO used just the NPRO + 35 W amplifier.

The high power oscillator injected beam pointing and beam size jitter noise into the LHO interferometer. Noise originated from the water system cooling the oscillator crystals; water flow is necessarily turbulent for efficient cooling. Water, brought in from removed chillers, is directed via a breakout manifold under the table and travels to the oscillator in tubes along the optic table. Water flows in a closed loop directly over the oscillator crystals in series with auxiliary cooled dumps, etc. Water motion couples into the beam in two ways: turbulent water flow over the crystals couples directly into the beam, and water flow shaking the optics table couples into optics and thus indirectly into the beam.

The noise concerns of the high power oscillator, combined with a laser incident rendering the LLO oscillator indefinitely inoperable, motivated the design of an alternative high power source.

To double the available input power between O2 and O3, a solid-state amplifier has

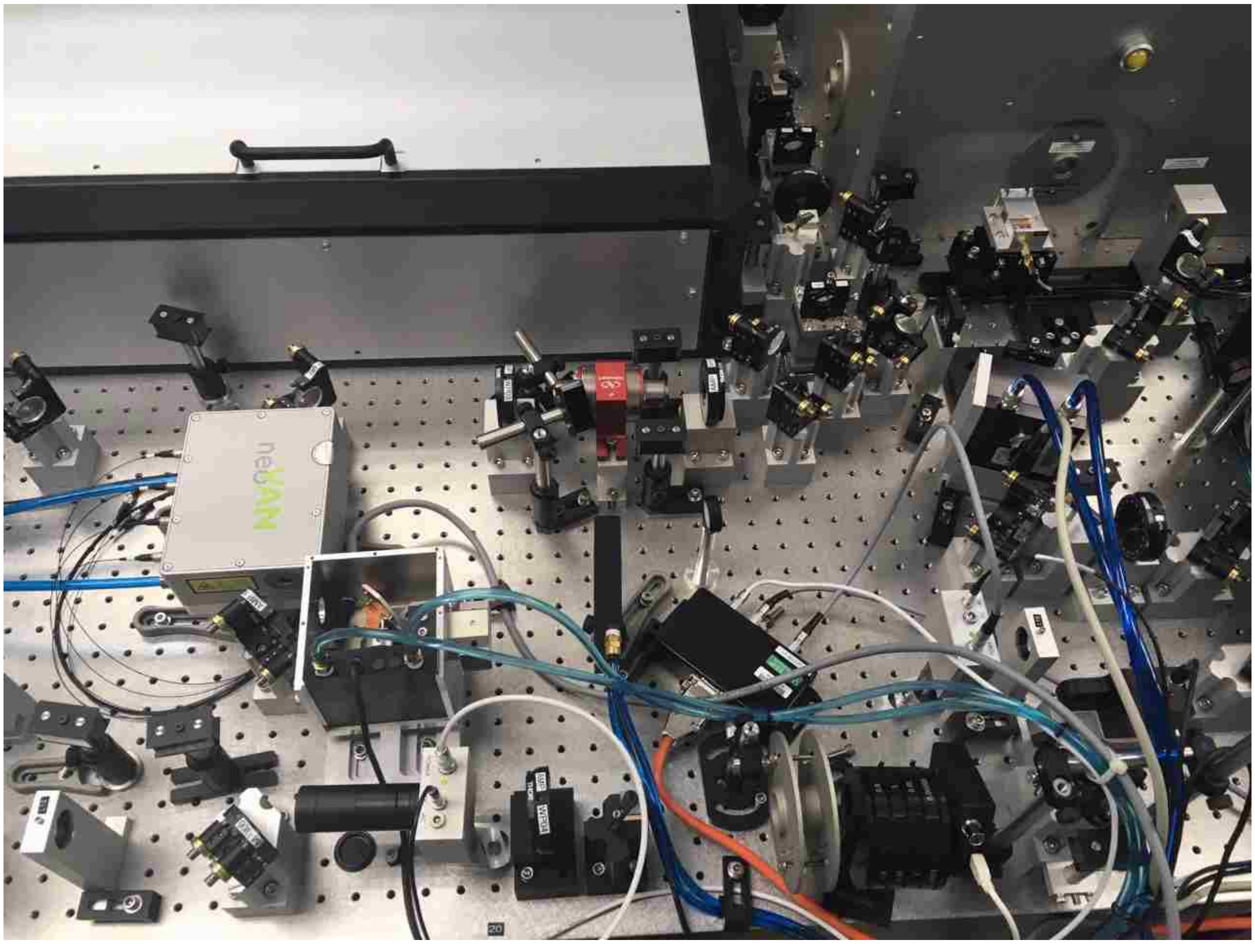

Figure 3.1. neoLASE© 70W amplifier (center left with green text label) in place on LIGO's laser table during installation. The large box in the top left of the picture contains the NPRO and 35 W amplifier; the box in the top right contains the old-style high power oscillator.

been installed capable of amplifying the 35 W beam to 80 W of optical power. The installed neoLASE© neoVan 70 W laser amplifier - Fig. 3.1 - is a solid-state system with 4 crystals pumped by fiber-coupled diode lasers specifically designed for minimum-impact integration into the LIGO table set-up and for quiet operation. The crystals are cooled indirectly: rather than water flowing over them, the crystals sit on a metal plate under which the water flows. The complete water system is designed in parallel such that the highest water flow needs no longer dictate the flow rate for all water tubes.

Testing and training lab

In Summer 2017, LIGO Livingston received a neoLASE© 70 W amplifier. Prior to incorporation into the interferometer's pre-stabilized laser (PSL) set up, the 70 W amplifier system was installed and tested in the Testing and Training (TNT) Lab. Located across the street from the main detector, the testing facility is an almost-complete replica of the LIGO PSL room: an optics table in a clean room with an NPRO, 35 W amplifier, high power oscillator, controls/computer system, water cooling system, diode room, etc.

A complete installation of the amplifier was stepped through and beam quality, power, and stability out of the amplifier was measured. Output power was shown to be stable over 80 W over many days, shown in Fig. 3.2, with fluctuations dominated by NPRO instabilities and daily temperature trends.

The TNT lab also provided the potential for initial tests of the noise contribution of the new amplifier system. Accelerometers are installed on the optics table in the three coordinate directions; if the motion of the TNT table can be mapped to the PSL table, then previously measured PSL coupling functions can be used to project the contribution of the amplifier system to DARM. As the TNT is housed in a separate building and on a different concrete slab than the PSL, measurements were first made to compare the ambient motion of the two. With normal ambient systems running and the 70 W water supply chiller running, motion of the TNT table is on average an order of magnitude higher than the PSL table above 80 Hz and higher below 80 Hz.

We performed a test to measure the minimal ambient noise of the TNT lab by turning off all moving equipment in the surrounding building (chillers, heating and air conditioners, etc.) except for cooling units for the server room (as this could only happen for short times); however, these could be heard from within the TNT lab and felt on the far wall (shared with server room), so likely is a major noise source. Results are shown in Fig. 3.3. In general, the motion of the TNT table over 80 Hz during an all-off time is comparable to the ambient PSL table motion; this means that the TNT lab can be used to test noise contributions of

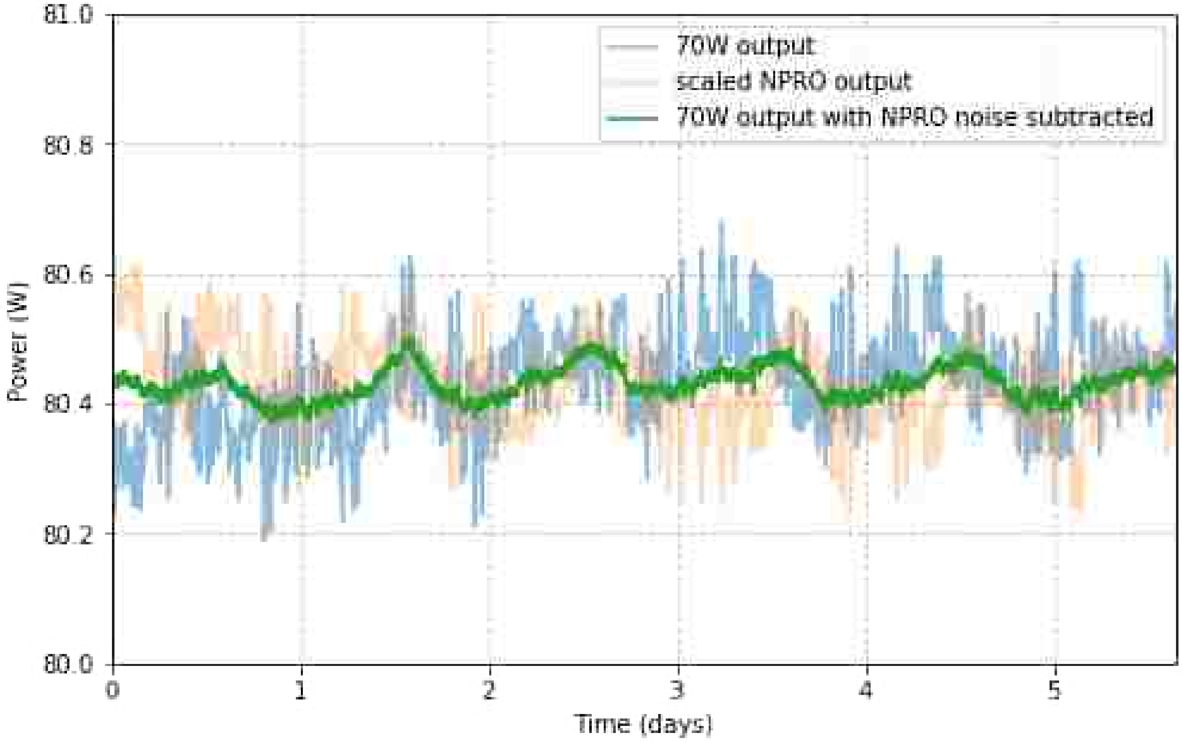

Figure 3.2. 70 W output power stability over 6 days in the TNT lab. Blue shows output of the 70 W amplifier as measured by the PD in the pick-off path after the amplifier. Orange shows the scaled NPRO output and green is the 70 W output with the NPRO power fluctuations subtracted. The fluctuations remaining post subtraction are coincident with daily temperature trends.

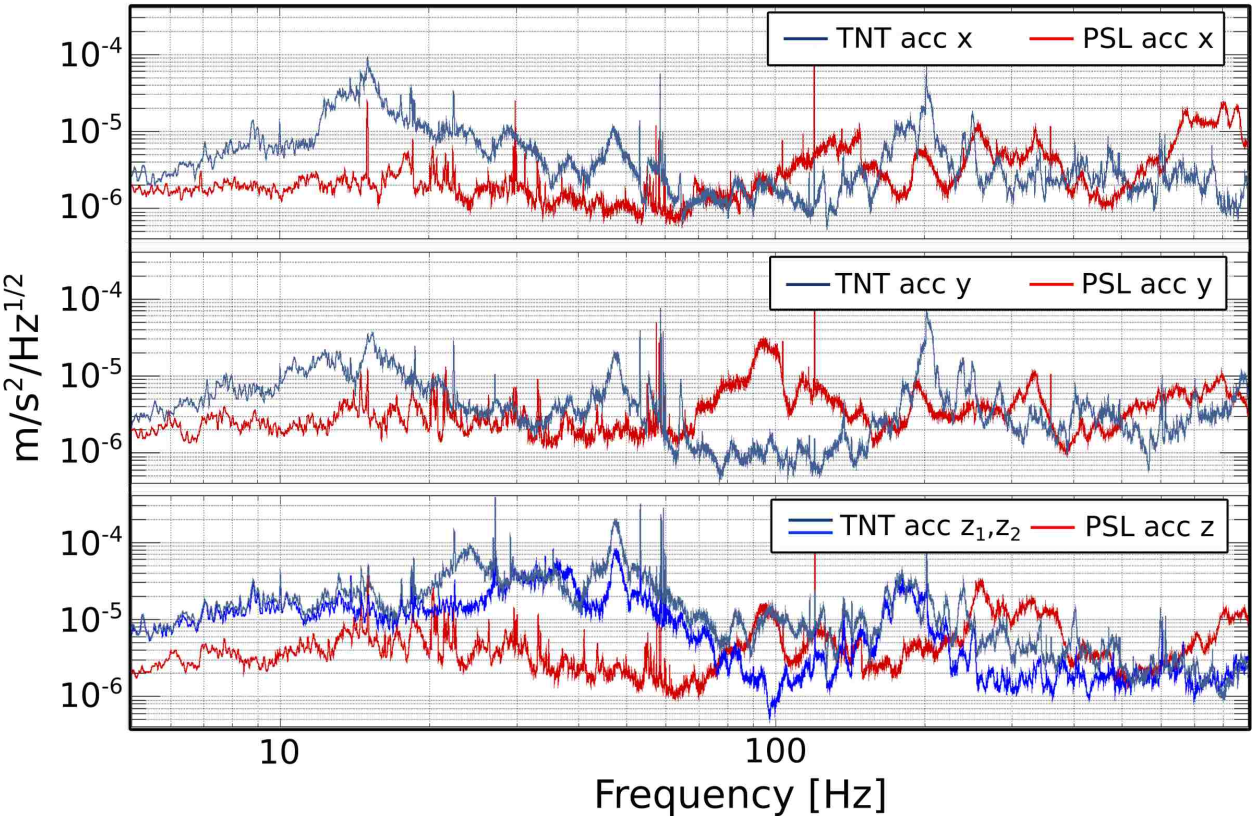

Figure 3.3. Spectra of accelerometers on the TNT table in X, Y, Z-direction during all-off test and on the PSL table during a quiet time in July 2017; note there are two Z-direction accelerometers. TNT ambient motion is reduced above 100 Hz during the test, more comparable with PSL, though a broad peak around 200 Hz sits about an order of magnitude above PSL motion.

future systems over short amounts of time.

70 W amplifier integration and performance

Installation of the 70 W amplifier into the LIGO PSL system began as soon as the second observing run ended in August 2017. Installation occurred in parallel with interferometer commissioning laser needs, so the developed procedure focused on minimizing interruption of the existing laser system; the 70 W infrastructure was built in parallel for as long as possible and a single mirror flipped between the previous and in-process optical paths. The output of the amplifier was modematched to a pre-existing bowtie cavity pre-mode cleaner (PMC); as it sets the pointing to the interferometer, the PMC and the optics after it were not altered.

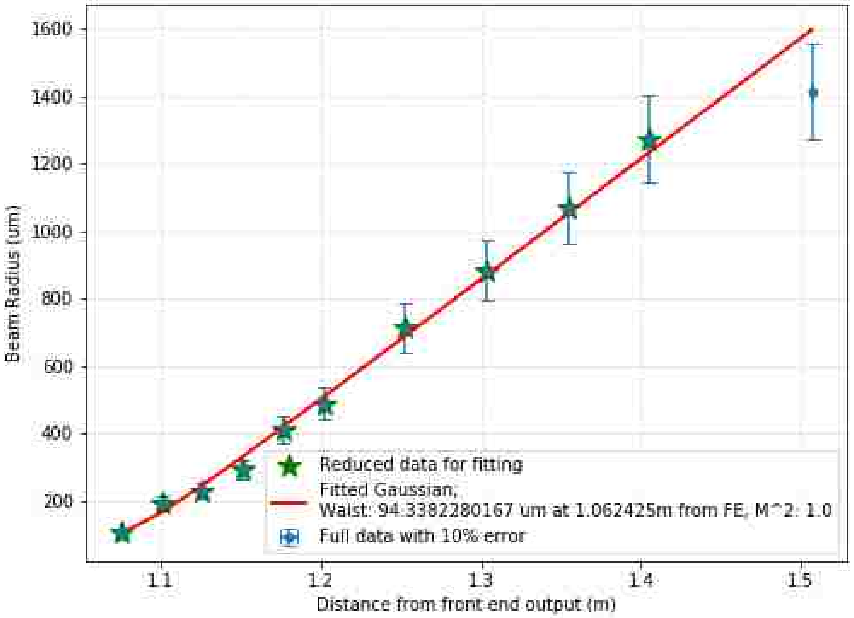

Figure 3.4. Result of caustic measurement of the beam out of the Front End after an f = 200 mm lens. Beam radius data is fit with a Gaussian and extrapolated down to the center of the Gaussian to extract the waist location.

A new pickoff was installed in the Front End 35 W amplifier to monitor power, thus altering the output beam. A new beam characterization (caustic) measurement was taken, using an f = 200 mm lens. Result, with Gaussian fit, shown in Fig. 3.4. The specifications for the 70 W amplifier is the waist size to be 135um, at a distance of 7.2cm in front of 70W amplifier. Two lenses, 50 mm and 100 mm, modematch the Front End to the 70 W amplifier. The amplifier continually outputs 80 W; power output has remained stable over 80 W during the two years since installation. The output of the 70 W is not fully Gaussian; a pedestal/halo was not able to be fully removed with modematching into the amplifier, indicating a slight internal misalignment. Ultimately, an aperture was placed immediately after the 70 W amplifier to clip the halo, resulting in a nearly-Gaussian beam transmission at the cost of a few Watts lost [25]. The 70 W is modematched to the PMC with two lenses, 300 mm and 400 mm. A simplified diagram of the optical path from Front End to PMC

Figure 3.5. Diagram of the Front End to PMC modematching layout.

is shown in Fig. 3.5. PMC visibility is 89%, indicating modematching only 3% decreased compared to that obtained between the Front End and the PMC previously. The PMC has a few percent loss and loss budget from 70 W amplifier to PMC optical path is 6%. Power available out of the PMC to the interferometer has remained over 50 W, with overall few percent degradation dominated by PMC loss increase. Power and diode settings are summarized in Table 3.1. The final full PSL layout is shown in Fig. 3.6.

Table 3.1. Summary of power values along the beam path and diode pump currents and temperature for the 35 W Front End (FE) and 70 W amplifiers [26, 27]

Power budget		**FE diodes**		**70 W diodes**	
power out of FE	35 W	FE D1/2	56 A	70 W D1/2	44 A
power out of 70 W	85 W	FE D3/4	50 A	70 W D3/4	37 A
power to PMC	68 W	FE D1 temp	19 C	70 W D1 temp	30 C
PMC visibility	90%	FE D2 temp	23 C	70 W D2 temp	28 C
PMC throughput	84%	FE D3 temp	22 C	70 W D3 temp	25 C
PMC loss	6%	FE D4 temp	18 C	70 W D4 temp	29 C

Total PSL ambient noise with the 70 W setup was successfully reduced to O2 levels. This required altering the water flow configuration, particularly at the breakout manifold. Water arrives in parallel configuration from the chillers (located outside of the PSL) and is directed to its component pathways (FE, 70 W amp, and water-cooled beam dump) at a manifold sitting on the floor under the optic table. This parallel configuration is a design feature of the new setup, allowing for individual flow control, as opposed to the previous series configuration where the water flowed from the chiller at the required highest flow rate. Even with the parallel configuration, table motion was still elevated from O2 levels. Water flow was being fine-tuned by valves at the manifold; it was found that when these valves are partially closed, the flowing water vibrates the valves and couples via the floor to the optic table. By fully opening the manifold valves and controlling flow rate only on the chiller side, in addition to adding vibration isolation under the manifold, the table motion dropped to O2 levels. Flow rates for each path are around 2.2 lpm.

3.2 Jitter coupling

In the noise budget shown in Fig. 2.5, we see input jitter noise with peaks in the few hundred hertz range. In this section, we review what input jitter is and how it couples to differential length. We present jitter noise measurements with the new amplifier setup and discuss the work done to reduce higher noise peaks. At the end of the section, we set a lower limit on jitter dependence of point absorbers.

Input beam jitter is fluctuations of input beam size and pointing. Jitter couples to DARM when the interferometer is misaligned. A lateral shift in beam direction - fluctuating at a frequency within the gravitational wave band - leads to a phase variation in the misaligned Michelson arms. As the misalignment is slow or static, the result is fluctuating phase in the gravitational-wave signal band at the jitter frequency. Thus, to first order, jitter of the phase front can be described as sidebands on the carrier separated by the jitter frequency.

Jitter can come from the laser itself or motion of the mirrors steering the laser field into the interferometer. The highest jitter noise historically occurs from resonant motion of mirrors on the PSL table; work was successfully done during O1 and O2 to redesign mirror mounts and damp jitter peaks. The most problematic resonances are from mirror mounts attached to a periscope which directs the beam up from the PSL table height to the interferometer beam line height. The new amplifier set up brought new water flow needs, which vibrates the table and can ring up mount resonances.

Prior to O3, jitter resonances were found at 490 Hz and 520 Hz from two mirror mount resonances, respectively; these mirrors are used to steer the high power beam from the PSL table height up a periscope to the main interferometer beam path height. Broadband tuned-

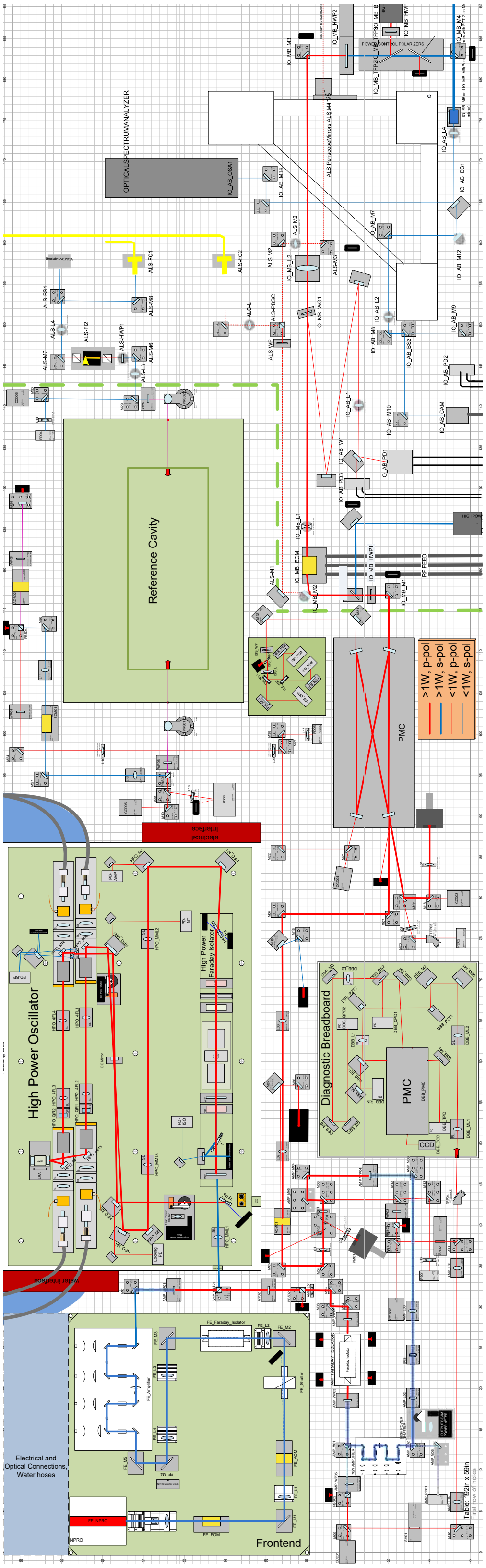

Figure 3.6. The complete aLIGO laser table layout with the 70 W amplifier scheme. The amplifier can be seen as a white box in the bottom right of the table.

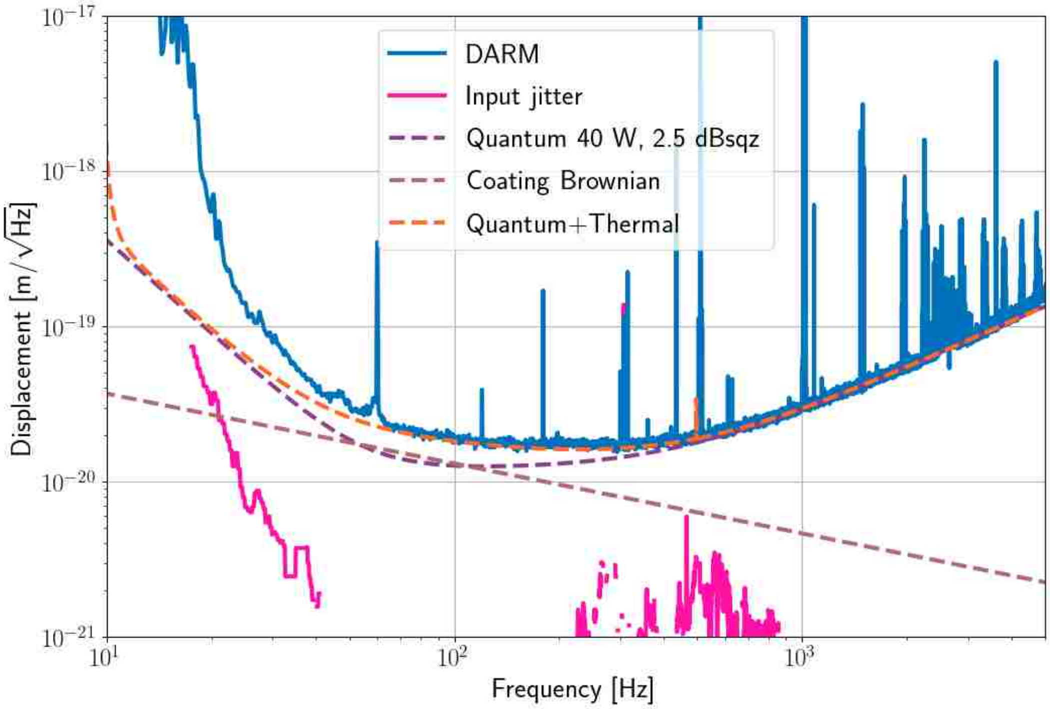

Figure 3.7. Noise projections of O3 jitter with 70 W amplifier set up prior to damping the last high resonance (see here at 490 Hz), since reduced by x3. First, coupling functions are made by injecting noise until a response is seen in DARM (in this case, shaking the optic table or a steering mirror). That function can then be multiplied by ambient noise to estimate how far below DARM the nominal noise sits. If the original injection was not strong enough to couple into DARM significantly, only upper limits can be placed.

mass dampers, shown in Fig. 3.8 were installed on the mounts, reducing the jitter peaks by a factor of 3 and 10, respectively.

To measure the ambient noise floor, jitter noise is elevated until a response is seen in DARM. Two methods of injection are used to excite the full gravitational-wave frequency band. For excitation above 40 Hz, a speaker is set up inside the PSL enclosure; broadband audio injections into the room shake optical components and thus amplify jitter on the input beam. For low frequencies (where the speaker cannot produce enough power for ample excitation), the piezoelectric steering mirror before the periscope is driven in pitch and yaw. Coupling functions are calculated using DARM signal and IMC RF wavefront sensor (WFS)

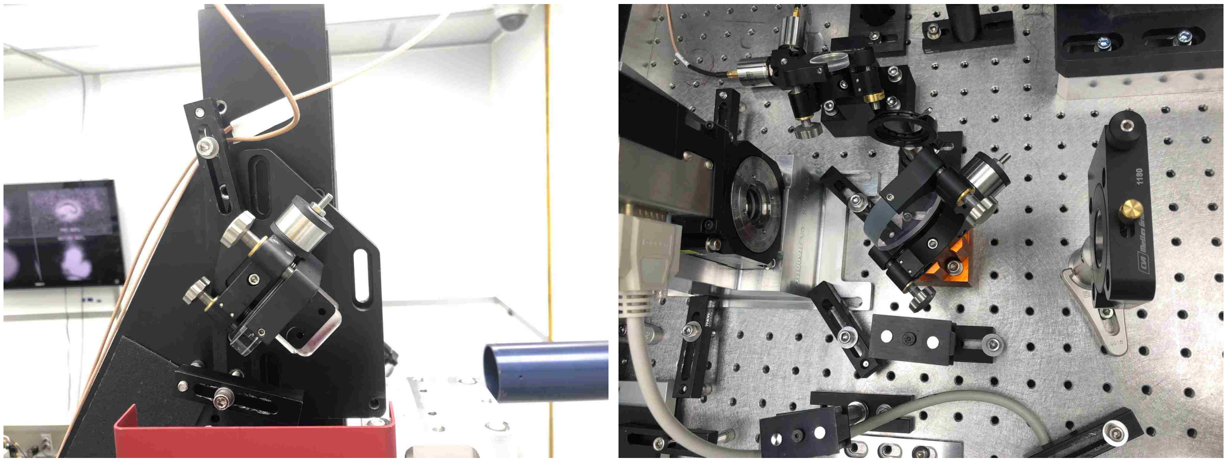

Figure 3.8. Mirror mount resonance dampers (silver cylinders) installed on the upper periscope mirror (left) and a table-top steering mirror (right).

during the excitations and the ambient quiet times:

$$C(f) = \frac{\sqrt{\mathrm{DARM}_i(f)^2 - \mathrm{DARM}_q(f)^2}}{\sqrt{\mathrm{WFS}_i(f)^2 - \mathrm{WFS}_q(f)^2}}. \tag{3.1}$$

As the WFS sense both pitch and yaw, the two degrees of freedom are quadrature summed for the coupling estimate. Note that this could be an overestimate if the coupling is primarily sensed in just pitch or yaw or an underestimate if sensed coherently in both.

The ambient noise floor in DARM units can be estimated by multiplying the quiet sensor noise by its coupling function to DARM. The O3 jitter noise budget is shown in Fig. 3.7.

Jitter coupling dependence on point absorber overlap

The presence of point absorbers can theoretically increase coupling of jitter to DARM. The high absorption heats the spot, causing expansion, and creating local tilt deviations. Beginning in O2, we found small areas of high absorption on some test masses. These point absorbers - discussed more extensively in Sec. 4.3.2 - are roughly 10 - 20 micron diameter areas that absorb order 10 mW (with around 270 kW circulating power in the arms) depending on the overlap between the beam and the absorber.

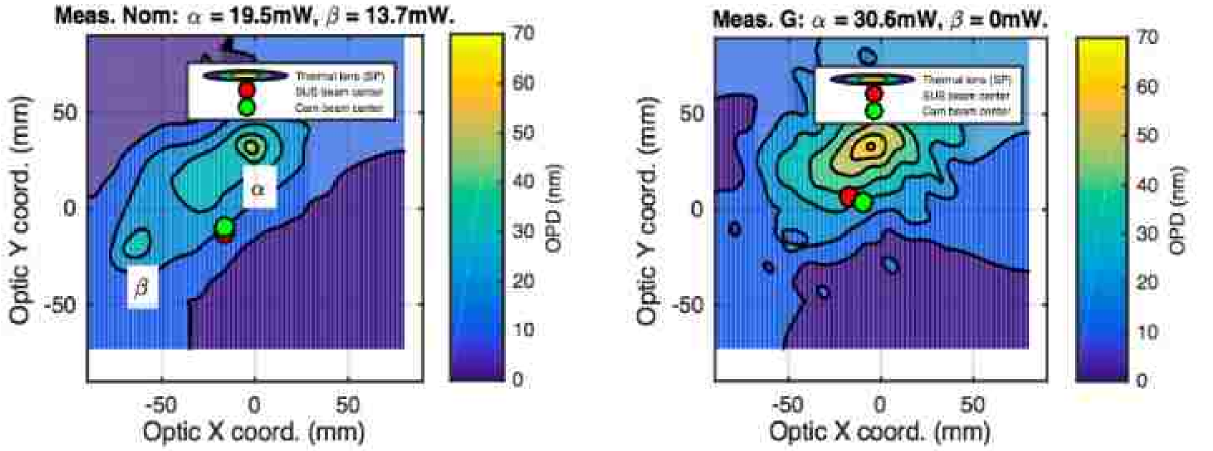

Figure 3.9. Beam location of two spot positions (nominal and 'G') relative to point absorber on ETMX. Optical path distortion (OPD) is measured by Hartmann Wavefront Sensors, with nominal RoC removed. The remaining OPD is dominated by two point absorbers, α - the larger, higher point - and β - the smaller, lower left point. Contour lines are spaced 5 nm apart. The red and green spots show the center of the X-arm cavity beam incident on ETMX, as determined by two different methods.

After the ETMs were replaced prior to O3, at least two point absorbers were found on the new ETMX: α, the larger absorber, sitting above the center of the optic, and β, smaller and sitting down and left from the center. Prior to the run, the position of the arm cavity beam was moved to optimize arm cavity buildup, resulting in a nominal beam location on ETMX 12 mm down and 17 mm left from optic center.

To further explore, the beam was slowly walked to several different spots and held there long enough for control loops to settle and thermal dynamics to reach steady state (walks performed by Effler [28]). For each spot change on ETMX, locations on other optics remained the same. Both optical gain and power recycling gain loss were monitored to judge 'badness' of spot. For all positions tried - mostly covering the left side of the optic - both gains decreased, though at different rates, indicating that both power loss and mode deterioration occurred. Loss could also occur if the edge of the beam falls off the central coating requirement area; the beam size is 124 mm diameter and the optimized coating size is 160 mm diameter, so the nominal spot position is likely just falling off the coating at one edge and

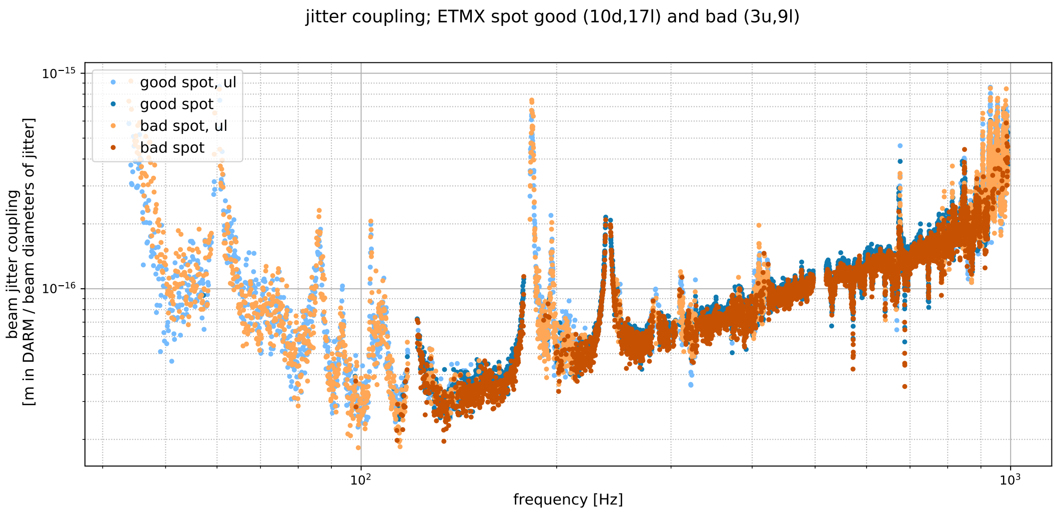

Figure 3.10. Jitter coupling at two different spot positions with different overlap with - and therefore intensity of - the worst point absorber on ETMX. No change in jitter coupling was found between a 19.5 mW point absorber and a 31 mW point absorber.

several test spots would have parts of the beam several mm off.

To test jitter coupling dependence on spot position overlap with point absorbers, jitter coupling was measured at two ETMX spot positions [29]. Good and bad positions were chosen based on previously discussed measurements, good being the nominal position (as well as highest power recycling gain) and bad being the position closest to the larger point absorber (as well as the lowest recycling gain). The spot positions relative to the point absorbers is shown in Fig. 3.9. Optical path distortion caused by the α and β point absorbers is shown overlaid with the approximate location of the beam; point absorber analysis was performed by Brooks [30]. At each spot position, a full suite of jitter injections was performed using the audio injection method. Both measurements were done during the same lock, under similar conditions; scatter noise varied based on uncontrollable environmental factors, but the coupling is analyzed above the frequencies nominally affected by scatter. Results are shown in Fig. 3.10: no change in jitter coupling was found between a 19.5 mW point absorber and a 31 mW point absorber. The power in the absorber at each spot position is found by measuring the optical path distortion caused by the absorber at the time of the different beam overlaps.

3.3 High power impact on sensitivity

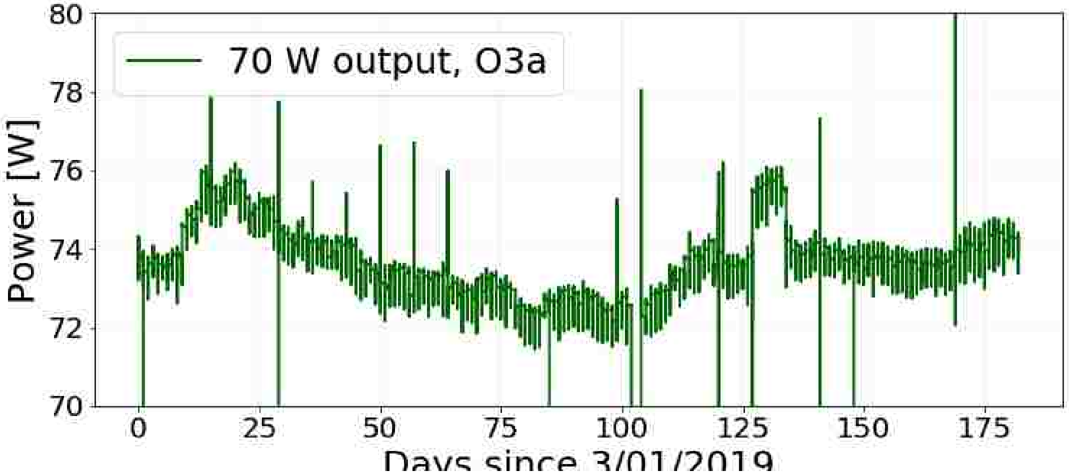

Figure 3.11. Output power of the 70 W amplifier over the first half of the third observation run.

Since installation, the 70 W amplifier has continually output between 70-80 W, providing at least 50 W available to the interferometer. Power has remained stable, with 2-3% variations due to temperature changes or diode current tweaks, see Fig. 3.11.

During O3, we are operating with approximately 40 W into the interferometer. The impact of increasing the input power from 25 W to 40 W is shown in Fig. 3.12 (at a time of no squeezing). With a 1.6 factor increase in power, we expected and found a $\sqrt{1.6} = 1.3$ factor in sensitivity over 60 Hz, as well as in range improvement ($\sim$ 90 to 125 Mpc). As the search volume goes as the cube of the range, the increased power has more than doubled the volume of the universe LIGO Livingston is observing.

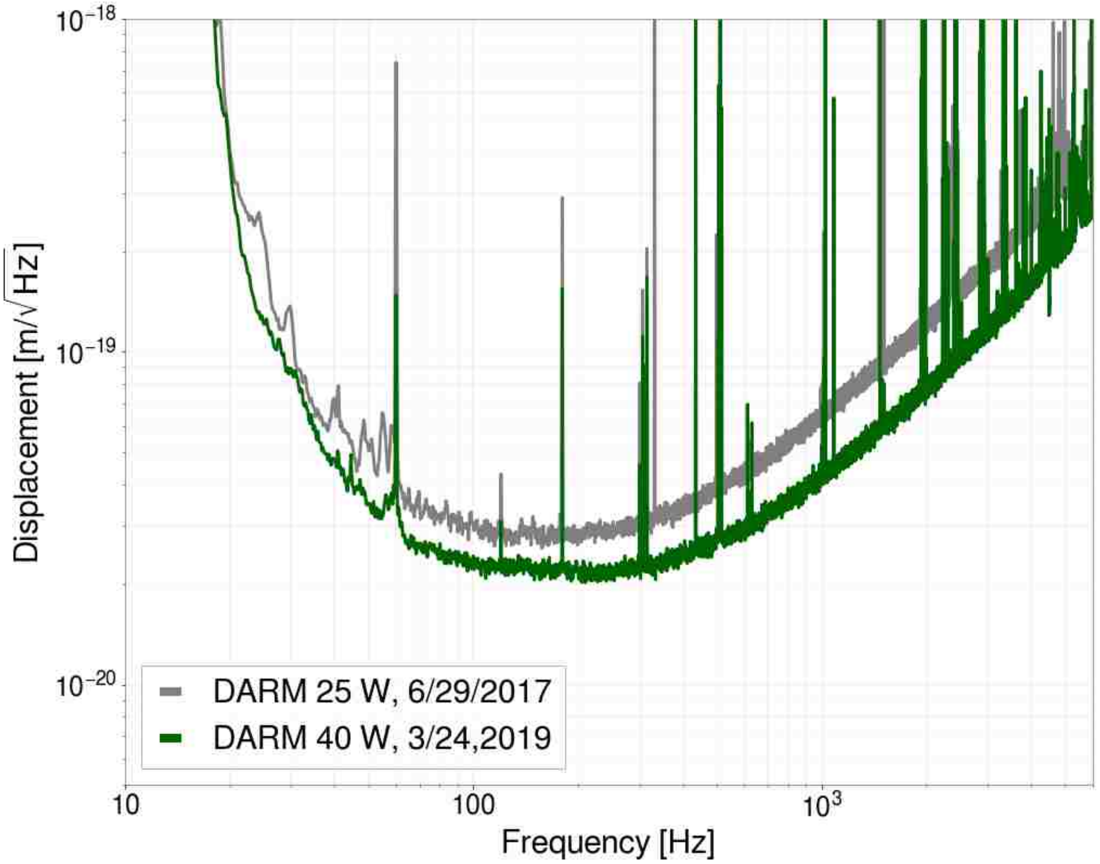

Figure 3.12. Output power of the 70 W amplifier over the first half of the third observation run.

4 High Power Thermal Effects

This chapter discusses how uniform and nonuniform absorption in the test masses leads to thermal surface and substrate distortion driven by the high circulating power. Mirror aberrations can cause mode mismatch and scattering, which lead to power loss and noise couplings to the gravitational-wave readout. Work to characterize and minimize these effects at LLO is presented. The author significantly contributed to re-commissioning the sensors used to analyze the test mass absorption, as well as perform long term analysis on the uniform and point absorbers. Tests and analysis to minimize laser noise coupling were led by the author, with significant input from C. Blair and V. Frolov and A. Mullavey; previous analyses done by previous commissioners at lower powers are noted. The last section of the chapter discusses the set up and results of applying CO_2 heating to the signal recycling mirror to optimize output beam modematching to the output mode cleaner. The author was part of a larger team conducting these test at both sites; in particular, the author worked to characterize the setup at Caltech under A. Brooks, performed the output beam characterization measurements at LHO, and installed, commissioned, and analyzed the setup at LLO alongside M. Kasprzack and C. Blair.

4.1 Overview of thermal effects

Design sensitivity of aLIGO assumes ideal modematching and minimal loss between the coupled cavities of the interferometer, where the beams recombining at the beamsplitter experience near-complete destructive interference and the beam transmitted through the signal recycling cavity is modematched to the output mode cleaner cavity. In reality, optics vary from their ideal radius of curvature and have minor defects which distort the wavefront. Additionally, high power passing through or reflecting off the surface of optics can create thermal defects, illustrated in Fig. 4.1. Thermally driven mirror aberrations can lead to power loss and increased noise coupling to the output port by mode mismatch and scattering.

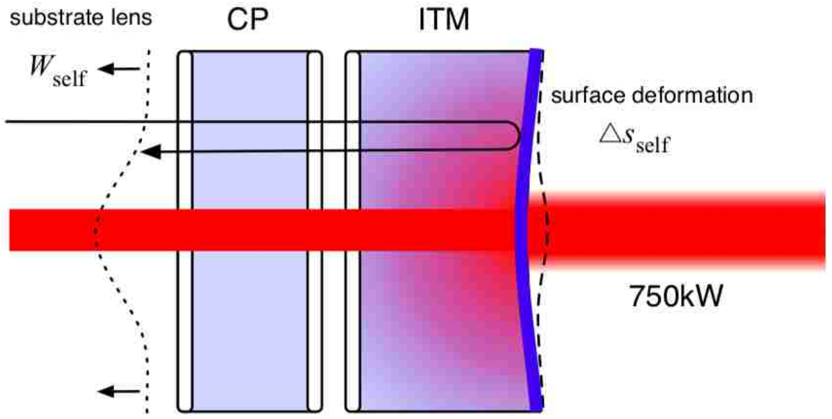

Figure 4.1. Surface deformation Δs_{self} and substrate lensing due to central heating from the circulating high power beam causing wavefront distortion W_{self}. Here the initial test mass (ITM) forming one of the 4 km arm cavities is shown, with the blue line indicating the HR surface. Before the ITM hangs the compensation plate (CP), an identical mass sitting between the ITM and the other coupled cavities of the interferometer. Figure by Brooks [31].

Mode mismatch

The coupling efficiency between the electric field entering a cavity and the fundamental field that resonates in the cavity can be described by the overlap integral

$$\eta = \frac{|\int E_c^* E_i dA|^2}{\int |E_c|^2 dA \int |E_i|^2 dA} \tag{4.1}$$

where E_c is the ideal cavity field, E_i is the input field, and the overlap is carried out over the full beam cross-section; movement away from full overlap indicates loss. If the optics forming the cavity differ from design (i.e. non-ideal radius of curvature, surface aberrations), then the ideal input beam parameters will no longer match the cavity parameters and less power couples to the cavity. Similarly, if the pumping field is non-ideal or picks up wavefront aberrations as it passes through the input optic, then there is also loss.

Thermally driven distortions alter the parameters of the interferometer's coupled cavities shown in Fig. 4.2 which can move them away from ideal modematching and decrease the gravitational-wave sensitivity. In aLIGO, absorption-driven surface deformation and wave-

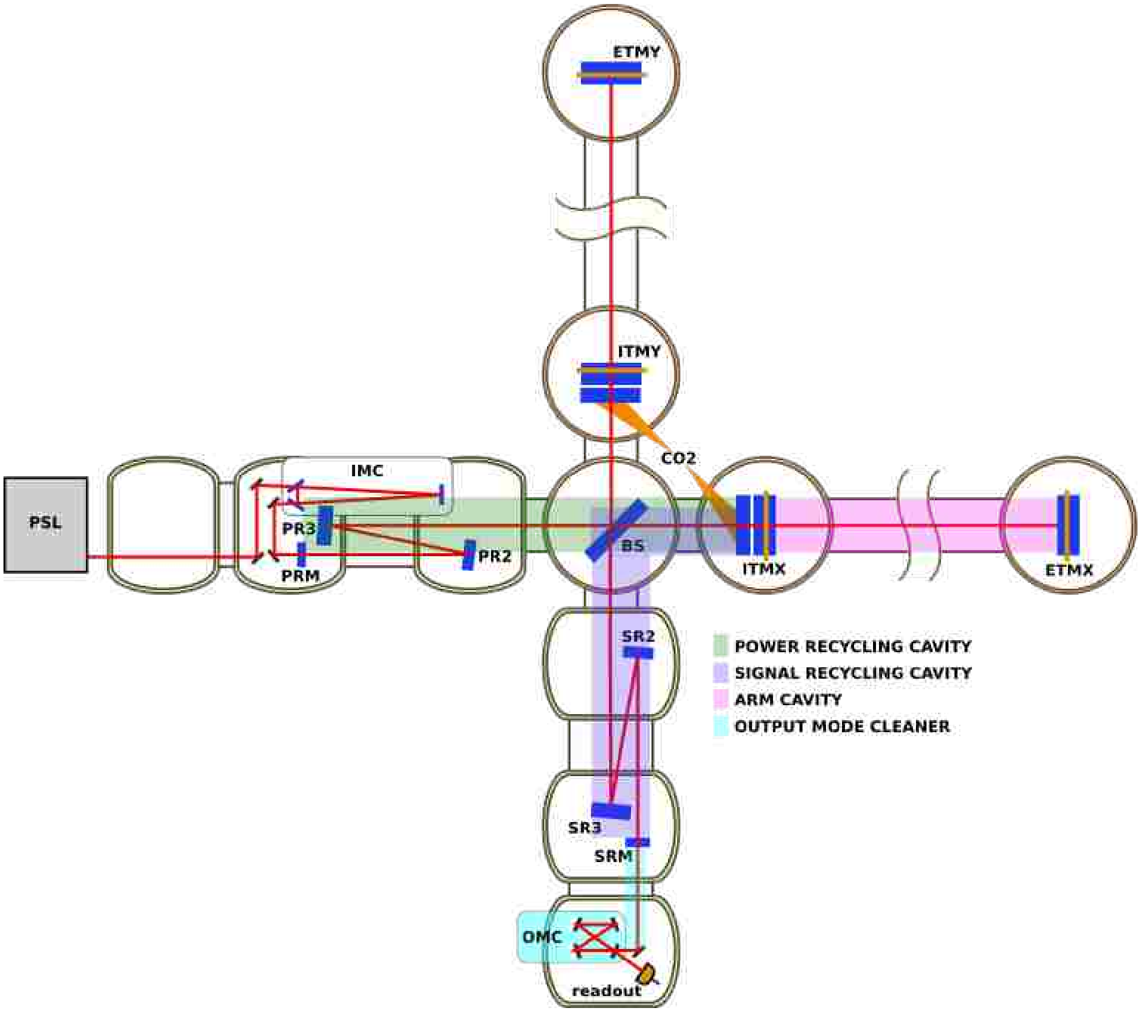

Figure 4.2. Overview of coupled cavities discussed in this chapter. For simplicity, only the cavities relating to one arm are highlighted.

front distortion from circulating power are significant within the high power arm cavities, specifically on the high reflectivity surfaces of the test masses and within their substrates. As the substrates of the ETMs lie outside of the field interactions that propagate to the dark port, only the thermal substrate distortions of the ITMs are impactful. A summary of thermal effects on modematching is outlined below; for a more complete analysis, see Ryan Lawrence's thesis [32] and Kiwamu Izumi's analysis on the frequency response of the aLIGO interferometer [33].

- Common mode carrier

  Consider the arm cavity with high circulating power and uniform surface absorption in the test masses (i.e. purely spherical thermal distortion). Thermal surface distortion from central heating effectively flattens the mirrors, altering the resonant spacial cavity mode. The reflectivity of the mirrors is not altered, so the arm cavity gain (P_{arm}/P_{PRC}) is only affected by mode matching between the power-altered field resonating in the arm and the field pumping it. The overcoupled arm cavity defines the fundamental mode in the interferometer; transmissive phase distortions in the ITM are essentially invisible to the carrier and the carrier gain in the PRC is unaffected.

- Common mode sidebands

  As the sidebands are anti-resonant in the arm cavities, their resonant mode in the PRC is defined by the ITMs - including thermal transmissive distortions. While the PRM does experience thermally driven distortion, the effect from the ITMs dominates as the absorbed power is several orders of magnitude higher in the latter. As seen by the PRC, thermal lensing of the ITM makes its effective curvature becomes more concave, thus decreasing the sideband mode.

- Differential mode

  Differential thermal effects cause imperfect interference at the beamsplitter, leaking carrier light to the dark port. Imperfections in the 50/50 beamsplitter coating, slight manufacturing differences in test mass RoC, inhomogenous absorption in the bulk and surface of the test mass, and resultant difference in circulating power in the respective arm cavities can all lead to non-identical fields incident on the beamsplitter from each arm.

In summary, assuming a stable Guassian mode exists in the arm cavities, distortions common to both ITMs most significantly cause loss in the sideband power stored in the PRC. The carrier is only slightly effected unless thermal distortion is so large that there is no mode common to the arm cavities and the PRC. Differential distortions couple carrier power to the dark port and cause sideband loss; both effects increase phase noise at the dark port, decreasing sensitivity.

Scatter

Round-trip loss in a cavity can arise from high spacial frequency mirror surface aberrations scattering power out of the fundamental mode and into higher order modes [34]. A beam incident on a distorted mirror surface can be modeled as light diffracted by a grating with spacial wavelength λ_m. The spacial frequency is given by

$$\Omega = \frac{\sqrt{2}\pi\omega_0}{\lambda_m} \tag{4.2}$$

where we have normalized to the size of the beam waist ω_0. A more complete discussion of mirror surface map coupling to higher order optical modes is presented in Chpt. 6, but for now we quote the result: for mode $n \geq 2$, the power scattered into the optical mode by the distorted mirror surface is

$$P_n = \frac{1-(-1)^n \cos(2\Phi)}{2} \frac{\mathcal{A}^2}{n!} \left(\frac{\Omega^2}{2}\right)^2 e^{-\Omega^2/2} \tag{4.3}$$

where mirror deformation amplitude $\mathcal{A} \ll 1$ and Φ is a term accounting for spacial phase from deformation with respect to the beam axis. Power can scatter from the fundamental mode into a HOM partially resonant in the cavity, amplifying the losses.

With these high power effects in mind, we now review the hardware in place to measure and compensate them.

4.2 Thermal compensation system

Advanced LIGO includes a thermal compensation system to sense and correct thermally-induced distortions. All concepts are illustrated together in Fig. 4.3. The system is only summarized below for reference; it has been presented in detail by Brooks [31]. The system senses optical path distortions with high spacial frequency resolution (<10 nm), provides quadratic correction (i.e. altering the overall radius of curvature) to the test mass sub-

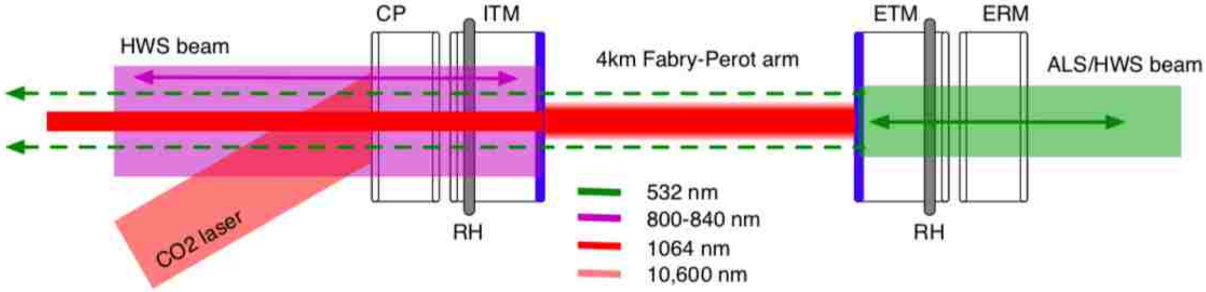

Figure 4.3. Components of the thermal compensation system on one arm cavity. The main interferometer beam - providing central heating - is shown in red. Ring heaters, shown in grey, encircle the ITM and ETM acting as an actuator to decrease the radius of curvate. Probe beams for the Hartmann Wavefront sensors are injected through the back of the ETM (green) and ITM (violet), respectively, to monitor the wavefront distortion. A CO_2 laser beam (salmon) incident on the back of the compensation plate (CP) creates a tunable lens between the arm cavity and the rest of the interferometer field. Figure by Brooks [31].

strate and surface, and can provide correction to the wavefront by altering the lens of the compensation plate (reaction mass behind the ITMs). The system cannot correct surface deformations due to non-uniform absorption.

In Sec. 4.2.1, we also introduce a new pre-filtering scheme for the ring heaters which has been successfully implemented at both detectors to provide accurate transient central heating compensation.

Ring heaters

Ring heaters consist of a glass rod wrapped with nichrome wire that encircles the barrel of the test mass without directly touching it. When current is driven through the wire, the glass and wire heat up and radiate heat onto the barrel of the optic. The rod and wire are divided into two segments, an upper and lower, attached to the suspension cage. A gold coated shield surrounds the ring heater on the outer side, reflecting outward-radiating heat back towards the test mass.

Ring heaters work to mend the arm cavity mode (i.e. E_c in Eq. 4.1), actuating on the test mass radius of curvature and thus the cavity g-factor (where $g = g_1 g_2$ and $g_i = 1 - L/R_i$ for each mirror radius of curvature R_i) to return it to ideal. They create a radial temperature gradient in the test mass, forming a negative thermo-refractive lens in the substrate and decreasing the radius of curvature. The arm cavity beam, roughly centered on the test mass, heats the center of the optic, effectively increasing the radius of curvature; the ring heater, in contrast, heats the outer radius of the optic, effectively countering the central heating. Ring heaters have large thermal time constants (approx. 24 hours) after an initial overshoot of a few hours; historically, optimal operation involved tuning the steady state settings and then leaving the ring heaters at that constant power. In Sec. 4.2.1, we present a new technique to significantly shorten this time constant.

CO_2 lasers

One more degree of control is necessary for mode matching. CO_2 (λ =10nm; fully absorbed by optic) beams are projected onto the back of the compensation plate, creating a tunable lens between the arm cavities and the other cavities of the interferometer. Before impinging on the compensation plate, the beam passes through a mask that sets a spacial distribution; this mask can be interchanged, allowing for tunable beam shape. The nominal design consists of central heating and annular heating, the former to counteract strong arm cavity central heating transients during locklosses and the latter to tune the residual distortion from the combined ring heater and central heating settings.

Hartmann wavefront sensors

Hartmann wavefront sensors (HWS) are designed to measure the wavefront distortions in the test masses. For each test mass, a probe beam is injected into the vacuum system, travels through the compensation plate and through the substrate of the test mass before retro-reflecting off of the HR surface and returning to a sensor outside of the vacuum system. The sensor consists of a plate of holes through which the returning beam passes before falling on a CCD. The spot positions created by the holes encodes the wavefront slope at each point; integrating the full gradient field gives the overall wavefront change [31]. The sensors have a spacial resolution of approximately 7.5 mm in the ITMs and 9 mm in the ETMs. Hartmann wavefront sensors are crucial for matching radius of curvature time constants (i.e. when correcting central heating with ring heaters) and for locating and characterizing point absorbers.

4.2.1 Ring heater input filtering

The ring heater and central heating have different RoC step responses, shown in Fig. 4.4. The lensing behavior due to the cavity power is asymptotic, reaching its approximate steady state value within the first hour. The ring heater transient has an initial overshoot as the heat first hits the outer edge, reaching the minimum defocus after 2 hours, followed by a long, slightly increasing RoC transient as the heat is distributed throughout the test mass until steady state is reached about 12 hours after the power up. The ring heater has a 15 min delay before a RoC response is observed. Thermal compensation for cavity control can be improved if the lens response from the ring heater more exactly offsets the central heating response.

It is possible to reduce this time constant and eliminate the overshoot with real-time digital filtering of the RH step input. An optimal filter is designed by transforming the impulse response of the system into the frequency domain, fitting a zero-pole-gain (zpk) model to the response, and then inverting said model ($\mathrm{H}^{-1}(\mathrm{s})$) [35]. Additional filters ($\mathrm{G}(\mathrm{s})$) are required to stabilize the inverted zpk model and allow some freedom to tune the time constant; signal flow outlined in Fig. 4.5. The filtered ring heater input and resultant thermal lens in congruence with central heating is also shown in Fig. 4.4.

The ring heater conditioning technique was successfully tested at both detectors. The interferometer was locked and Hartmann wavefront sensors were used to measure the surface and substrate thermal deformation transient due to central heating. Once the system had

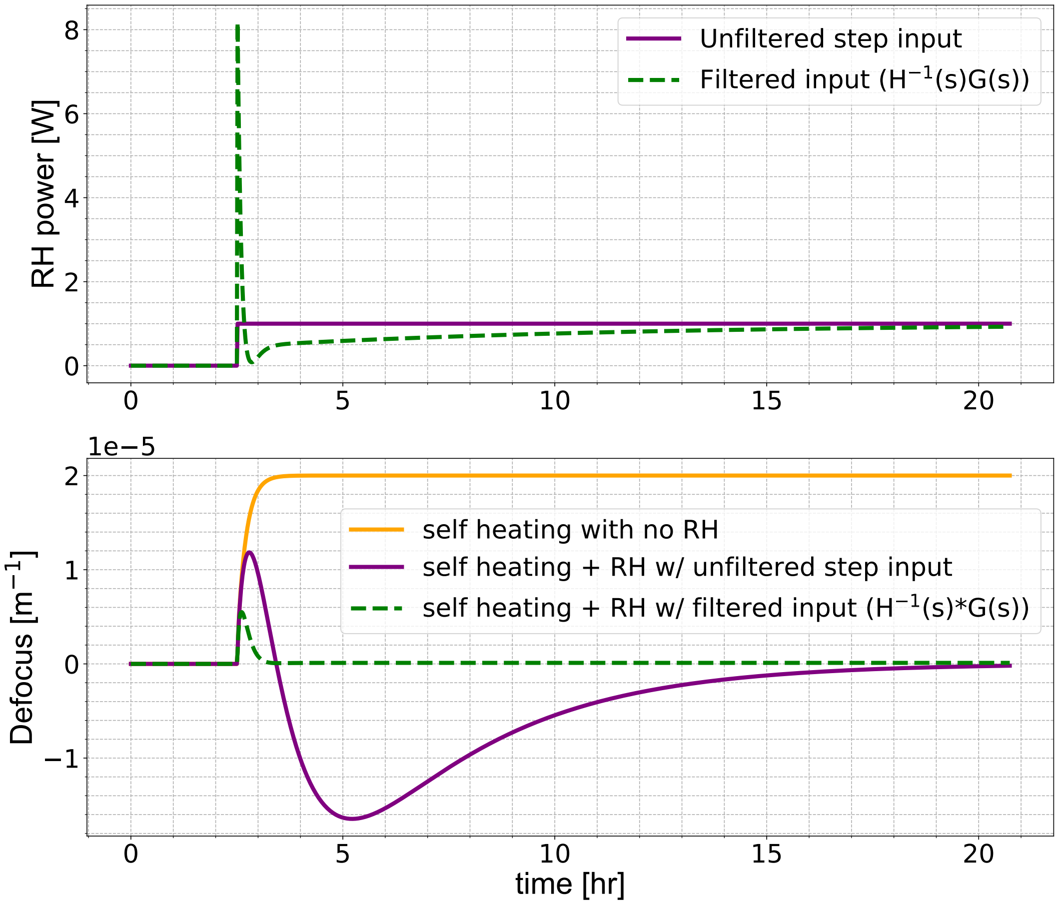

Figure 4.4. Comparison between the natural transient response of the RH vs. the conditioned transient response from $\mathrm{H(s)}^{-1}\mathrm{G(s)}$ where the response filter is a second order low pass. Plot made by Daniel Vander-Hyde.

thermally stabilized, the ring heaters were stepped up by 0.4 W with the inverse filter engaged and the resultant lensing was measured in the same way. The measured transient time constant of the ring heater differed by only 15 min from that of the central heating, indicating reasonable transient compensation.

Filters have also been tested that provide fast transients (∼1000 sec) for small steps, allowing near instantaneous control of the cavity g factor. This fast feedback time will be

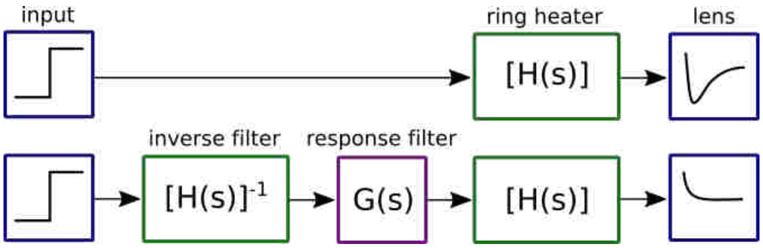

Figure 4.5. Diagram showing the effect of a step in the ring heater on the thermal lens (top), and the filtered step response (bottom).

helpful for real-time cavity geometry control as discussed in Sec. 5.5. Note that as this pre-filtering technique requires a large ring heater power input at the beginning to offset the initial delayed response, this sets a more narrow limit on the central heating power that can be compensated. The ring heaters have a maximum delivery power of 40 W. In Fig. 4.4, the final steady state ring heater power is 1 W but 8 W are used during the initial transient, indicating that this same methodology could be used up to a steady state ring heater power of 5 W.

4.3 Absorption

This section walks through how high circulating power deforms the test masses via absorption. Uniform and non-uniform (point) absorption is discussed.

4.3.1 Uniform absorption

The test masses that form the arm cavities have nominal uniform coating absorption of 0.2 - 0.5 ppm. As power in the arms has increased to hundreds of kW, the power absorbed has increased to hundreds of mW. The subsequent temperature differential causes heating in the manner of the Gaussian distribution of the interferometer beam on the optic. This results in surface deformation of the high-reflectively side of the test masses and substrate lensing due to the change in index of refraction with temperature of the test masses, as shown in fig. 4.1.

These effects distort the wavefront of the beam passing through or reflecting off of the optic. The thermo-refractive substrate lens is colloquially referred to as wavefront distortion, and the surface deformation as a change in the sagitta (circular arc) of the surface. Both phenomena effect mode-matching between the coupled cavities of the interferometer. Deviation from perfect mode matching leads to loss and increased noise coupling to the dark port [32], discussed in Sec. 4.4.

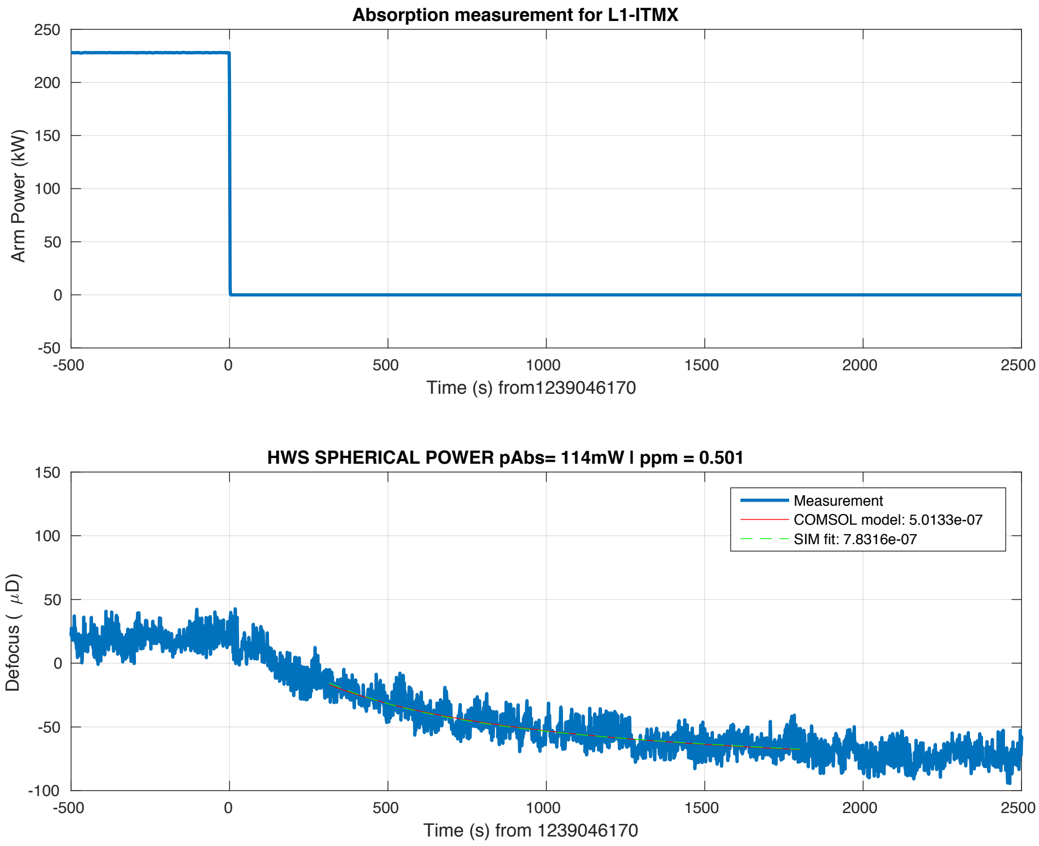

Figure 4.6. Fitting of ITMX spherical power during cooling to estimate absorption. Top panel shows arm power; lockloss occurs at t=0. Bottom panel shows HWS spherical defocus data, with COMSOL fit in red.

The thermal lens power S in a double-passed test mass depends on absorption α and the power stored in the arm P:

$$S_{x,y} = 2 * \beta * \alpha_{x,y} * P \tag{4.4}$$

where β =487 is the single pass spherical power (microdiopters) per Watt of power absorbed [32]. To estimate absorption, a COMSOL model was made of the double passed thermal lens (spherical power) transient response from a 1 W absorbed power step response. As the thermal lens scales linearly with power, this model is then scaled by the absorption value and adjusted with an offset to fit thermal lens transient data from, either immediately after power-up or after lockloss. The stored arm power is calculated using the input power P_{in}, average power recycling cavity gain (PRG) for that lock, arm cavity gain ($\times$266), and accounting for loss in the input optics and the 50/50 beamsplitter: $P = P_{in}*0.9*\text{PRG}*0.5*266$. Live readout of the spherical power transient is obtained using the Hartmann wavefront sensors.

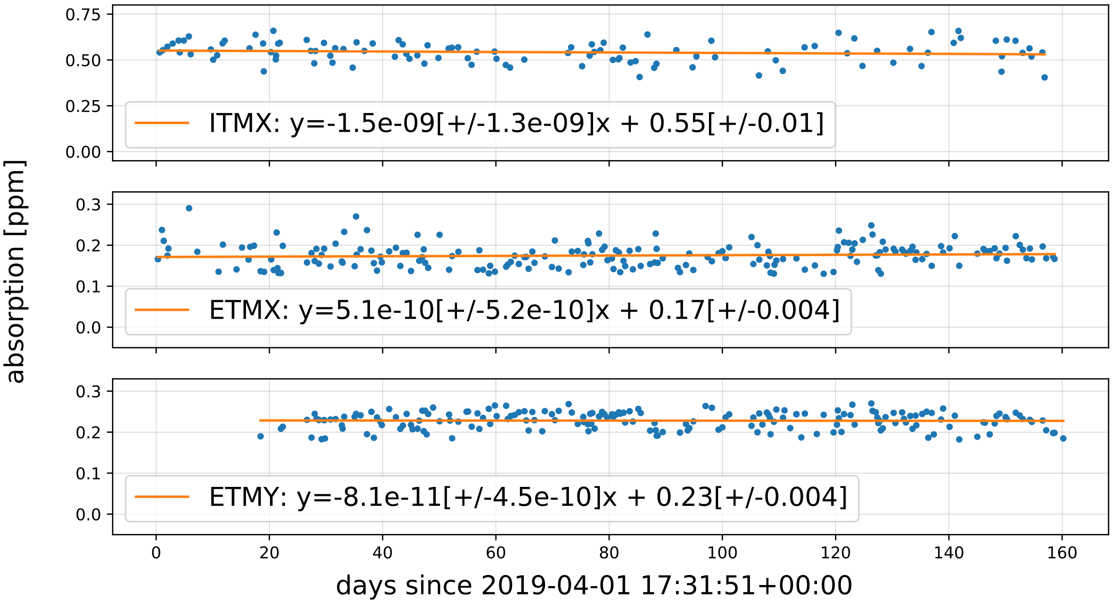

Figure 4.7. Absorption measurements during the first 160 days of O3 for ITMX and ETMs. The Hartmann wavefront sensor beam was clipping in the path for ITMY, so data has been excluded. Absorption data has been filtered to exclude extreme unrealistic values from poor fits and the first 20 days for ETMY when the Hartmann wavefront sensor was not operating nominally.

Uniform absorption measured and compiled by the author and others during the first half of O3 is shown in Fig. 4.7. Note that due to clipping in the path, the wavefront sensor beams can only be aligned for either ITMX or ITMY; during O3, ITMX was aligned for absorption measurements so ITMY is not plotted. Absorption measurements are shown for every lock longer than 2 hours during which the Hartmann wavefront sensors were operational. Cooling data (immediately after lockloss) is used for ITMs; ITMs are moved during lock acquisition for alignment purposes, smearing the ITM wavefront heating data. Heating data is used for ETMs, as leakage from the green auxiliary laser beam pollutes the ETM wavefront sensor and this auxiliary laser is shuttered during lock and unshuttered upon lockloss (cool down). Due to systematic uncertainties in the model used to perform the fitting, here we look for trends: fitting the several months of data finds no significant change of absorption in the three test masses monitored at LLO, shown in Fig. 4.7.

4.3.2 Point absorbers

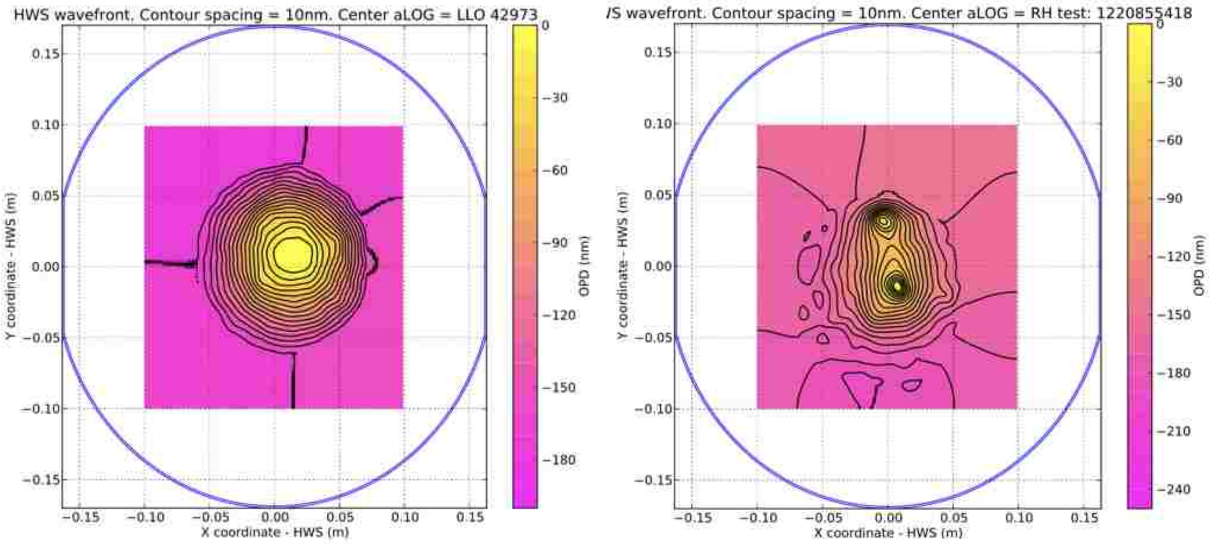

Figure 4.8. Optical path distortion measured by the Hartmann Wavefront Sensors for uniform absorption due to central heating (left) and uniform + point absorbers (right).

In addition to the uniform absorption, small ($\leq 100\,\mu$m) highly absorbing (>1e4 ppm) spots on the reflective surface of the test masses effect LIGO sensitivity. Point observers were first observed at LHO during O2 and are present on at least two optics at each site during O3.

Point absorbers can be sensed with the Hartmann wavefront sensors. Figure 4.8 shows an example of wavefront images for an optic with central heating and uniform absorption, and uniform absorption + point absorbers. The images map out x- and y-axis of the given optic, with colorscale showing optical path distortion. Contour lines are spaced at 10 nm of optical path distortion. Note that the wavefront sensor cannot give information about the size of an absorber smaller than the sensor's spacial resolution; rather, it provides the absolute power absorbed in an area. As we know the power incident on the optic, we characterize point absorbers by the minimum diameter it could have, assuming 100% absorption.

As discussed in Sec. 4.1, non-uniform surface deformation of the optics will scatter power into higher-order spatial modes in the interferometer's coupled cavities. If close to resonance, some of these modes will resonantly extract power from the fundamental mode, resulting in losses. The time constant of loss via scatter from a point absorber decreases with the order of spatial mode power is scattering into. When first pumped, the high spacial frequency deformation of the small point absorber has higher overlap with higher order optical modes. As the heat dissipates, the width of the point absorber deformation grows and lower order modes are excited.

Loss is observed as a decrease in the power recycling cavity gain immediately after power-up as the point absorber is first pumped and the scatter process is initiated. At LLO, we observed loss with a time constant of approximately 200 s, consistent with models of the time constant from point absorber-induced scatter into HOM7. During pre-O3 commissioning, LLO effectively minimized loss from the largest point absorber on ETMY by decreasing the overlap between the circulating arm field and the region of high absorption. By moving the beam approximately 3 cm on ETMY, thermal distortion from the ETMY point absorber decreased by a factor of 0.56 and arm power increased by a factor of 1.42. Results of decreased optical path distortion due to decreased power pumping the point absorber shown in Fig. 4.9. The move recovered about 20% power recycling gain - shown in Fig. 4.10. However, the loss dependence on increasing power is still evident in both detectors, likely

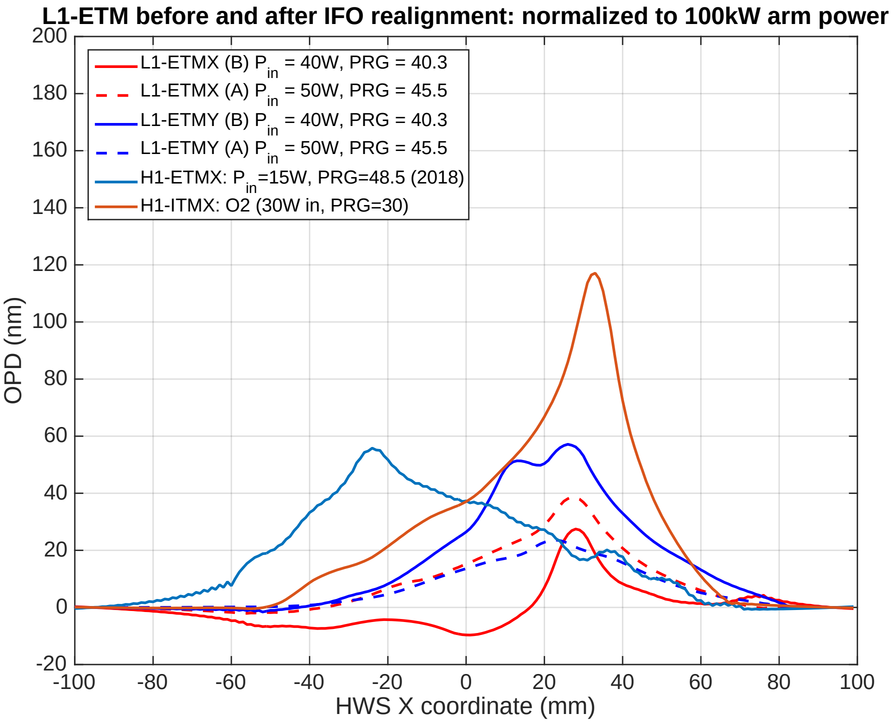

Figure 4.9. Optical path distortion (OPD) across one axis of several optics before and after realigning the LLO Y-arm cavity beam to decrease overlap with the most offensive point absorbers. The decrease in OPD in ETMY is shown between solid and dotted dark blue, compared to the relatively static red traces. For comparison, two OPDs of LHO optics with large point absorbers are also shown in the highest traces (orange and light blue). Plot by A. Brooks.

from continued scatter from non-uniform absorption.

During a mid-O3 vent, LLO's ETMY was inspected for evidence of the main point absorber. It was found that a $\sim 100\,\mu$m spot was void of coating in the location identified by the HWS, suggesting a particulate that had been vaporized with the high circulating power.

Mitigation of point absorbers will require eliminating their introduction into the test mass coating process or a multi-array surface deformation compensation heater [37].

4.4 Laser noise coupling

We recall from Sec. 2.4.1 and Fig. 2.4 that aLIGO employs two intentional length imbalances: the macroscopic Schnupp asymmetry in the Michelson length and the microscopic

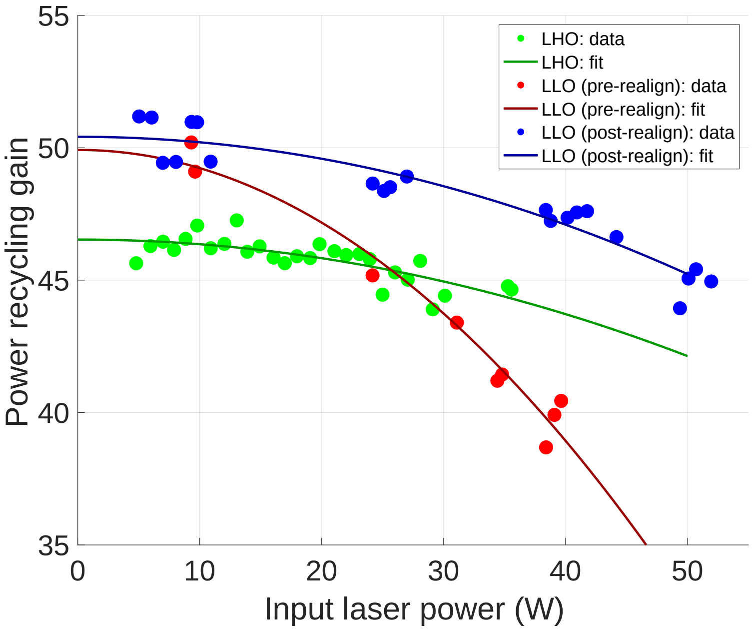

Figure 4.10. Power recycling gain dependence on input laser power, showing power dependent loss. Red and blue dots show before and after spot move, respectively, at LLO. LHO shown in green. Plot from [36].

dc readout offset in the differential arm lengths. This directs some carrier light to the antisymmetric port, carrying common-mode noise. As discussed in Sec. 4.1, thermal-induced mismatches between the arms couples additional power to the antisymmetric port. In this section, we discuss the impact of these mismatches on laser noise coupling. The thermal compensation system discussed above is designed to compensate imbalances between the coupled cavities and reduce frequency and intensity noise couplings. Reducing coupling by equalizing the ITM substrate lenses was explored previously in [13] at approximately 100 kW circulating arm power. Here we discuss coupling reduction by equalizing cavity parameters with ring heater tuning; the measurements discussed below are with 170 - 270 kW power.

4.4.1 Frequency noise

The freerunning NPRO has phase noise around $100\,\mathrm{Hz}/\mathrm{Hz}^{1/2} \times (100\,\mathrm{Hz}/f)$; the sensitivity goals of aLIGO require this to be stabilized by an additional seven orders of magnitude. A

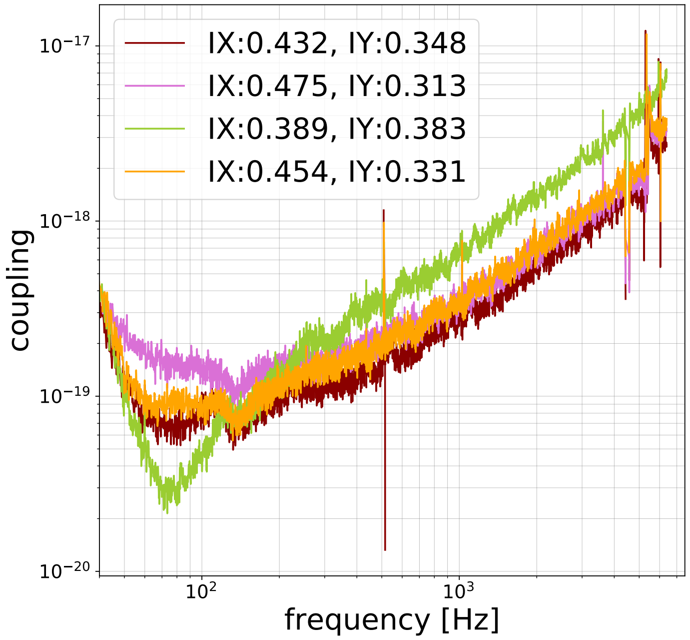

Figure 4.11. Frequency noise coupling at various ITM ring heater differential settings at LLO. Common ring heater power was 0.386 W. Measurement in [38].

multilayered stablization scheme using a reference cavity on the PSL table, the input mode cleaner, and the common mode arm length effectively accomplish this suppression [7]. For aLIGO, noise in the error signals of this frequency stabilization system limits the residual frequency noise of the beam entering the interferometer to approximately 10^{-6} Hz/Hz$^{1/2}$ between 10 and 100 Hz, and increasing as f above 100 Hz.

Frequency noise gets passively filtered by the common mode rejection in the interferometer at frequencies above the common mode cavity pole (0.6 Hz). However, a small amount of noise couples to the antisymmetric port through the intentional arm length asymmetry (dc offset): the length offset slightly detunes each arm from resonance, which converts frequency noise fluctuations to differential arm power fluctuations. Additional coupling occurs if the arm cavities are imbalanced; the differential field component couples directly to the antisymmetric port, carrying the laser noise.

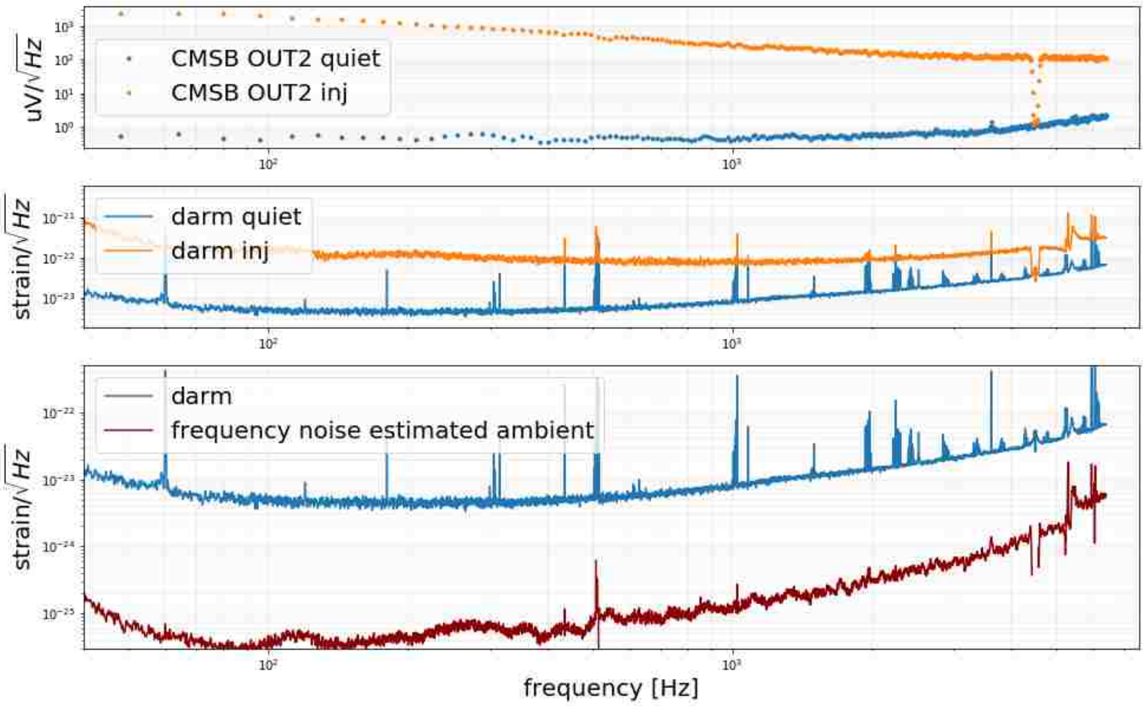

Figure 4.12. Measurement and noise projection of laser frequency noise post minimization during O3. The top panel shows noise as witnessed by the common mode servo board during injection and nominal quiet. Middle panel shows DARM strain during same injection and quiet. Bottom panel shows frequency noise projection relative to quiet DARM. Full description of measurement in [38].

Tests to minimize frequency noise coupling using ring heater thermal compensation were carried out during O3, at nominal operating power. Frequency noise is amplified by broadband injection into the common mode stabilization loop servo board input; an out-of-loop pick-off from the output of the same servo board is used as the witness sensor. The excitation is strong enough such that DARM is excited by approximately an order of magnitude. Couplings were measured for a series of differential ITM ring heater settings. Results are shown in Fig. 4.11. A differential settings range was found that minimizes coupling, with some residual noise remaining; outside of this band, a small change in differential ring heater setting increases coupling significantly. The minimized frequency noise estimated ambient relative to DARM strain is shown in Fig. 4.12. It is possible this is a local minimum; a full landscape of common and differential settings was not quantitatively explored.

4.4.2 Intensity noise

The relative intensity noise of the light out of the 70 W amplifier is roughly 10^{-6} Hz/Hz$^{1/2}$. Two loops are used to stabilize this by several orders of magnitude to within aLIGO sensitivity requirements: an error signal from the PMC and a signal from the the IMC transmission, both of which are fed back to an acousto-optic modulator (AOM) after the amplifier. Finally, intensity noise in the interferometer gets passively filtered by virtue of the common mode rejection at frequencies above the common mode cavity pole (0.6 Hz).

Intensity noise couples to the gravitational wave readout by the field arising from the DARM offset and Schnupp asymmetry as the light leakage to the AS port is directly modulated by the input laser intensity noise. Additional coupling occurs at frequencies below 50 Hz through the conversion of intensity fluctuations to radiation pressure forces; if there are mismatches in the mirror masses or the power circulating in the arms, then the differential radiation pressure responses will produce a differential length signal. At higher frequencies (above 100 Hz), intensity noise coupling is dominated by surface deformations - such as point absorbers - which scatter light out of the fundamental mode in the cavity into higher-order spacial modes. These modes - not resonant in the arm cavity - are not filtered by the common-mode coupled cavity pole and thus couple intensity noise to the dark port [13].

To measure coupling, the intensity stabilization servo outer (IMC transmission) loop is turned off (to avoid suppression) and a broadband excitation is injected. Out-of-loop photodiodes of the outer loop are used as witness sensor. The excitation is strong enough such that DARM is excited by approximately an order of magnitude. Intensity noise coupling measurements are shown in Fig. 4.13. Multiple coupling investigations while tuning ring heater settings found that different ring heater corrective settings were required to minimize

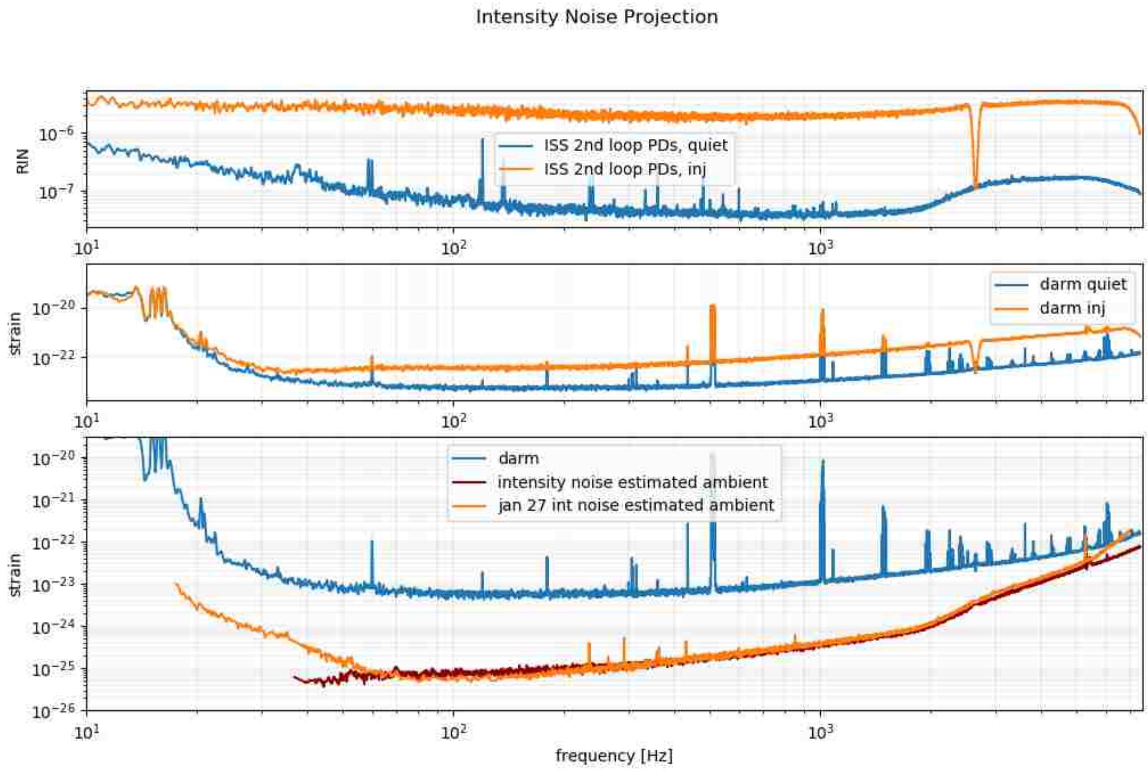

Figure 4.13. Measurement and noise projection of laser intensity noise. The top panel shows example of relative intensity noise (RIN) as witnessed by the photodiodes in the 2nd loop of the Intensity Stabilization Servo (ISS) during noise injection and a nominal quiet time with no injection. Middle panel shows DARM strain during same injection and quiet. Bottom panel shows intensity noise projection relative to quiet DARM. Two projections are shown, one when Y-arm beam was strongly overlapped with a point absorber (orange) and one after the arm beam has been realigned for lower overlap (red). Note the increased low and high frequency projection in orange. Red trace does not extend down in frequency as far due to lack of excitation of DARM from low coupling below 40 Hz. Full description of measurement in [39].

frequency or intensity noise. A comparison of Figs. 4.11 and 4.14 – showing frequency and intensity noise coupling at various differential ITM ring heater settings from common 0.386 W – finds intensity noise minimized with 0.01-0.1 W more differential ITM ring heater power.

The effect of scatter-inducing point absorbers on intensity noise coupling was investigated. Point absorbers (see Sec. 4.3.2) affect intensity noise coupling at both low and high frequency. Large beam overlap with a point absorber in one test mass scatters power out of the fundamental mode into higher order modes, leading to differential arm power (lower

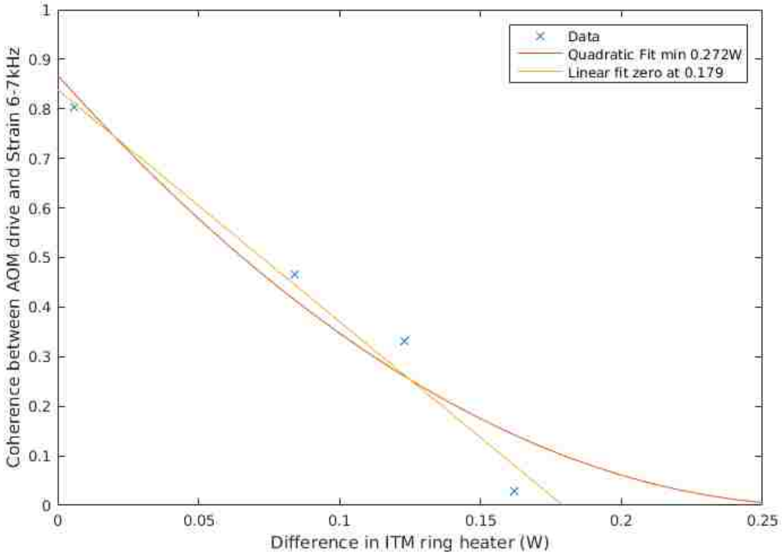

Figure 4.14. Relative intensity noise coupling at various differential ring heater settings, same as those in Fig. 4.11. Plot by C. Blair [38].

power in the arm with the absorber) and increased unfiltered higher order mode content in the arm with the strong point absorber. Common intensity noise with differential arm power causes differential radiation pressure noise; this directly converts to differential arm length fluctuations, coupling intensity noise at low frequency with a dropoff with increasing frequency due to attenuation from the pendulum response. Intensity noise coupling measurements were taken before and after realigning the Y-arm away from a strong point absorber on ETMY. Intensity noise projections under DARM at that time are shown in Fig. 4.13; overlap with the point absorber led to increased coupling at low frequency due to differential arm losses (below 60 Hz) and high frequency due to increased power in high order optical modes (above 5 kHz). Coupling at low frequency (via radiation pressure forces) goes as approximately $1/f^3$. Since the coupling is flat at high frequencies, the rise after 5 kHz is a real increase in noise. The transverse mode spacing of the arm cavity is around 5 kHz and the point absorber is likely scattering power into the second order transverse mode, causing increased noise centered around 10 kHz; a higher rate measurement is required to verify this.

A simple model of power differential radiation pressure-induced relative intensity noise

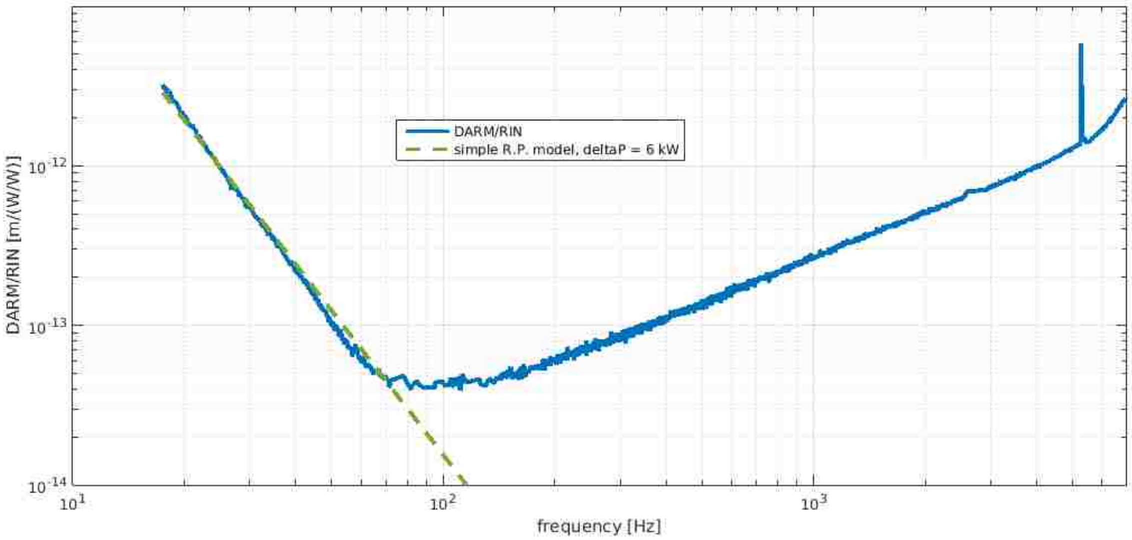

Figure 4.15. Intensity noise coupling to DARM during large overlap with a point absorber on ETMY is shown in blue. The dotted green line is a simple radiation pressure RIN model following Eq. 4.5, with ΔP scaled to best fit the low frequency data. In this case, ΔP ~6 kW. Measurement in [40].

(RIN) coupling can be made according to the equation

$$\frac{DARM}{RIN} = \frac{2\Delta P_{arms}}{c\mathrm{m}\omega^2} \times \frac{\mathrm{RIN}_{arm}}{\mathrm{RIN}_{input}} \tag{4.5}$$

where $\mathrm{RIN}_{arm}/\mathrm{RIN}_{input}$ is essentially the double cavity pole (since input RIN is filtered by this transfer function), ΔP_{arms} is the DC power difference in the arms, m is the mirror mass, and c is the speed of light. By scaling ΔP_{arms} to match the model to the measured coupling function, an estimate of the difference in arm power can be made. Prior to the spot position change, ΔP_{arms} ~6 kW, shown in Fig. 4.15. After the change, there was no dominant low frequency component in the coupling function, but an upper limit can be set of 0.5 kW. The pre-spot move ΔP found a 3% arm power difference between the arms; this was corroborated with a different arm power measurement methodology discussed in [41].

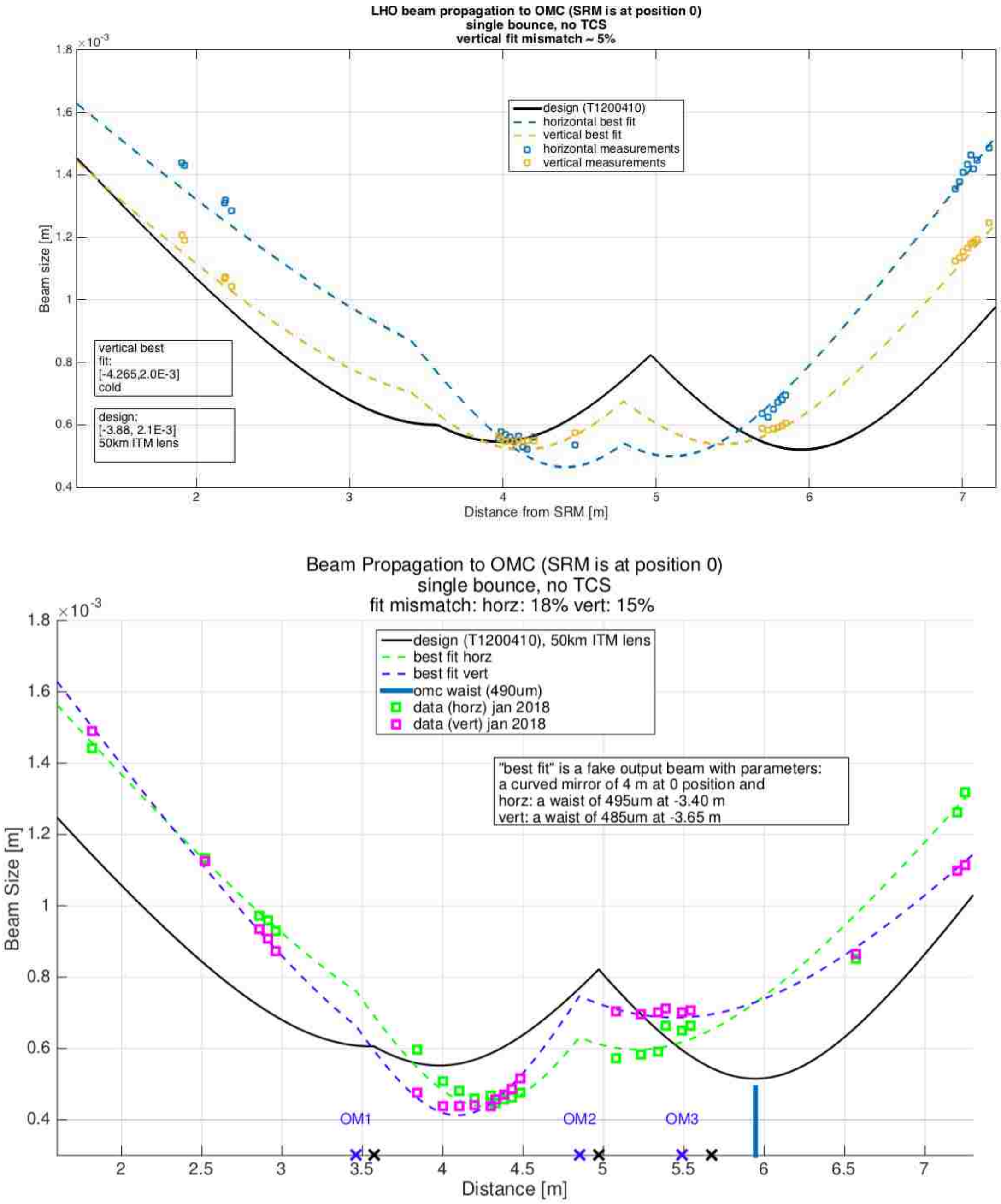

Figure 4.16. Caustic measurements of output beam at LHO (top) and LLO (bottom) prior to O3. Markers indicate in-chamber measurements, in vertical and horizontal. Astigmatism is apparent at both sites. Bottom plot shows location of 'OM' steering mirrors before OMC; black crosses show design locations and blue crosses show measured locations at LLO. The black trace shows design beam, though this includes a 50 km thermal lens in the ITM which is not accounted for in the measured data fits. LLO measurements by Anamaria Effler.

.

4.5 Output beam modematching

The work discussed previously in this chapter investigates mode matching between the fields circulating in each arm and the fields in the recycling cavities. The final power incident on the dark port photodiodes also depends on the modematching between the interferometer and the Output Mode Cleaner (OMC).

An in-chamber caustic measurement of the output beam was measured at both sites. Measurements were taken in single-bounce configuration: the ETMs, one ITM, and recycling mirrors are misaligned, so that there are no resonating cavities and the input beam does a single bounce off of one ITM before impinging on the OMC. Results are shown in Fig. 4.16. Measurement details can be found in [42] and [43]. Beam waist data is then fit with a MATLAB simulated arm beam that has been propagated through the ITM, BS, and SRC (though the propagation here does not include a 50 km lens assumed in the black design trace).

Discrepancy between single bounce and full IFO configuration hinders a full understanding of the implications of the single bounce measurements on low noise, high power operations. Most ideally, high power would only significantly change the ITM thermal lens. This can be added to the model when propagating an ideal beam from the arm to the output; this more closely matches the design beam parameters. However, in reality, the full interferometer configuration producing the output beam depends on the IFO operating point, cavity round trip variables, and optical suppression of the higher order modes - variables that are often unknown or increasingly difficult to model. The effect of resonant cavities on mode shape strongly changes the This prevents full IFO conclusions being accurately drawn from single bounce measurements.

4.5.1 Signal recycling mirror lens tuning using CO_2

As the OMC is a fixed bowtie cavity and the mode coming out of the interferometer is variable, a dynamic lens between the two would provide necessary actuation ability to

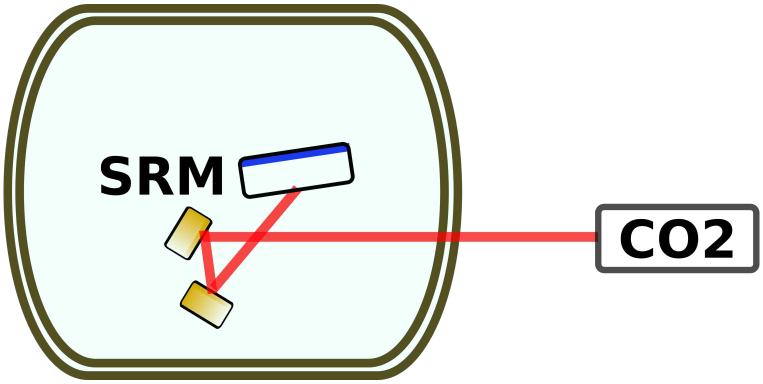

Figure 4.17. Basic set up of the in-air CO_2 laser injected into HAM5 and steered onto the back side of the SRM via two gold-coated copper mirrors.

.

optimize output power. If an arm cavity mode is modelled and propagated to the OMC waist, almost all cases within the uncertainty distribution are improved with a positive thermal lens in the SRM substrate. The idea is to use a CO_2 laser incident on the SRM substrate to create a tunable IFO-to-OMC modematching lens, in the same fashion as the ITM compensation plates. A design was developed that injects an in-air CO_2 laser into the vacuum system through a viewport on HAM5. The beam is steered onto the anti-reflective side of the SRM via two 2" gold-coated copper mirrors, see Fig. 4.17. In-vaccuum optics were installed in Fall 2017.

A first test of a prototype system was carried out in early 2018 [44]. A low-power Access L3 400 mW laser and steering optics were housed in an optical enclosure which was mounted to the viewport. A visible co-aligned red laser was necessary for alignment onto the SRM. A 5 mm radius CO_2 beam in a central heating pattern created a peak thermal lens of 10.5 mDiopters in the SRM. To test modematching, the interferometer was put in single-bounce configuration; while this gives a measurement of modematching between input field and OMC, it was assumed that this mimics full interferometer modematching, as the arm and recycling cavities are well modematched to the input field. The transmission through the OMC was improved by approximately 4.4%, from 87% to 91%.

Fitting the data from the 400 mW prototype system estimated a need for 1.5 W of central

CO_2 power to move through maximum mode matching. Additionally, a more sturdy, quieter hardware set up would be required for low noise operations. A higher power laser was characterized, temporarily installed, and tested in single bounce and full interferometer, low noise configurations.

First, a test bed was set up at Caltech to characterize the higher power CO_2 laser prior to testing at a detector. The power transient and stability were measured. The power settled to within a few mW after approximately 13 minutes at 0.5W, 1W and 1.5W output power tests. No significant variation in the output power was observed at the measured timescales in this setup. The polarization out of the laser was found to vary but up to 8.8% and a polarizer + half-wave plate should be placed before the pickoff that is used for power monitoring during usage. A caustic measurement was performed and the beam waist was located 370 mm from the output of the laser with a beam radius of 1.5 mm.

The injected CO_2 beam hits the back of SRM with a 25 degree angle of incidence which, if not corrected for, introduces astigmatism in the SRM lens. A 25 degree angle of incidence projects a heating beam onto the SRM that is 10% larger in horizontal beam size than vertical. COMSOL predicts a roughly 5% reduction in the horizontal lens strength relative to the vertical lens strength. If we take the average of the horizontal and vertical lens strengths as a metric and assume strengths around 60 mD, then around 100 ppm is scattered out of the TEM00 mode of a 5% astigmatic lens compared to a purely spherical lens. Such a small effect means there is no need to correct for this astigmatism.

The laser injection system was installed on a temporary in-air optics table next to HAM5 (the chamber housing the SRM). The table setup at LLO is shown in Fig. 4.18. The SRM CO_2 heating was tested in two configuration: a central heat load creating a positive lens in SRM, and an annular heat load creating a negative lens, see Fig. 4.19. The annular beam was created by mounting two ZnSe axicons and a lens before the periscope.

A first test with 1 W central CO_2 in full lock with 45 W input power showed a loss of optical gain of about 2%, contrary to the modematching direction extrapolated from the

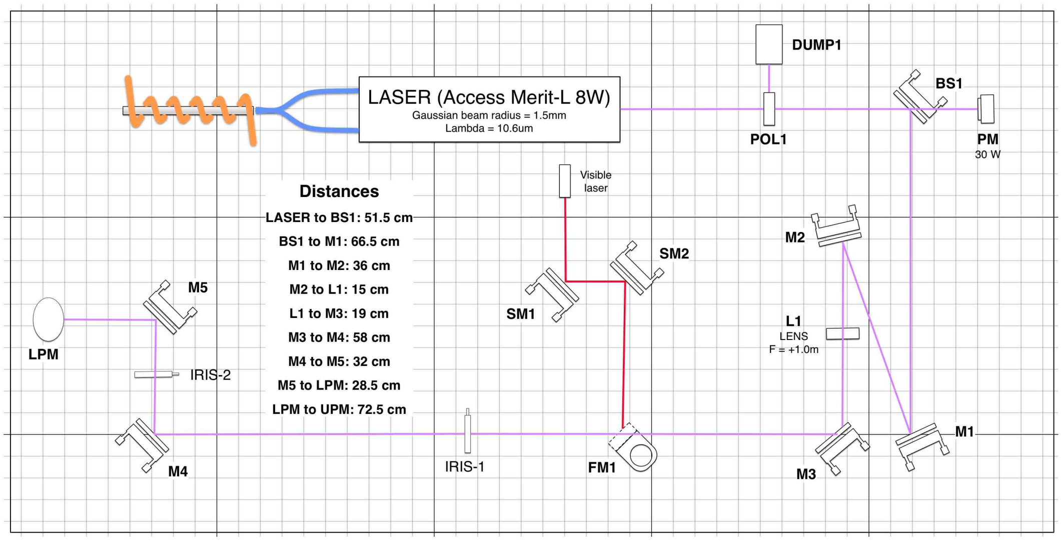

Figure 4.18. Setup of the 8 W SRM CO_2 and alignment laser (red) in-air breadboard. Distances not to scale. After reaching the lower periscope mirror (LPM), the beam is directed up a periscope and into the vacuum system through a viewport.

prototype test results. As the latter was taken in single bounce configuration, the error in assuming the single bounce and full IFO configuration were interchangeable up to some modemismatch percentage became clear. To move in a direction of increased mode matching in full lock, the CO_2 injection set up was reworked to project an annular pattern onto the SRM.

Creating an effective annular heating pattern proved difficult. Over the long propagation distance in vacuum, the axicon ring beam resulted in a bessel beam, and precise tuning of the axicons and a lens were required to land the desired annular pattern on the back face of the SRM. A tight (< 10 mm) annular heat pattern quickly diffused into an effectively central heat pattern within the SRM. Final tests were conducted with a heating ring diameter of 15 mm.

1 W annular CO_2 was applied on the SRM in several different input powers in full lock configuration. The mode matching deteriorated with annular CO_2 by about 1% at 10 W IFO input power and 0.25% at 25 W. At 40 W, a fraction of a percent improvement in mode matching was observed. These measurements provide weak evidence that annular

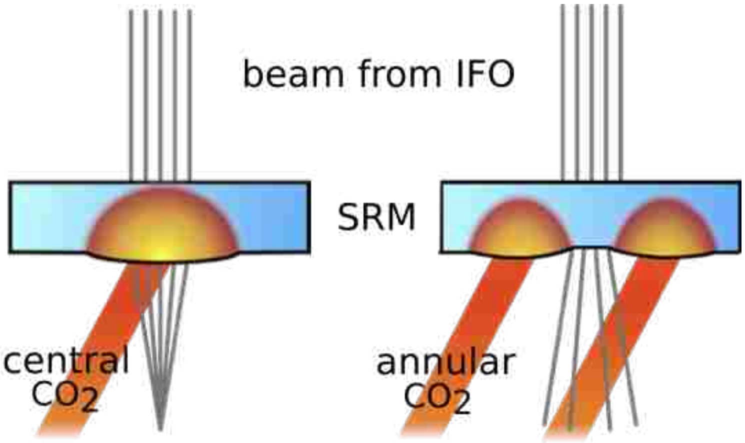

Figure 4.19. Central or annular CO_2 projection patterns to create a positive or negative thermal lens in the SRM.

SRM heating is required to improve OMC mode matching assuming optimal ITM thermal lens for OMC mode matching (complimenting the previous SRM central heating experiment conclusion). Fitting these measurements suggest mode matching could be only marginally improved (<1%) with order 1 W annular CO_2.

5 Parametric Instability

A significant technical challenge of high power operation involves an opto-mechanical interaction between the laser field and the test masses that can create an unstable feedback loop. When the mechanical motion of a test mass resonance scatters light into a higher-order optical mode, the optical energy stored in the cavity can in turn apply radiation pressure back onto the test mass such that the mechanical motion is amplified. This process can result in an instability that exceeds the limits of control loops and render the interferometer inoperable. The interactions - known as 'parametric instabilities' - grow more problematic with higher power and first hindered LIGO operations in 2014.

Schemes to avoid parametric instabilities fall under two domains: those that reduce the mechanical motion of the test mass and those that modify the optical mode overlap. Test mass mechanical mode Q-factor reduction can be active - with control loops that actuate against the test mass bulk motion - or utilize passive dampers. Optical-mechanical mode overlap modification works by tuning the radius of curvature of an optic to modify the arm cavity geometry and thus change the optical mode spacing. All these methods have been successfully implemented at LIGO detectors at various detector operating powers and are discussed in detail in the following sections.

The first section of the chapter reviews the mechanism behind parametric instability. The following sections walk through the four schemes that have been implemented to mitigate parametric instability. The work presented comprises a significant focus of the author's dissertation work. Work was split between both LHO and LLO and is presented by the author and others in [45–47].

First, we review the opto-mechanical interaction that gives rise to parametric instability (PI).

5.1 Background

PI is a run-away mechanism that can occur when the frequency of an internal mechanical mode of an optic is close to the beat frequency between the fundamental mode and a

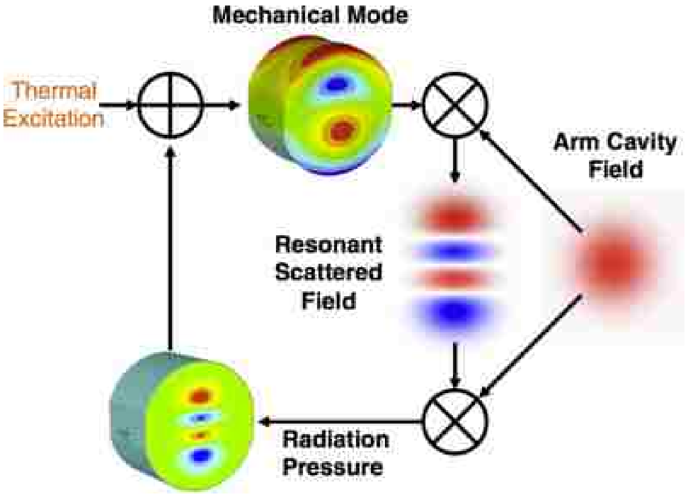

Figure 5.1. Parametric instability (PI) feedback loop: mechanical motion of the test mass can scatter light into a higher order optical mode which then puts radiation pressure back on the optic, reinforcing the mechanical motion.

higher-order optical mode present in the cavity. The full interaction is illustrated in Fig. 5.1. Ambient mechanical motion of a test mass eigenmode scatters light out of the fundamental and into a higher order mode in the arm cavity. The beat between the two modes in turn applies radiation pressure back onto the test mass at the mechanical mode frequency. If the transverse amplitude distribution of this field overlaps the spacial surface profile of the generating mechanical mode and if the field is in phase with the motion, the radiation pressure reinforces the surface motion, creating a feedback loop. If the optical energy imparted to the mechanical mode exceeds its dissipation, this results in an instability which can grow beyond the limits of the cavity control systems.

If we model this mechanism as a classic feedback loop [48], the parametric gain of the loop for a particular mechanical mode m in a single cavity is

$$R_m = \frac{8\pi Q_m P}{M\omega_m^2 c\lambda_0} \sum_{n=1}^{inf} \Re[G_n] B_{m,n}^2 \tag{5.1}$$

where Q_m is the quality factor of the mechanical mode, P is the circulating power in the cavity, M is the mass of the optic, ω_m is the mechanical frequency, G_n is the optical transfer function, and $B_{m,n}$ quantifies the spacial overlap between the optical field pressure distribution and the mechanical motion pattern. The linear dependence on power makes parametric instability a greater threat as circulating power is increased in Advanced LIGO.

Parametric gain R_m depends on the beat frequency between the fundamental optical mode and higher order optical modes resonating in the arm cavities of the interferometer. We consider a single cavity as an approximation of the optical mode behavior in a LIGO arm cavity [see section **??** for the limitations of this model]. In a cavity of length L, the optical beat note spacing $\Delta\omega_{pq} = |\omega_{00} - \omega_{pq}|$ between the TEM$_{00}$ and TEM$_{pq}$ modes is dependent on radius of curvature such that

$$\Delta\omega_{pq} = (p+q)\frac{c}{2\pi L} cos^{-1}\sqrt{(1-L/R_1)(1-L/R_2)} \tag{5.2}$$

where $R_{1,2}$ are the radii of curvature of each optic. For the LIGO arm cavities, using measured radii of curvature of the cold test masses, $c/2L = 37.5\,\mathrm{kHz}$ is the free spectral range and $\Delta\omega_{pq} \sim (p+q)5.1\,\mathrm{kHz}$. PI in Advanced LIGO thus involves the interaction of mechanical modes that have eigenfrequencies near multiples of 5.1 kHz and whose surface deformation mimics the higher order beat note pressure distribution shapes.

Parametric gain changes the time constant (time to build up by a factor of e) of the mechanical mode such that

$$\tau_{pi} = \tau_m/(1 - R_m), \tag{5.3}$$

where τ_m is the time constant of the mode with no three-mode parametric influence. As the Q-factor can be ascertained by the time constant - $Q = \tau\pi f_m$ - measuring the ring down of a mode while the interferometer is locked proves a tool for evaluating the state of parametric gain.

5.2 Electrostatic damping

This section discusses the electrostatic damping mitigation technique, which decreases parametric gain by actively damping the test mass mode involved in the interaction. It

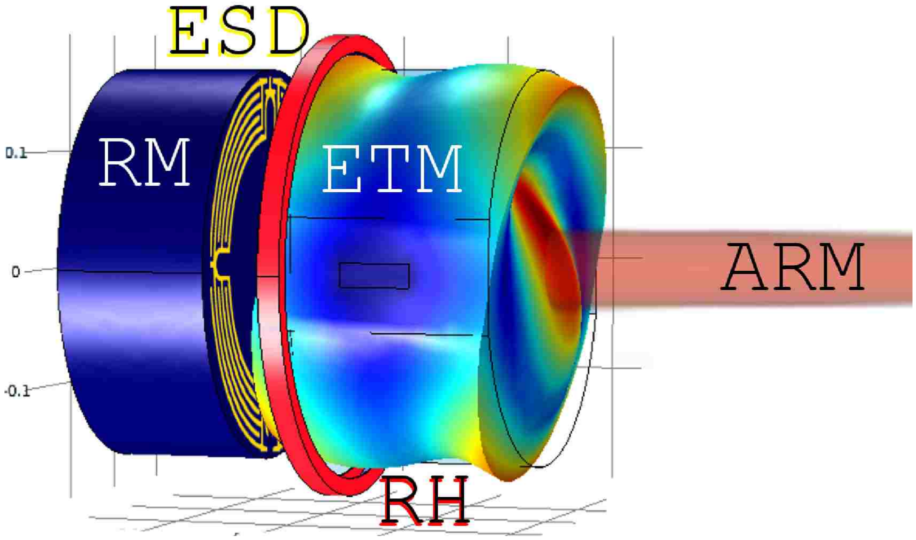

Figure 5.2. Schematic of the test mass and reaction mass, showing the gold ESD comb on the reaction mass (RM). The ring heater (RH) is shown surrounding the ETM. The ETM has exaggerated deformation due to a 15.5 kHz mechanical mode, where the color represents the magnitude of the displacement (red is large, blue is small). The distance between the reaction and test mass is exaggerated by a factor of 10 in order to show the ESD. The circulating laser power is depicted in red.

utilizes the electrostatic drive hardware already in place for unrelated test mass control in aLIGO. This technique was successfully used for PI mitigation at LHO during O2 and the setup, installed at both sites, is also crucial for PI characterization. Results are presented in [45]. The author contributed significantly to the infrastructure setup, commissioning, analysis, and continual running of the electrostatic damping scheme during O2 alongside C. Blair at both sites.

Advanced LIGO utilizes Electrostatic Drives (ESDs) to control the bottom pendulum stage of the test mass chains. The ESD consists of a comb of gold conductors on the reaction mass in a symmetric pattern of four electrode pairs, depicted in Fig. 5.2. When voltages are applied to the electrodes, the potential difference between the electrode pairs creates fringing electric fields. These fields attract the dielectric test mass with an electrostatic force (per quadrant) of

$$F_{ESD} = \alpha \frac{1}{2}(V_{bias} - V_{app})^2, \tag{5.4}$$

where α is the force coefficient and $V_{bias} - V_{app}$ is the potential difference between the electrode pairs in a given quadrant; for nominal interferometer control operation we apply a constant V_{bias} and vary V_{app} for control. The main purpose of the ESDs is to provide quiet arm length control at frequencies which higher pendulum stage control cannot apply effective forces. The quadrature pattern of the electrodes allows for pitch and yaw actuation.

The active PI damping concept utilizes the ESD actuation force to modify the Q-factor by driving the optic at the mechanical mode, m, frequency with a force pattern that overlaps the mode's surface motion displacment, $\vec{u}_m$ [49]. A portion of F_{ESD} couples to the mechanical mode:

$$F_{app,m} = b_m \alpha \frac{1}{2}(V_{bias} - V_{app})^2, \tag{5.5}$$

where b_m is the force coupling between the ESD and the mechanical mode,

$$b_m = |\iint_S \vec{f}_{ESD} \cdot (\vec{u}_m \cdot \hat{z})\, dS|. \tag{5.6}$$

To implement active damping, specialized control systems were developed. Error signals are derived from the quadrant photo detectors (QPD) in transmission of the ETMs and/or the DC photo detectors (DCPD) in transmission of the output mode cleaner. With a suitable combination of quadrant signals, the end QPDs see the beat signal between the fundamental and higher order optical mode that is being excited by the relevant mechanical mode of that arm. The mechanical modes are visible in the OMC DCPDs via the differential arm length caused by the motion of a particular mirror.

The frequency range of PI requires a high data sampling rate to resolve modes up to tens of kilohertz. For more efficient processing, the error signals are demodulated to a 2 kHz band, processed, then modulated back up to drive the optic at the mode frequency. Once downconverted, each error signal is bandpassed around the particular mechanical mode of interest (5 Hz wide bandpass), then phase shifted to produce a control signal that is out of phase with the resonant motion. Once upconverted back up to the PI band, the damping

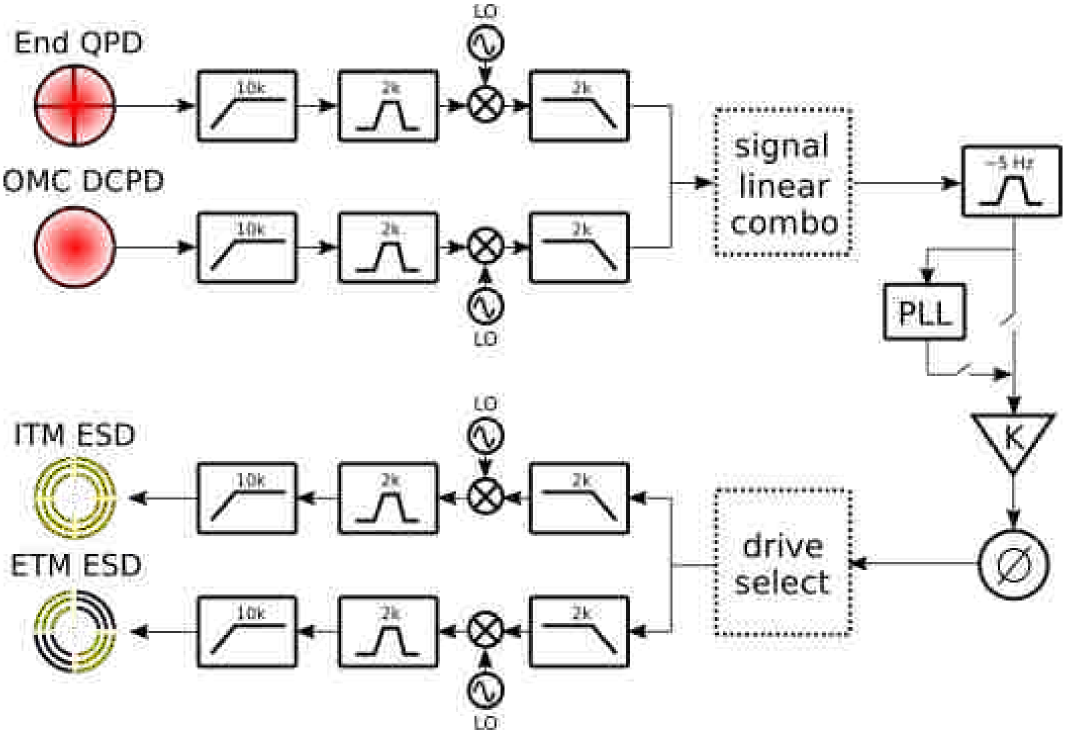

Figure 5.3. Signal flow of ESD damping scheme.

force is applied to the relevant optic with adjustable gain. In this way, the ESD force counters the mechanical motion of the optic, effectively reducing the Q-factor. For the ETMs, two opposite quadrants of the ESD are available; for the ITMs, all four quadrants can be driven. The quadrants can be driven in or out of phase with one another to best mimic the shape of a particular mechanical mode. A full schematic of the ESD damping signal flow is shown in Fig. 5.3.

Electrostatic damping of PI was first demonstrated at LHO in 2016 [45], shown in Fig. 5.4. Using thermal compensation (discussed in Sec. 5.3), the ETMY 15538 Hz mechanical mode was made parametrically unstable. The amplitude of the mode grew with a time constant of 182 seconds and, once it was sufficiently excited, the ESD damping loop was turned on. Error signal from the Y-End QPD was used to drive ETMY ESD, effectively damping the resonant motion and reducing the Q-factor of the mode. Using Eq. 5.3, time constants before and after show a parametric gain decrease from 2.4 to 0.18.

With the successful demonstration of ESD damping, the scheme was extended for use on

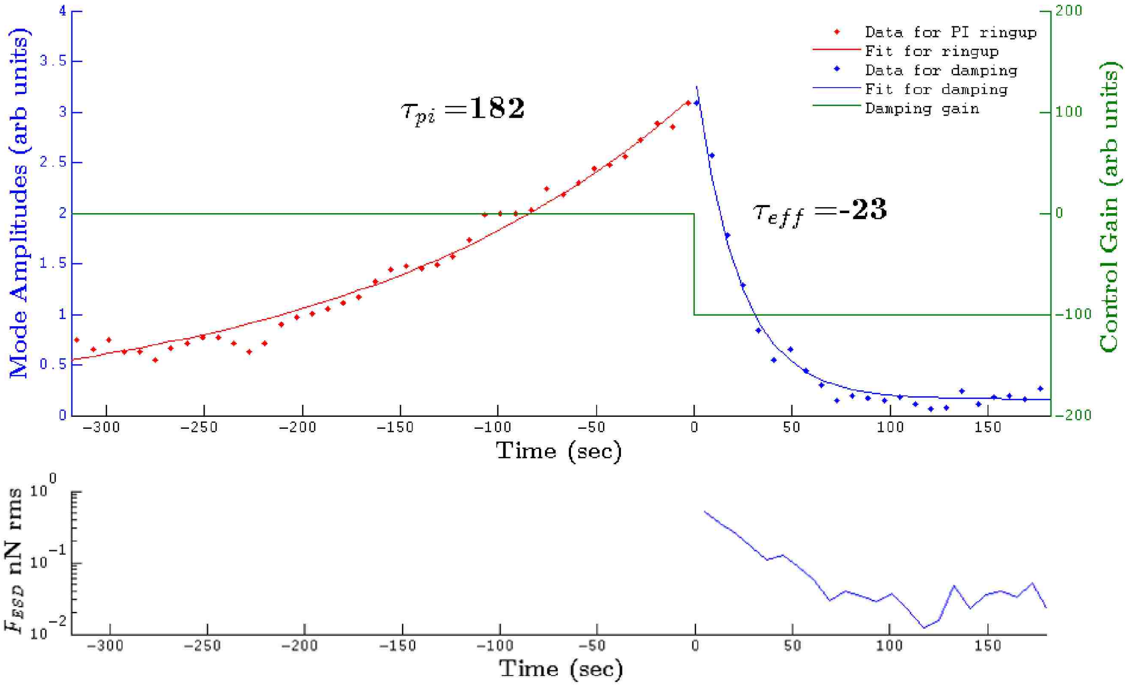

Figure 5.4. First demonstration of damping a mechanical mode using electrostatic drive system. The amplitude of the mechanical mode (witnessed in the OMC DCPD) grows with unstable parametric gain. At t=0, the ESD damping control gain is turned on and the mode amplitude decreases. The control force is shown in the lower panel. The time constants of the ring up and controlled ring down are overlaid.

all test masses at both sites. During O2, active damping was engaged on 13 modes across both the sites, including the 15, 15.5, 32.7, 47.5 and 47.7 kHz mode groups. Phase locked loops were implemented for each damping loop and user-friendly interfaces were developed for tracking and changing PI. The ESD control infrastructure gave the additional benefit of the ability to manually excite mechanical modes. By driving the actuation in-phase, a mechanical mode can be excited to orders of magnitude above its ambient level. If the drive is then turned off, the ring down of the mode can be measured by monitoring the amplitude decay. This measurement technique has been crucial in assessing the effectiveness of other PI mitigation schemes, such as will be discussed in Sec. 5.6. It has also been necessary for three mode interaction monitoring, discussed in Sec. 5.5

Although the technique was successful at damping ∼10 modes at ∼100 kW circulating power, several issues make ESD damping insufficient for full Advanced LIGO design power:

Phase changes As the interferometer goes through a thermal transient (Sec. 5.3), the opto-mechanical overlap changes, thus changing the control loop phase. This requires additional manual phase tuning on top of the PLL. Accounting for the phase shift would require a complete understanding and model of the real-time transient cavity geometry.

Overlapping mechanical modes Mechanical modes across the four different test masses can be very close in frequency; if too close, the PLL cannot differentiate. Band passes can be made very thin to differentiate separate control loops for each mode, but must be kept wide enough to cover the full thermal shift (see next item).

Thermally driven mechanical mode shifts As the test mass heats up with high circulating power, the change in Young's modulus causes the test mass resonances to change by up to several hertz. Once in steady state, temperature fluctuations of the test mass are dominated by ambient temperature changes of the environment outside the vacuum chamber. Each test mass then experiences unique temperature changes (especially the ETMs); one mechanical mode may sweep through the frequency of another test mass's mode. The PLL cannot differentiate during this process, manual interaction is required to reestablish damping. Efforts to track unique modes and subtract the other test mass from the loop proved to be difficult. Efforts to actively alter the bandpass to center on the moving mechanical mode peak were only somewhat successful, hindered by low SNR of the peak at times, as well as the previously discussed mode crossings.

5.3 Thermal compensation

This section discusses mitigating PI by using the ring heaters to alter the arm cavity parameters so as to decrease the coincidence of the three mode interaction.

In the single cavity configuration, the optical transfer function between the mechanical mode and optical field is

$$\Re[G_{pq}] = \frac{c}{L\pi\gamma(1 + \Delta\omega^2/\gamma^2)} \tag{5.7}$$

where γ is the optical mode linewidth, and $\Delta\omega = \Delta\omega_{pq} - \omega_m$ defines the frequency spacing between the optical beat note and the mechanical mode. The transverse mode spacing of a

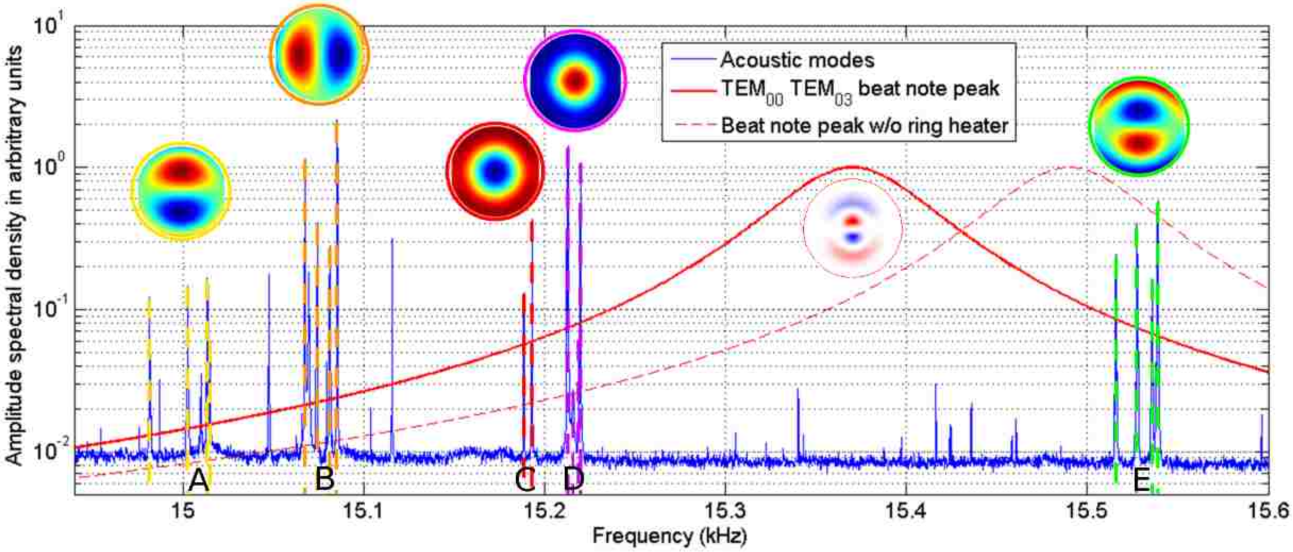

Figure 5.5. Amplitude spectral density of the output photodiode signal showing the mechanical modes (peaks in blue trace) and representation of the optical beat note (red traces) responsible for parametric instability during static thermal compensation. A model of the surface displacement of the test mass due to each mechanical mode is shown above that mode; each mode group has four peaks, one for each test mass.

higher order mode of order $(p+q)$ is given by

$$\Delta\omega_{pq} = (p+q)\frac{c}{L}cos^{-1}\sqrt{(1-L/R_1)(1-L/R_2)} \tag{5.8}$$

where $R_{1,2}$ are the radii of curvature of each optic. Thus, the coincidence of the three mode interaction is modified by a change in the RoC of a test mass, which alters G_n in Eq. 5.1.

As discussed in Sec. 4.2, annular radiative heating elements circling the barrel of the test masses are installed in LIGO to compensate central self heating. These ring heaters (RH) induce a decrease of RoC of the mirrored surface through thermal expansion. In steady state configuration, they result in a static shift of $\Delta\omega_{pq}$ down in frequency by $4\,\mathrm{m_{RoC}/W_{RH}}$.

If we take the derivative of Eq. 5.8 wrt R_1, we get

$$\frac{d\Delta\omega_{pq}}{dR_1} = (p+q)\frac{c}{2R_1^2}\sqrt{(g_2/g_1)/(1-g_1g_2)} \tag{5.9}$$

where $g_i = 1 - (L/R_i)$. Using Advanced LIGO parameters, the higher order mode spacing changes with radius of curvature as $-(p+q)13\,\mathrm{Hz}/\mathrm{m}_{\mathrm{RoC}}$. The third order optical beat note, $\Delta\omega_{03}$, of the LIGO cold arm cavity sits near 15 kHz. There are test mass mechanical resonances at 15 kHz and 15.5 kHz that have been observed to cause PI starting at 50 kW circulating power. Instability can be prevented if $\Delta\omega_{03}$ avoids these two mechanical mode frequency bands. For (p + q) = 3, the optical mode shifts in frequency by 39 $\mathrm{Hz}/\mathrm{m}_{\mathrm{RoC}}$. Thus, 1 W of ring heater power on a test mass will decrease $\Delta\omega_{03}$ by over 150 Hz. By tuning the ring heater power, we can move the optical mode and thus change the opto-mechanical frequency overlap.

This thermal compensation technique has been used to avoid PI at both LIGO detectors. Ring heater power set points are adjusted to tune the thermal steady state away from problematic mechanical modes, decreasing their parametric gain to sub unity. During the first Advanced LIGO Observing Run (O1), static thermal compensation alone was used to successfully avoid PI. A schematic of the mechanical mode and third order optical beat note during O1 operations is shown in Fig. 5.5. There were two unstable modes at that time, one in mode group A around 15 kHz and one in mode group E around 15.5 kHz. The ring heaters were tuned such that the steady state optical beat note sat around 15.3 kHz with about 100 kW circulating arm power.

For the second Observation Run (O2), circulating power was increased at LHO to approximately 150 kW. Active electrostatic damping was also implemented. The increase in optical power in conjunction with point absorbers made controlling PI with static thermal compensation and active damping difficult. Ring heater power was increased so compensate for the additional power in steady state; the effect of the change on a particularly problematic mechanical mode is shown in Fig. 5.6. However, the increased power - and thus increased parametric gain - caused some 15 kHz modes to become unstable during the thermal self heating transient, motivating the dynamic thermal compensation scheme discussed in the next section.

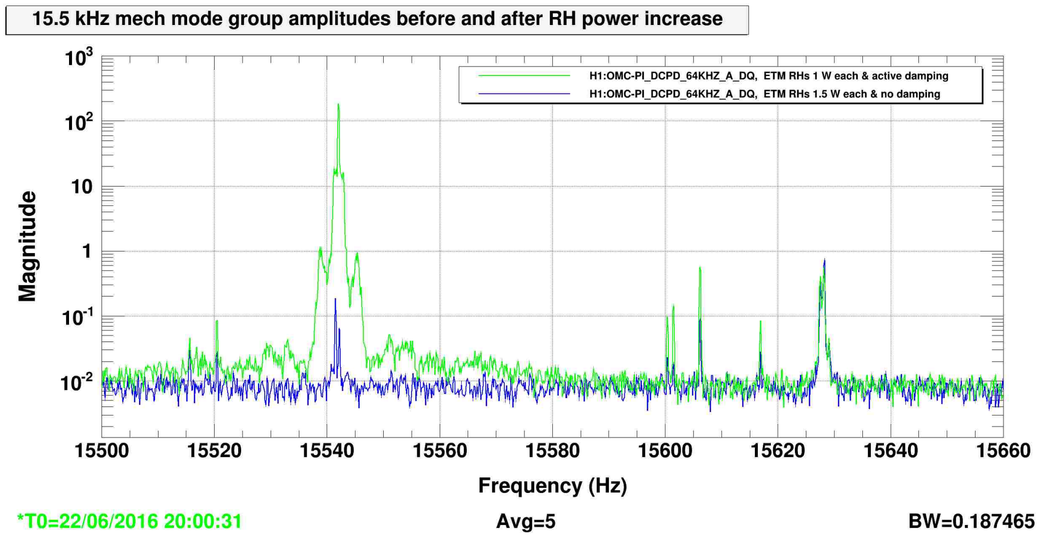

Figure 5.6. The 15.5 kHz mechanical modes during O2, witnessed by the OMC DCPDs, steady state before (green) and after added ring heater compensation (blue) at LHO when circulating power was about 150 kW. Prior to the ring heater increase, active damping with the ESD system was required to reduce the parametric gain of some of the modes. After, no active damping was required.

5.4 Dynamic thermal compensation

In this section, we extend the previously discussed thermal compensation to dynamically control - and thus hold steady - the cavity parameters during the central heating thermal transient. We first walk through the transient nature of parametric instability with high power. We then present simulation, experiment, and results of the dynamic scheme, followed by future improvements and uses. This work was done at LLO and is presented in [47]; modeling was done by V. Jaberian and testing and analysis was led by the author with significant contribution from C. Blair. The optical model extension was explored by A. Green under the direction of the author.

Transient PI

The LIGO test masses have nominal coating absorption of 0.3-0.5 ppm. When the cavity becomes locked (controlled to remain resonant) and power circulating in the arms increases to hundreds of kW, the absorbed power increases to hundreds of mW in the central portion of the test mass. The subsequent radial temperature gradient results in a time-dependent

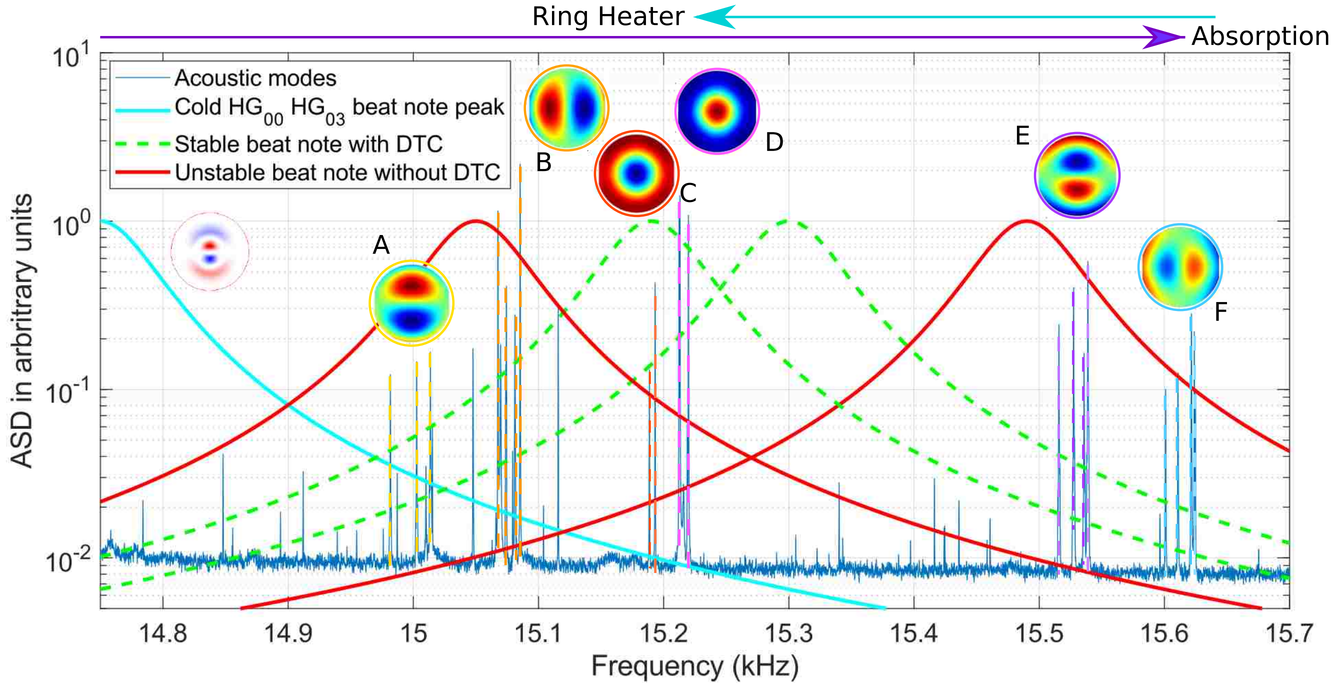

Figure 5.7. Representation of the mechanical modes (blue trace, one peak per test mass at each mode group) and optical beat note responsible for parametric instability during dynamic thermal compensation experiments. Mechanical modes are grouped A-F by mode shape, test mass surface deformation associated with each mode is overlaid, dashed colour lines overlaid on the mechanical modes and circling the surface deformation mark specific modes. The cyan optical beat note shows $\Re[G_{pq}]$ as a function of $\Delta\omega$ for the cold arm cavity; the simulated optical mode is overlaid. Central heating sweeps the optical mode up in frequency. The red curves show locations of instability during this thermal transient. The green curves show the stable tuning range maintained with DTC after the first hour of power up.

surface deformation of the high-reflectively side of the test mass that can be approximated as an increase in the RoC.

For this analysis, we use a single cavity configuration model to approximate the optical mode behavior in a LIGO arm cavity (see section 5.4 for the limitations of this model), utilizing the transverse mode spacing given in Eq. 5.8 and the optical transfer function given in Eq. 5.7. As the mirrors go through a central heating thermal transient, their changing RoC sweeps the cavity optical mode up in frequency by hundreds of hertz, changing how the optical beat note frequency overlaps with the mechanical mode frequencies. The modes of the test masses are temperature dependent, but shift by only a few Hz under typical conditions and thus have negligible impact on transient parametric gain.

The third order optical beat note, $\Delta\omega_{03}$, of the LIGO cold arm cavity sits near 15 kHz. There are test mass mechanical resonances at 15 kHz and 15.5 kHz that have been observed to cause PI starting at 50 kW circulating power [45]. Instability can be prevented if $\Delta\omega_{03}$ avoids these two mechanical mode frequency bands. During power up to 170 kW circulating power, $\Delta\omega_{03}$ shifts up in frequency by ~ 700 Hz, sweeping through both of these mechanical mode groups. The thermal transient is slow enough that parametric instability can occur during these times of frequency overlap and cause the interferometer to lose lock.

Annular radiative heating elements encircling the barrels of the test masses in LIGO compensate central heating. These ring heaters induce a decrease of RoC of the mirrored surface through thermal expansion of the perimeter. From Eq. 5.8, a decreasing RoC results in a decrease in $\Delta\omega_{pq}$ as L/R_n approaches 2. At the time of measurements, LIGO Livingston was operating with static ring heater powers that placed the cold cavity $\Delta\omega_{03}$ at approximately 14.8 kHz.

During O1 and O2, the LIGO Livingston detector was operating with up to 100 kW circulating power. Static thermal tuning was sufficient to avoid parametric gain greater than unity. The central heating transient, offset by the static ring heater setting, resulted in an increase in RoC and an associated increase in $\Delta\omega_{03}$ of a few hundred hertz to a steady state around 15.3 kHz. At this circulating power, the parametric gain was low enough and the transient fast enough such that the amplitude transient in the 15 kHz modes was small.

The sensitivity of the detector is fundamentally limited by shot noise at high frequencies, which depends on the power circulating in the interferometer. To reach Advanced LIGO design sensitivity, higher circulating power is required to reduce the shot noise. At the time of this experiment, the power had been increased to 170 kW circulating in the arm cavities. The increased power absorbed in the central region of a test mass increased the radius of curvature by approximately 10 m and increased $\Delta\omega_{03}$ several hundred Hz. An illustration

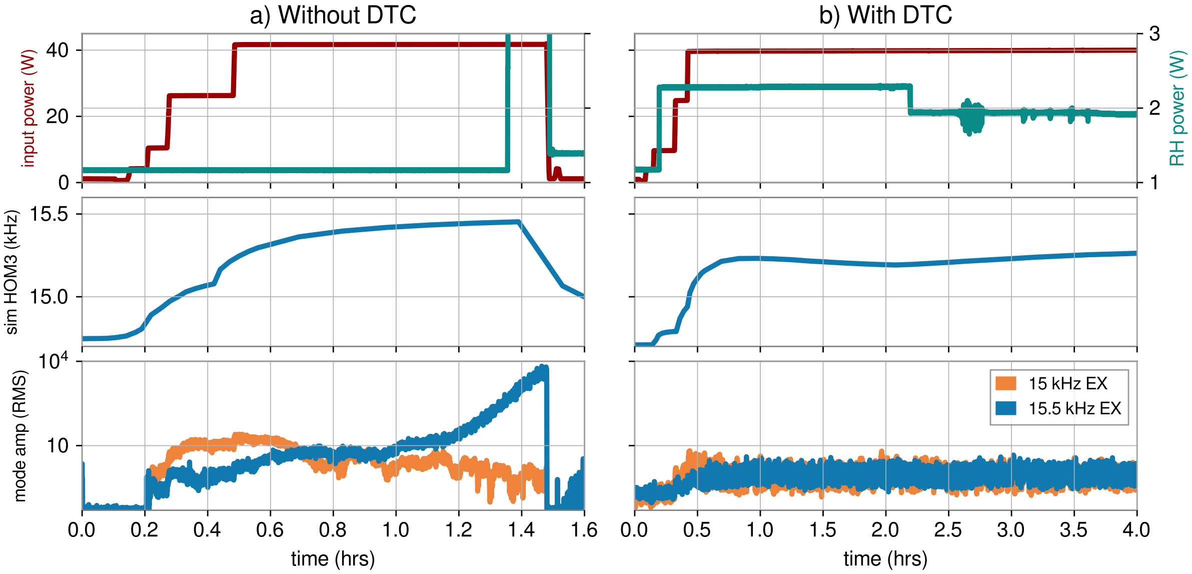

Figure 5.8. Simulation and experimental results from static and dynamic thermal compensation (DTC) at LIGO Livingston. The top panels show input laser power and ring heater (RH) power during lock acquisition and into the lock, the middle panels show the single cavity simulation of the HOM3 spacing, and the bottom panels show mechanical modes' RMS amplitude. Panel a) shows the results of a lock at 40 W input power without DTC: as the power is increased, the HOM3 spacing increases. As the optical beat note moves towards 15.5 kHz, the parametric gain of a 15.5 kHz mechanical mode grows and becomes unstable. The ring heater power was stepped up in a last attempt to save the lock, but the resultant optical shift was too slow and PI caused the interferometer to lose resonance. Panel b) demonstrates a successful 40 W lock using DTC: the end ring heaters are stepped up prior to input power-up to compensate the initial self heating transient. Two hours later, the ring heaters are stepped down to account for the different thermal transient shapes. Simulation shows the optical mode remaining in the safe zone between 15 kHz and 15.5 kHz and, indeed, mechanical modes remain stable throughout the duration of the lock.

of the opto-mechanical interaction is shown in Fig. 5.7, with the cyan curve showing the third order optical beat note peak in the cold arm cavity and the red lines showing locations of instability during the central heating thermal transient. The static ring heater power was increased in an attempt to avoid the 15.5 kHz modes, but the combination of higher parametric gain and a slower transient resulted in the 15 kHz modes becoming unstable for a period. There was no stable static ring heater setting. With more ring heater power, the 15 kHz modes became unstable at the beginning of lock, unlocking the interferometer. With less ring heater power, the 15.5 kHz modes became unstable, unlocking the interferometer about an hour into the lock; an example of this case is shown in Fig. 5.8a. This necessitated the use of dynamic thermal tuning.

Dynamic thermal tuning

As increased operating power causes the optical mode transient to sweep through larger frequency ranges, a static ring heater setting becomes insufficient for avoiding parametric instability. Dynamic thermal compensation (DTC) is needed to control the optical mode to within a frequency band of sub-unity parametric gain. We demonstrate a technique of applying power to the end test mass (ETM) ring heaters in multiple steps throughout the transient to compensate the central heating from the cavity beam while accounting for the different shapes of the ring heater and central heating RoC transients. DTC minimizes the change in cavity geometry; in the experiment presented here, $\Delta\omega_{03}$ is controlled to avoid the 15 and 15.5 kHz mechanical modes known to go unstable.

The ring heater and central heating have different RoC step responses, shown in Fig. 5.9. The RoC behavior due to the cavity power is asymptotic, reaching its approximate steady state value within the first hour. The ring heater transient has an initial overshoot as the heat first hits the outer edge, reaching the maximum RoC decrease around 2 hours, followed by a long, slightly increasing RoC transient as the heat is distributed throughout the test mass until steady state is reached about 12 hours after the power up. The ring heater has a

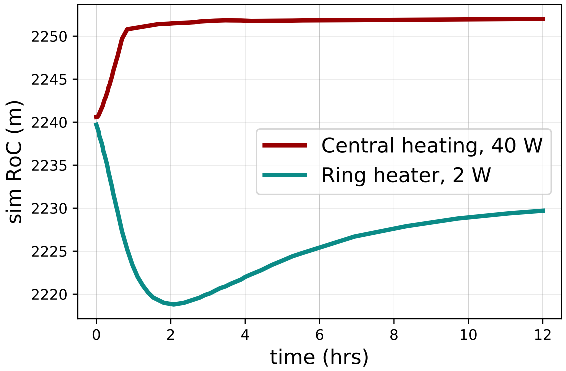

Figure 5.9. Single cavity simulation of ETM RoC transients due to 2 W ring heater power and central heating from 40 W input power. Input power has been scaled to approximate 170 kW circulating arm power.

15 min delay before a RoC response is observed; therefore it is changed 15 min prior to the power up event. It is stepped up to a power higher than required for steady state, to better compensate the faster self-heating transient during the beginning of the lock. Then the ring heater power is reduced about 2 hours after the power up event to steady state settings. The steady state ETM ring heater power is set to compensate an absorption of 0.5 ppm per test-mass.

A simulation was made of the optical mode frequency using the methodology described by Jaberian et al [50]. Using finite element modeling software (COMSOL [51]), the time dependence of the surface deformation of each test mass was obtained by applying thermal loads. Central heat loads were applied to both input and end test masses and annular heat loads simulating the ring heaters were applied only to the end test masses. The surface deformation was then fit to estimate the RoC transient of each test mass. The time-dependent optical beat note transient for the simple cavity case was calculated using Eq. 5.8, with (m + n) = 3, and the RoC transient. As in [50], this technique was verified with OSCAR (a Matlab based optical FFT code) [52] using the complete mirror maps. For this analysis, we consider only the transient optical beat note frequency between the fundamental mode and the third higher order mode (HOM3) which is responsible for the most problematic PI observed in Advanced LIGO.

Two cases were simulated: a 40 W input power (170 kW circulating power) lock without DTC and the same power lock with DTC. Without DTC, the static ring heater power used during O2 (1.2 W) was applied to the ETM, along with a central heating thermal load. For DTC, the ring heater power was increased from 1.2 W to 2.4 W 15 minutes before applying the central heating, followed by a decrease to 2 W after 2 hours. Simulation parameters are summarized in Table 5.1. Absorption values for each test mass were extracted from direct measurement of power dependent wavefront distortion with Hartmann wavefront sensors [31]. Accuracy of the ring heater simulation was checked against measurements taken at LIGO, where the ring heater power was stepped up and cavity scans using an auxiliary laser were performed to verify transient mode spacing behavior [53].

Table 5.1. The specification of Advanced LIGO LLO X-arm optics used for the single cavity simulation. Cavity length, input and end test mass (ITM, ETM) parameters, and ring heater (RH) powers are listed.

Features	LLO (X-arm)
Cavity Length (m)	4000
ITM RoC (m)	1937.9
ETM RoC (m)	2239.7
ITM-thickness × diameter (m)	0.20 × 0.34
ETM-thickness × diameter (m)	0.199 × 0.34
ITM coating absorption (ppm)	0.3
ETM coating absorption (ppm)	0.5
Beam spot size on ITM (m)	0.055
Beam spot size on ETM (m)	0.062
ITM RH power (W)	0
ETM RH power (W)	variable

Experimental verification of the modeled DTC scheme was carried out in the LIGO Livingston detector and was successfully used to suppress PI with 170 kW circulating power, as shown in Fig. 5.8b. Fifteen minutes before power up, the end test mass ring heaters were stepped up from 1.2 W to 2.4 W. The power up transient was fast enough to avoid instability in the 15 kHz mechanical modes. The ring heaters were stepped down two hours into lock, stabilizing the optical mode to a steady state between the 15 and 15.5 kHz modes; the green curves in Fig. 5.7 show the range of the optical mode maintained by DTC after the first hour of lock. DTC was successfully demonstrated over multiple 40 W locks up to 14 hours long.

The Advanced LIGO design calls for 750 kW circulating power in the arms. Assuming 0.5 ppm absorption per test mass, compensating the central heating transient to hold $\Delta\omega_{03}$ stable around 15.3 kHz would require approximately 16 W ring heater power per arm. The ring heaters can deliver up to 40.5 W per test mass [53] and compensation can be distributed between both the input and end test masses. This approach will require mechanical mode Q-factor reduction from passive dampers (see Sec. 5.6), without which the range of RoC over which 15 kHz and 15.5 kHz will be unstable will be much larger than the spacing between them, leaving no stable region.

Optical model extension

The model used to tune the DTC approximates the optical system as a single cavity rather than using Advanced LIGO's full core configuration: a Dual-Recycled Michelson interferometer with Fabry-Perot arms (DRFPMi). This simplifies the analysis by allowing direct calculation of the time-dependent optical beat-note spacing of a single arm cavity via Eq. 5.8. The approximation is efficient for simulating general opto-mechanical overlap behavior where a precision of ∼100 Hz is sufficient. As the unstable mechanical mode density increases, and for the higher precision application of three-mode interaction monitoring as a cavity control mechanism (see Sec. 5.5), a more complete model of parametric gain within the full coupled cavity system must be utilized.

It has been shown that the presence of the power- and signal-recycling cavities alter the resonant conditions for higher order modes in the interferometer and therefore the conditions for which a mechanical mode will produce a PI [54, 55]. When the full interferometer configuration is considered, the parametric gain response with respect to changes in RoC alters from a single broad peak to multiple narrower, taller peaks, as shown in Fig. 5.10.

Figure 5.10 is the result of a Finesse model [56] configured as described by Green

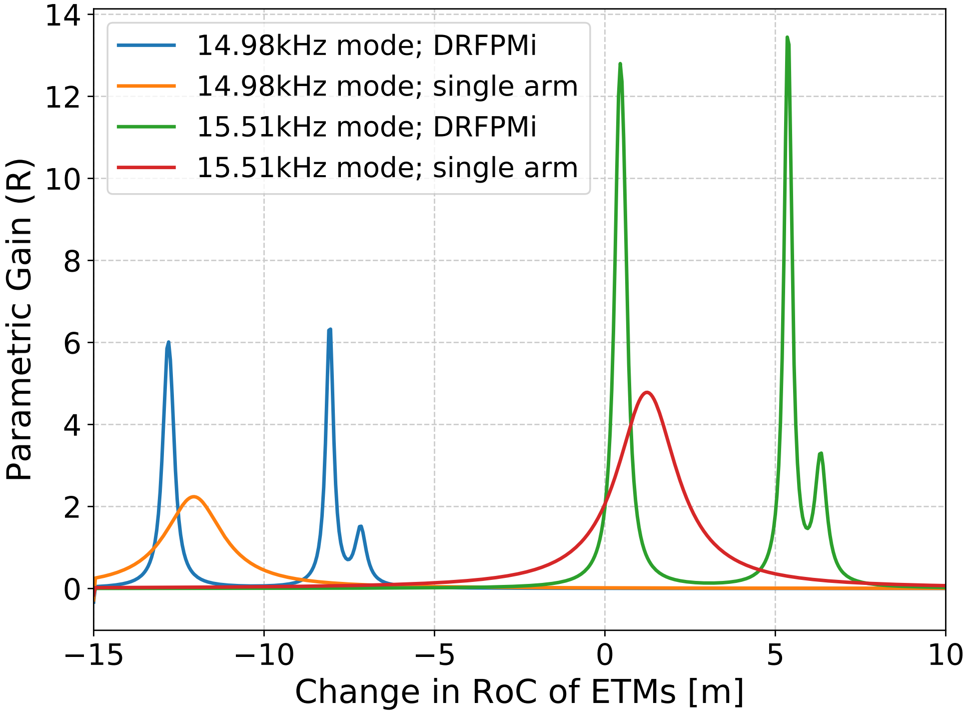

Figure 5.10. The parametric gain of the 15 kHz and 15.5 kHz mechanical modes as a function of ETMX and ETMY common radius of curvature change (from 2248 m). When the full DRFPMi is taken into account, the range of RoCs for which the interferometer is stable for both modes is split and reduced in width compared to the single arm model. In both configurations, input power is scaled to give 170 kW arm circulating power.

et. al. [55], with input power re-scaled to give an arm circulating power of 170 kW as was used in the experiment. In each case, a surface motion map, generated using a very simple Comsol model of the optic [57], is applied to ETMX at its eigenfrequency. The curvature of both ETMs in the Finesse model are then scanned simultaneously and the resulting parametric gain computed. This is done for both the full DRFPMi model and a reduced version which excludes all cavities except the X-arm, with input power re-scaled to compensate. Note that the surface motion map is generated for a flat optic, with all curvature introduced directly in the Finesse model.

When the recycling cavities are included, the range of RoC curvatures for which each of the 15 kHz and 15.5 kHz modes are stable becomes split, and spread over a wider range. While each individual unstable region is narrower than suggested by the single arm model, the stable regions are also expected to be narrower. The third order optical beat note changes by approximately 40 Hz per meter of RoC change. For a single arm, this gives approximately 400 Hz between instability maximums, but this is reduced to 300 Hz when considering the full interferometer.

This model represents a single snapshot in time of the interferometer state; in practice, the properties of the recycling cavities vary slightly from lock to lock and during the thermal transient. This could smear the effect of the recycling cavities when measuring R vs. RoC experimentally.

5.5 Three mode interaction monitoring

Determination of real-time optical mode frequency spacing currently relies on simulation. Hartmann wavefront sensors [31] monitor changes in wavefront distortion of a beam transmitted through the optic. The RoC of an optic can be inferred by assuming a thermal model; typically such models assume that laser power is absorbed uniformly in the mirror coating. Auxiliary laser systems can be also used to measure the transverse mode spacing of a cavity when the detector is not operating [53]. These techniques have been used to estimate rates of geometry change, such as to calibrate the effect of the ring heater. However, the cavity geometry during high power operation is affected by other things, such as thermal expansion from nonuniform absorption in the coatings [58], and by the beam position on the test mass [59] in conjunction with figure error in the mirror surface.

Each test mass mechanical mode amplitude in the gravitational-wave readout channel is the result of the spatial overlap between the mechanical mode of the optic and one or more transverse optical cavity modes. The signal is enhanced if the light scattered from the mechanical mode is resonant in the cavity, i.e. maximising Eq. 5.7. When the opto-mechanical coupling is high enough, the three-mode interaction – mechanical mode, the fundamental optical mode, and a higher order optical mode – results in a real change in mechanical mode amplitude. As these interactions depend strongly on the optical beat note frequency, they act as a highly sensitive witness of cavity geometry. Monitoring the mechanical mode amplitude has therefore been suggested as a tool to monitor cavity geometry [60]. The experiment reported here provides a demonstration of a three mode interaction monitoring (3MIM) technique for the full operating LIGO interferometer. In this case limits are inferred on the allowed cavity geometry consistent with a parametrically stable model.

Parametric instability has been used to tune the dynamic thermal compensation and thus maintain the cavity geometry between the two unstable thermal tuning regimes (around 15 and 15.5 kHz). The maximum parametric gain was estimated to be 3 for the 15 kHz mode and 7 for the 15.5 kHz mode [61] with 100 kW intra-cavity. Assuming a 89 Hz transverse mode linewidth, there is a stable regime between optical beat note frequencies 15060 Hz and 15390 Hz at 170 kW. Using Eq. 6.4, this shows that the cavity g-factor product has been maintained to within $g_1 g_2 = 0.829 \pm 0.004$ after an initial thermal transient of approximately one hour, where $g_n = 1 - (L/R_n)$. The simulated range of beat note frequencies shown in green in Fig. 5.7 are considerably narrower than this range. This analysis assumes a single-cavity model approximation; we will see in the next section that a full interferometer model reduces the g-factor range between unstable regimes. Therefore, this estimate provides an upper limit on g-factor stability range.

In addition to avoiding PI, maintaining the cavity geometry reduces the change in cavity beam parameters and stabilizes mode matching to the input and output of the interferometer. This will be necessary to achieve the ambitious loss requirements of Advanced LIGO and A+. In principle, a much higher precision g-factor measurement could be made from the opto-mechanical interaction strength; however, this is conditional on having a good understanding of the resonant optical modes discussed in Sec. 5.4 and a reliable measurement of the interaction strength.

5.6 Acoustic mode dampers

This section presents a fundamental approach to eliminating PI by reducing the test mass mechanical modes with acoustic mode dampers (AMDs), decreasing the parametric gain to stable regimes. After a successful test on a single test mass at LLO, AMDs were installed on all test masses at both sites prior to O3 and have eliminated almost all PI at 270 kW arm power. They are projected to mitigate all but a few modes (which can then be addressed with one of the previously discussed techniques) up through aLIGO design circulating power. AMDs were designed and built by Biscans et al. at MIT; the author led the post-installation analysis presented in Sec. 5.6.2. Results are presented in [46].

As passive dampers require direct contact with the optic, the challenge is to dissipate mechanical energy in the 10-80 kHz band while not significantly increasing the thermal noise around 100 Hz, where LIGO's strain sensitivity is closest to limitation by coating thermal noise. Gras *et al.* investigated several damping techniques, including metal rings and coatings, and prototype acoustic mode dampers; while each iteration showed increasing success at damping mechanical modes, all increased thermal noise above practical design limits [54,62]. The design presented in [62] was reworked, with a focus on reducing noise at each stage, and the resultant AMDs were tested and installed on all LIGO test masses.

5.6.1 AMD design

The AMDs are piezoelectric tuned mass dampers installed directly on the barrel of the test mass. The design concept is shown in Fig. 5.11. The AMDs consist of a base that attaches to the optic, a piezoelectric plate shunted with a resistor, and a reaction mass. The piezoelectric plate converts mechanical energy into electrical energy which is then dissipated through the resistor and released as heat. The PZT and the reaction mass determine the principal resonance of the AMD. If we model the system in one dimension, the spring constant $k_{pzt,sh}$ of the shunted PZT is a function of the angular frequency $\omega = 2\pi f$:

$$k_{pzt,sh}(\omega) = Y[1 + i\eta_r(\omega)]\frac{S}{h}\,, \tag{5.10}$$

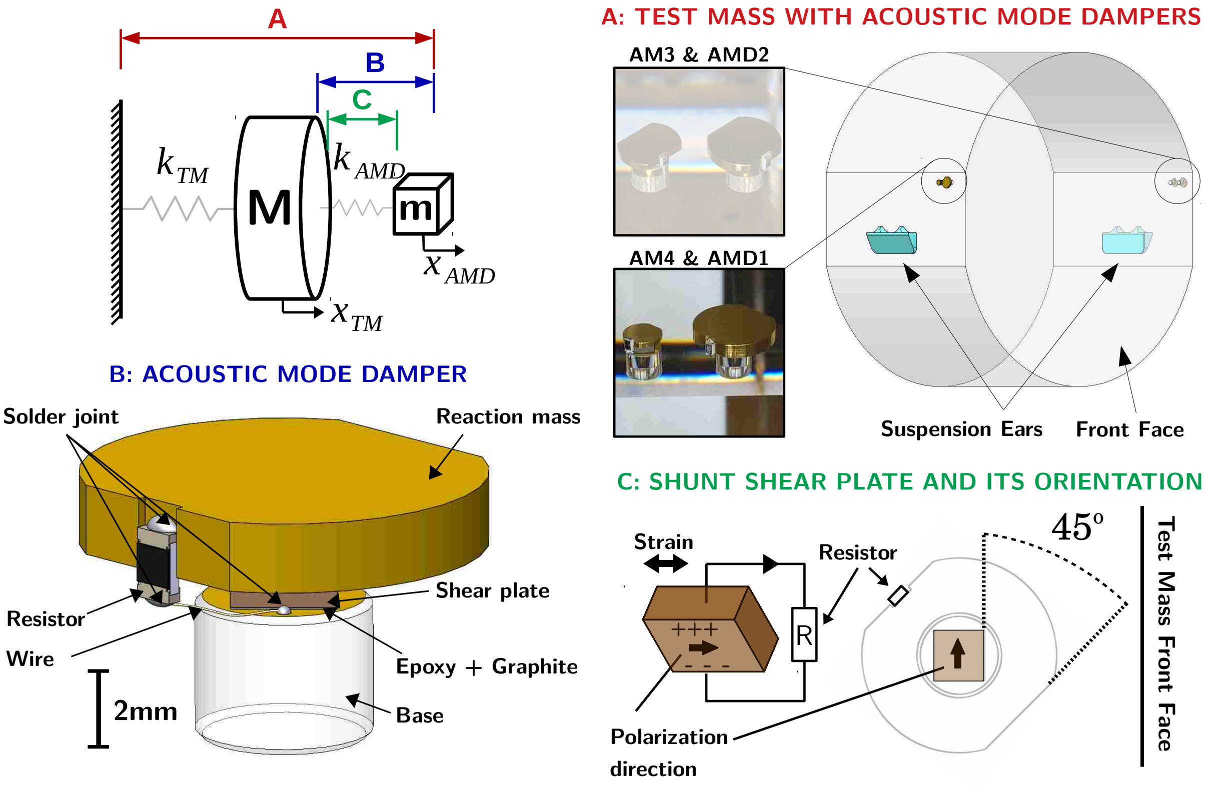

Figure 5.11. Overview of the low-noise Acoustic Mode Damper. The AMD can be described as a small damper of mass m attached to a larger vibrating mass M, as illustrated in the top left. To cover a broader frequency bandwidth, each test mass is equipped with four different AMDs distributed on the optic's flats, as shown in Fig. A. Each AMD is made of a base, a shunted shear plate and a reaction mass (Fig. B). The shunted shear plate is used as a lossy tunable spring with a complex stiffness k_{AMD}. Its polarization direction is oriented perpendicular to the cavity axis to limit thermal noise injection (Fig. C). Finally, the top face of the base and the entire reaction mass are gold coated for electrical conductivity, assuring current flow between the PZT plate and the resistor. The bonds with the PZT plate are made of epoxy mixed with graphite nano-particles for conductivity.

where Y is the Young's modulus of the PZT material (bulk or shear), S is the surface area, h the height of the plate. The loss due to the resistor is

$$\eta_r(\omega) = \frac{RC\omega k^2}{(1-k^2) + (RC\omega)^2}, \tag{5.11}$$

where R is the shunt resistance and C the capacitance of the PZT plate [63]. The square of the electromechanical coupling coefficient k (set by the material of the PZT) represents the percentage of mechanical strain energy which is converted into electrical energy [64]. The resistor is tuned such that the peak loss occurs where unstable mechanical modes exist.

The reaction mass m attached to the PZT spring creates the AMD oscillator, with resonant frequency f_D. When attached to a TM of mass M, the AMD-TM system becomes a coupled oscillator with resonant frequency f_m and a resultant mechanical mode Q-factor

$$Q_m \simeq \frac{\eta_r^2 + (1-\rho)^2}{\eta_r \mu \rho}\,, \tag{5.12}$$

where $\rho = f_m/f_D$, and the mass ratio, $\mu = m/M$, is assumed to be small [62]. When the TM and AMD resonance are similar, $\eta_r \gg |1-\rho|$ and $Q_m \simeq \eta_r/\mu$. With $\eta_r = 0.1$ and $M = 10\,\mathrm{kg}$, a reaction mass of 1–10 mg is required for a Q-factor reduction of one to two orders of magnitude.

The simple model discussed above neglects material losses, losses arising from bonding the AMD to the TM, imperfect placement of the AMD on the TM antinode, and multiple coupled degrees of freedom in the AMD. The design elements discussed below maximize damping of problematic mechanical mode frequencies while reducing loss in the DARM strain band.

A single, large mass passive damper that covers the full 10-80 kHz damping band also introduces more thermal noise than a smaller mass; a larger mass will create more inertia against a TM-driven acceleration and a larger strain on lossy components of the damper. Thus, the reaction masses are kept small (<1 g) and the damping for a single TM is split into 4 differently tuned AMDs, each tuned to cover a more narrow frequency band. The reaction masses are also asymmetric, splitting the degeneracy of the principal resonance into five, each of which can be tuned to a specific band; see Fig. 5.12.

The geometry of the AMDs can further reduce unwanted loss. TM motion will generally

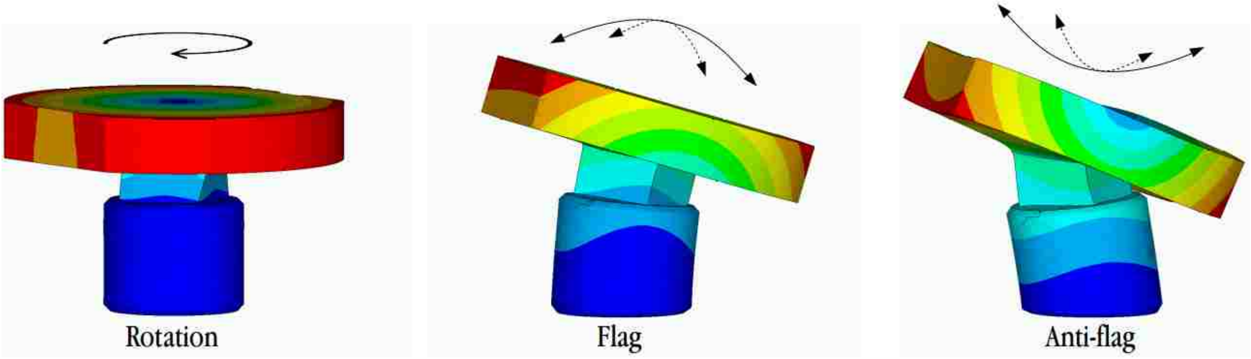

Figure 5.12. A visualization of the three principal resonances of an AMD, the latter two of which are further split into doublets.

accelerate in all directions, while thermal noise pertains mostly to motion in the optical axis direction. By using a shear plate PZT and mounting the AMDs such the PZT's active direction is perpendicular to the optical axis, the mechanical mode loss coupling is relatively maximized.

5.6.2 Testing and results

Prior to O3, a test of the AMDs was performed at LLO and, upon its success, AMDs were installed on all test masses at both LIGO sites. No parametric instabilities are observed in the (15-80)kHz range - even without any thermal mode tuning or active damping - with an arm power level of $P_{arm} = 230\,\mathrm{kW}$, in contrast to without AMDs, when the first instability would appear at 25 kW arm power.

To quantitatively assess AMD performance, we measured Q-factor reduction of mechanical modes, parametric gain of a specific mode versus cavity tuning, and classical noise in the thermal noise impact region.

Prior to full installation, a test of AMDs on a single optic was performed at LLO. As the ETMs were being replaced, four test AMDs were installed on the old optic, providing a test of the installation procedure and results at no risk.

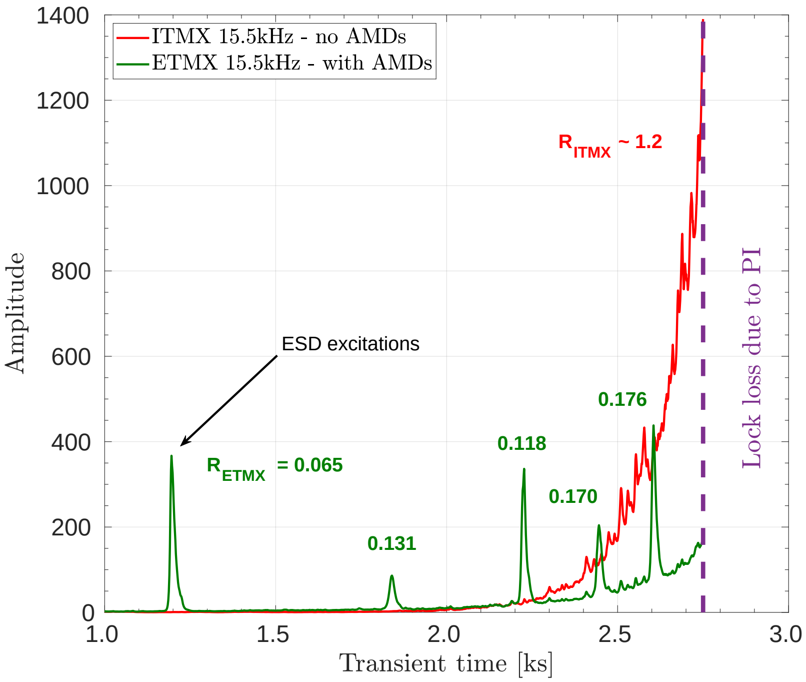

Figure 5.13. Thermal transient of the 15.5kHz modes on input (ITMX) and end (ETMX) TMs, respectively. As expected, the ITMX without AMDs became unstable during thermal transient, with rapidly rising amplitude. Contrary, ETMX which has attached AMDs remains stable with parametric gain below unity. The rising envelope of the ETMX signal is a result of imperfect filtering out of the ITMX signal.

Optical mode transient test

As discussed in 5.3, thermal tuning of a TM's RoC will shift a cavity HOM and change the gain of the mode G_n. By tuning an optical mode to move through the frequency band of the PI-relevant mechanical modes, we can sweep through the maximum parametric gain and estimate the safety factor before instability would occur.

We performed this measurement during the ETMX AMD test period. The interferometer was locked with 100 kW circulating power and the ETMX RH was turned off, such that HOM3 swept up in frequency towards 15.5 kHz. The parametric gain of the ITMX and ETMX 15.5 kHz mechanical modes were monitored so that we could compare the test masses without and with AMDs. As the respective 15.5 kHz mechanical modes of each test mass differ by about 4 Hz, the optical gain for both is expected to be similar. We periodically excited the ETMX mode using the ESD method discussed in 5.2 and measured the ring-down time, from which the parametric gain was extracted using Eq. 5.3. The ITMX mode was free to continually grow.

The evolution of the 15.5 kHz mode amplitude in both TMs is shown in Fig. 5.13. ITMX, which does not have AMDs, becomes unstable with a measured parametric gain of $R = 1.2$ before it drives the interferometer out of lock. ETMX, with AMDs, remains stable with a highest measured gain of $R < 0.2$. The ITMX instability causes lockloss before moving through maximum parametric gain. However, if we fit the measured ETMX gain values to a Lorentzian, we estimate the ITMX 15.5 kHz mode to have a max parametric gain of 1.6. If we assume the same factor increase for the ETMX mode, the 15.5 kHz mode with the AMD installed has a max gain of 0.2, indicating a reduction over an order of magnitude (pre-AMD max gain estimated to be 7). This is in line with the reduction of the Q-factor measured for this mode.

Additionally, since the 15.5 kHz mode is the strongest in terms of parametric instabilities, this R value can be used to estimate the maximum arm power at which the interferometers should be stable under most thermal tuning conditions: $P_{max} = 100\,\mathrm{kW}/0.2 = 500\,\mathrm{kW}$. Furthermore, any instabilities that occur when the full design power of 750 kW is reached should be avoidable with thermal cavity tuning.

Test mass Q-factors

Finite element analysis (FEA) models were made to estimate the Q-factors of the test mass mechanical modes with AMDs. Monte Carlo methods are then used to determine the resultant maximum parametric gain of each mode. To test AMD effectiveness, we measured Q-factors before and after AMD installation.

The ESD actuation method discussed in Sec. 5.2 was used to excite the TM mechanical modes and their Q-factors are extracted from the ring down resulted in the high rate gravitational wave channel. Measurements are taken at 2 W input laser power to mostly avoid the effect of parametric gain on the ring down times.

We successfully measured Q-factors for thirteen modes post-AMD installation, across multiple test masses, in the band $(10 - 50)\,\mathrm{kHz}$ [65]. For the ten lowest frequency modes, we could identify their particular mode shapes and so can compare the measurements to the finite element model predictions; above 30 kHz the mode density is so high that it is not possible to map the frequency to a particular mode shape. The Q-factor measurements from the LIGO Livingston interferometer are shown in Fig. 5.14; the results from LHO are similar. The plot also includes ten Q-factors from one of the LLO TMs measured before the AMDs were installed. As predicted by modeling, the Q-factors for all but one of the modes at 15 kHz and above are reduced by nearly an order of magnitude or more.

The variations in Q across TMs and the deviations from the modelled values are realistic given uncertainty bounds of AMD and TM parameters. There is error on the FEA prediction of TM mechanical mode frequencies around 0.5%, or up to a few hundred Hz; as the AMDs were designed to maximize overlap with these modeled TM frequencies, the actual overlap may vary. The location of installed AMDs could vary by several mm, which could vary the AMD coupling test mass to test mass. Additionally, the epoxy bond thickness could vary by up to -50% or +20% from the $1\,\mu$m nominal thickness, which would limit the accuracy of the AMD principal resonance to about 5 kHz.

A table-style list of all measured Q-factors is shown in Fig. 5.15

Thermal noise impact

The AMDs were modeled to add at most an additional 1.2% strain noise at 60 Hz due to thermal noise increase. An increase in thermal noise would first be seen around 100 Hz in the DARM strain spectrum where the thermal noise sits closest, as seen in Fig. 5.16. Above 40 Hz, however, DARM is limited by quantum shot noise. The classical noise - including thermal noise - spectrum beneath the quantum noise can be revealed with cross correlation, described in Sec. 2.5.3. As the thermal noise cannot be isolated, it is not possible to quantify

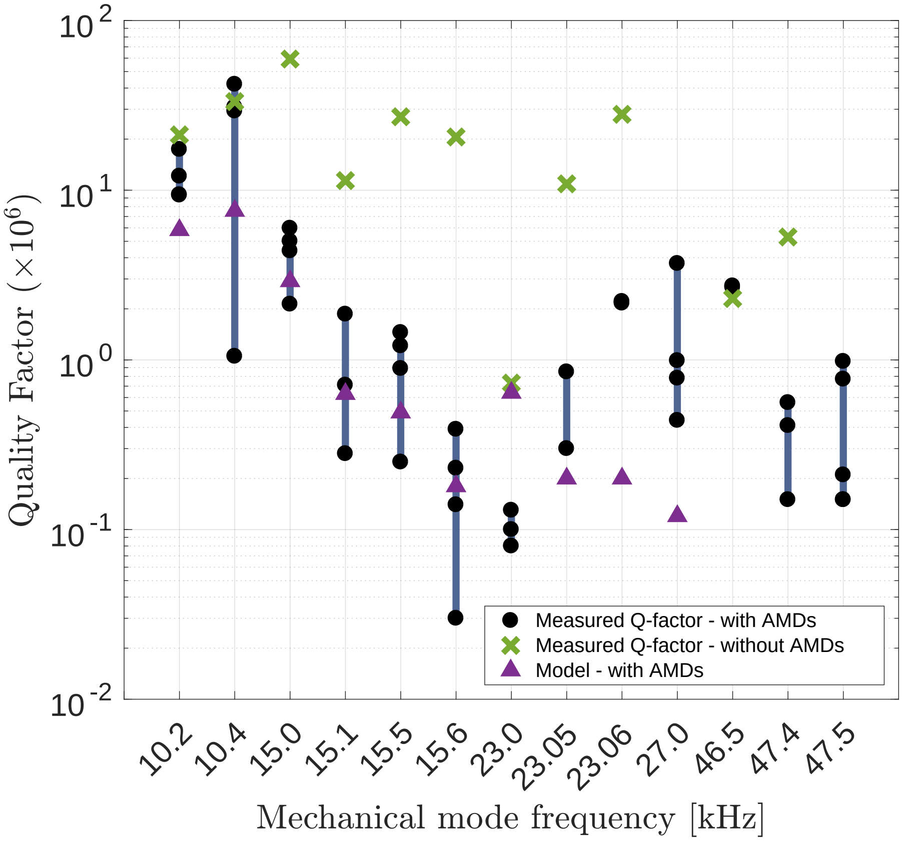

Figure 5.14. Measured Q-factors of TM mechanical modes. The green crosses correspond to pre-AMD measurements of one of the LLO TMs. The post-AMD Q-factors are shown as black dots. The blue bars indicate the spread of Qs measured across several TMs (with AMDs), and the purple triangles represent the model prediction of Qs with AMDs [66]

the thermal noise impact from AMDs. Rather, by comparing the classical noise before and after installation and to noise model expectation, we set an upper limit on the noise impact.

The cross correlated spectrum was analyzed before and after full AMD installation at LLO. Data was taken during low-noise operations. Between measurements, several changes were made to the detector in addition to the installation of the AMDs, including annular reaction masses and scattered light baffle installation. Thus, the comparison does not measure only the change due to AMDs. However, it can be used to verify that the classical noise did not increase with the presence of AMDs. In addition, we can compare the measured cross-spectrum with the modeled classical noises, which are well-known in the frequency band of interest.

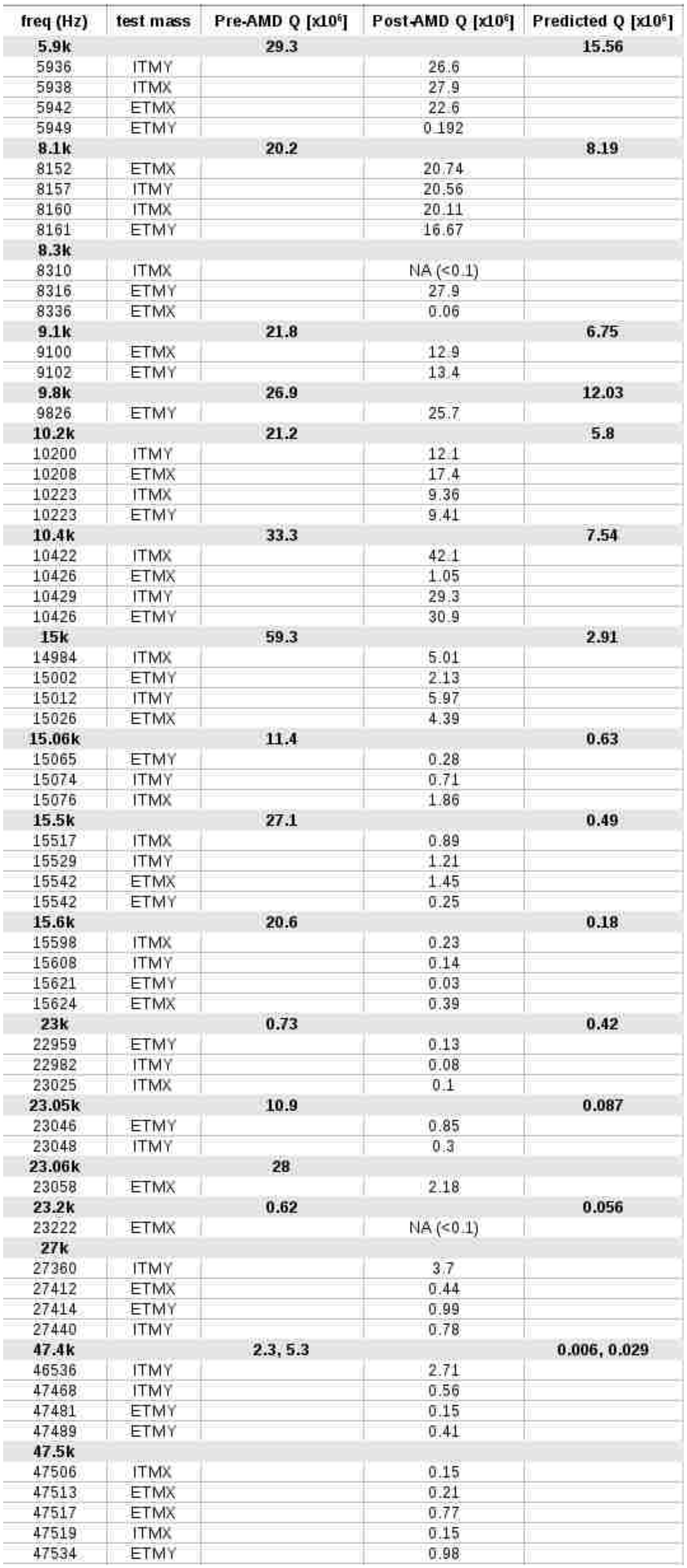

freq (Hz)	test mass	Pre-AMD Q [x10^6]	Post-AMD Q [x10^6]	Predicted Q [x10^6]
5.9k		**29.3**		**15.56**
5936	ITMY		26.6	
5938	ITMX		27.9	
5942	ETMX		22.6	
5949	ETMY		0.192	
8.1k		**20.2**		**8.19**
8152	ETMX		20.74	
8157	ITMY		20.56	
8160	ITMX		20.11	
8161	ETMY		16.67	
8.3k				
8310	ITMX		NA (<0.1)	
8316	ETMY		27.9	
8336	ETMX		0.06	
9.1k		**21.8**		**6.75**
9100	ETMX		12.9	
9102	ETMY		13.4	
9.8k		**26.9**		**12.03**
9826	ETMY		25.7	
10.2k		**21.2**		**5.8**
10200	ITMY		12.1	
10208	ETMX		17.4	
10223	ITMX		9.36	
10223	ETMY		9.41	
10.4k		**33.3**		**7.54**
10422	ITMX		42.1	
10426	ETMX		1.05	
10429	ITMY		29.3	
10426	ETMY		30.9	
15k		**59.3**		**2.91**
14984	ITMX		5.01	
15002	ETMY		2.13	
15012	ITMY		5.97	
15026	ETMX		4.39	
15.06k		**11.4**		**0.63**
15065	ETMY		0.28	
15074	ITMY		0.71	
15076	ITMX		1.86	
15.5k		**27.1**		**0.49**
15517	ITMX		0.89	
15529	ITMY		1.21	
15542	ETMX		1.45	
15542	ETMY		0.25	
15.6k		**20.6**		**0.18**
15598	ITMX		0.23	
15608	ITMY		0.14	
15621	ETMY		0.03	
15624	ETMX		0.39	
23k		**0.73**		**0.42**
22959	ETMY		0.13	
22982	ITMY		0.08	
23025	ITMX		0.1	
23.05k		**10.9**		**0.087**
23046	ETMY		0.85	
23048	ITMY		0.3	
23.06k		**28**		
23058	ETMX		2.18	
23.2k		**0.62**		**0.056**
23222	ETMX		NA (<0.1)	
27k				
27360	ITMY		3.7	
27412	ETMX		0.44	
27414	ETMY		0.99	
27440	ITMY		0.78	
47.4k		**2.3, 5.3**		**0.006, 0.029**
46536	ITMY		2.71	
47468	ITMY		0.56	
47481	ETMY		0.15	
47489	ETMY		0.41	
47.5k				
47506	ITMX		0.15	
47513	ETMX		0.21	
47517	ETMX		0.77	
47519	ITMX		0.15	
47534	ETMY		0.98	

Figure 5.15. All measured Q-factors of TM mechanical modes, before and after AMD installation on all test masses. Pre-AMD Qs are from ETMX. Last column shows Qs predicted by model.

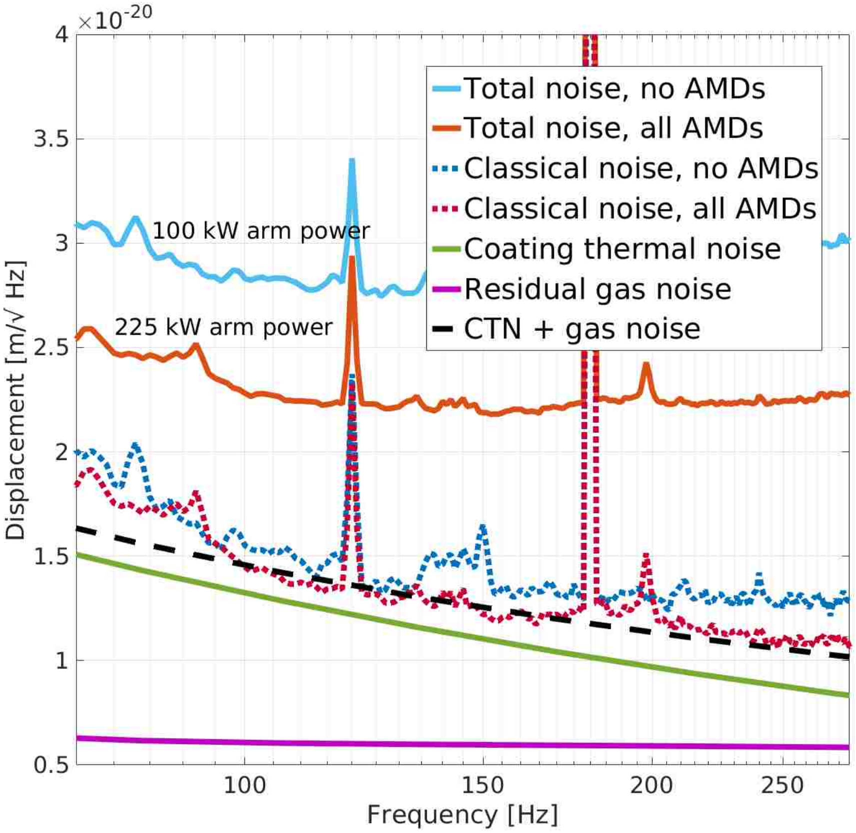

Figure 5.16. Noise spectra of the Livingston interferometer before and after installation of all AMD. The solid lines show the total noise level measured (classical + quantum noise). The dotted show the level of classical noise only, after the quantum has been subtracted via a cross-correlation technique. Coating thermal noise and residual gas noise - the dominant classical noise contributions in this region - are also shown.

Total interferometer noise and cross spectrum classical noise both before and after AMDs were installed on all test masses is shown in Fig. 5.16. The total noise decrease with AMDs is due to increased circulating power, which reduces the shot noise. The small decrease in classical noise after AMD installation is likely due to an unrelated reduction in a different classical noise, such as scattered light. The classical noise model is shown in dotted black, along with two dominant classical components that contribute: coating thermal noise and phase noise due to residual gas in the beam tubes. We see that the measured classical noise with AMDs (dashed red curve) matches the noise model estimate for the dominant classical noises well in most of the 50 - 300 Hz frequency band. The discrepancy between the AMD measurement 100-150Hz and the model is within the $\sim 2\%$ detector calibration uncertainty [67] and model uncertainties which are larger than calibration uncertainty. There is no evidence that the AMDs are introducing significant additional thermal noise.

Effect of beam decentering

The simulations of opto-mechanical overlap used to asses AMD effectiveness on PI gain assume the cavity beam is centered on the test mass. In practice, the beam may be purposefully decentered to avoid point absorbers; the beam location is walked to optimize cavity build up and interferometer sensitivity, which can result in the beam sitting up to tens of mm off center of several test masses at both sites. This significantly alters the geometrical overlap $B_{m,n}$ from that modeled and can increase (or decrease) the probability of PI. This is particularly the case for a pair of acoustic modes at 10.2 and 10.4 kHz, which have a displacement pattern on the test mass face similar to the Zernike trefoil polynomial. These modes overlap only weakly with the Hermite-Gaussian second order modes ($HG_{0,2}, HG_{2,0}$ and $HG_{1,1}$) when the cavity beam is centered, but the overlap factor can increase by several orders of magnitude when the beam is off-center. Instabilities at both 10.2 and 10.4 kHz have been observed in one of the LHO arm cavities with 230 kW circulating power. At this power, both instabilities are stabilized by shifting the second-order optical modes by $\sim$100 Hz using the ring heater on the end test mass.

6 Cavity mode content with thermal aberrations

In Sec. 4.3.2, we saw that a non-uniform test mass surface can cause scatter into higher order spacial modes of the arm cavity. In this chapter we further explore this relationship, in particular how higher order mode fields can give us information about the optic surface and how higher order mode content can likewise be manipulated via thermal actuation.

The work in this chapter was carried out at Caltech's 40 m interferometer by the author alongside A. Allocca and with significant contribution from the 40 m commissioners. A detailed background can be found in her thesis [37] and previous experimental results on the subject are presented in [68]. This work is ongoing and preliminary results are presented.

6.1 Mirror distortions and field response

The resonant frequency of a field in an optical cavity is determined by the radius of curvature of the cavity optics. Usually, we approximate an optic surface as spherical, with a radius of curvature that changes with high circulating power and that might be actuated with ring heaters as discussed in Chpt. 4. In reality, mirror surface errors create local deviations that disrupt the spherical shape and result in local radius of curvature variations. To understand field interactions with these surface variations, it is useful to decompose mirror maps into a sum of Zernike polynomials, which represent a complete orthogonal basis over the unit circle. Zernike polynomials are described by radial and azimuthal indices; the first few orders of Zernike polynomials are shown in Fig.6.1. The mirror map can then be written as

$$Z(x,y) = \sum_{i,j} c_{i,j} \mathcal{Z}_i^j(x,y). \tag{6.1}$$

If we consider a field $\psi_0(x,y)$ incident on a distorted mirror with reflectivity r and where $Z(x,y)$ is the surface deviation map, then the reflected field will carry information about that surface map:

$$\psi_R(x,y) = re^{2ikZ(x,y)}\psi_0(x,y). \tag{6.2}$$

As we are interested in the effect in terms of higher order modes, we follow the represen-

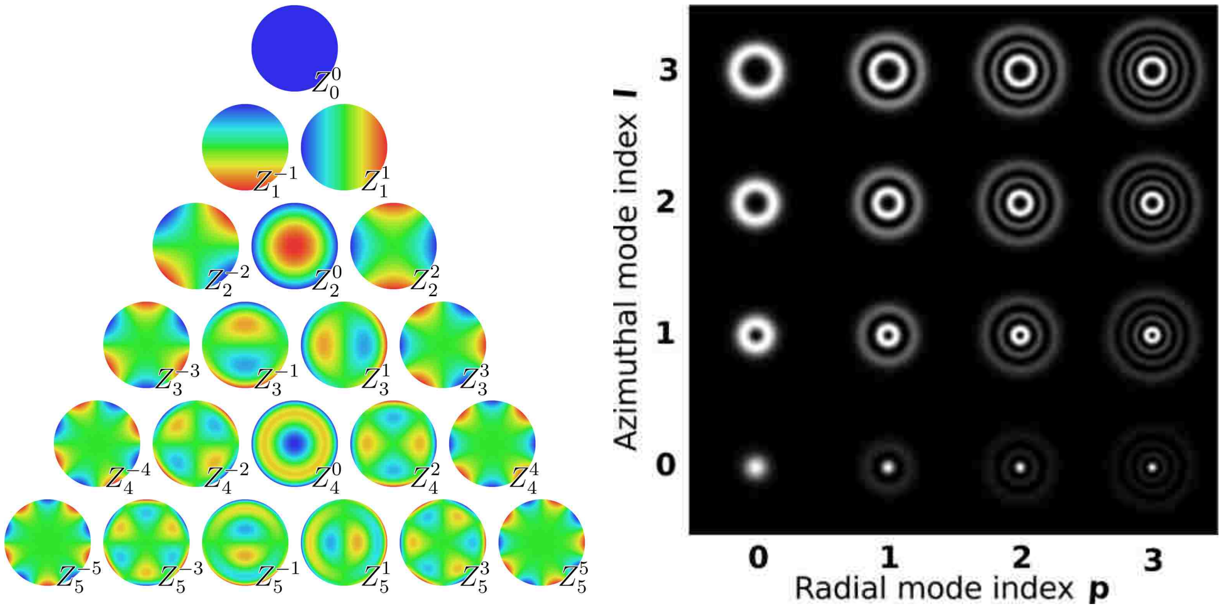

Figure 6.1. Left: The first 21 Zernike polynomials, ordered vertically by radial degree and horizontally by azimuthal degree. Zernike image from [69]. Right: The first few orders of Laguerre-Gauss (LG) optical mode. Image from [70]

tation developed in [37] where the mirror is an operator that acts on the the fundamental Gaussian mode in the cavity as a coupling mechanism to higher order mode (nm):

$$M_{nm,00} = r < nm|e^{-2ikZ(x,y)}|00 > . \tag{6.3}$$

As higher order modes have different spacial distributions - Laguerre-Gauss basis shown in Fig. 6.1 - each interacts with the mirror surface uniquely, experiencing a particular radius of curvature that depends on the mirror figure of error averaged over that mode's spacial extent. In this way, mirror distortions away from uniform radius of curvature can change the resonance conditions for different modes, shifting their resonance frequency away from the ideal frequency.

In this experiment, we use projected heat patterns to create known mirror distortions and measure the corresponding field response, as illustrated in Fig. 6.2. We introduce non-uniform radius of curvature changes with the aim to measure unique shifts in frequency of higher order optical modes which 'witness' the deformations more than others.

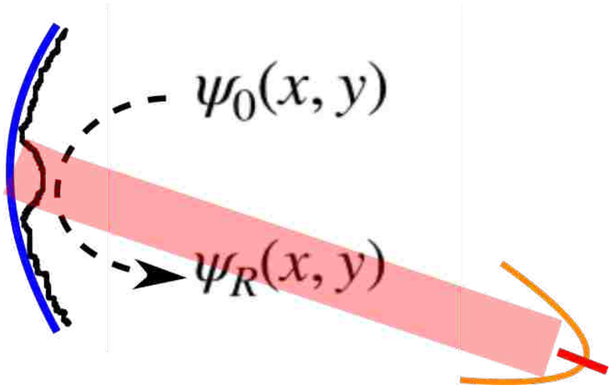

Figure 6.2. Illustration of projected heat pattern (red) causing a local mirror deformation (black) away from the ideal spherical optic surface (blue). The field reflected off of the deformed mirror carries information of the mirror surface map.

6.2 Experimental setup

Table 6.1. 40 m Y-arm measured cavity parameters

cold cavity parameter	value
cavity length (L)	37.78 m
aux wavelength (λ)	1064 nm
RoC ITMY (r_1)	∞
RoC ETMY (r_2)	60.65 m
free spectral range (FSR)	3.967 MHz
gouy phase	52°

In this experiment, heating patterns are projected onto the HR surface of the Y-end test mass in Caltech's 40 m interferometer. In a cavity of length L where $r_1 = \infty$, the transverse mode spacing $\Delta f_{pq} = |f_{00} - f_{pq}|$ between the higher order modes modes HOM_{00} and HOM_{pq} modes is

$$\Delta f_{pq} = (p+q)\frac{c}{2\pi L}\cos^{-1}\sqrt{\left(1 - \frac{L}{r_2}\right)}. \tag{6.4}$$

Using the parameters of the 40 m cold cavity listed in Table 6.1, this gives transverse mode spacing of approximately (p+q)1.15 MHz.

To measure transverse mode spacing, we used in-situ mode spectroscopy. Scans of the Y-arm cavity were taken using an auxiliary probe laser injected through the dark port. To stabilize the cavity length and the laser frequency, the cavity is locked to the PSL laser like

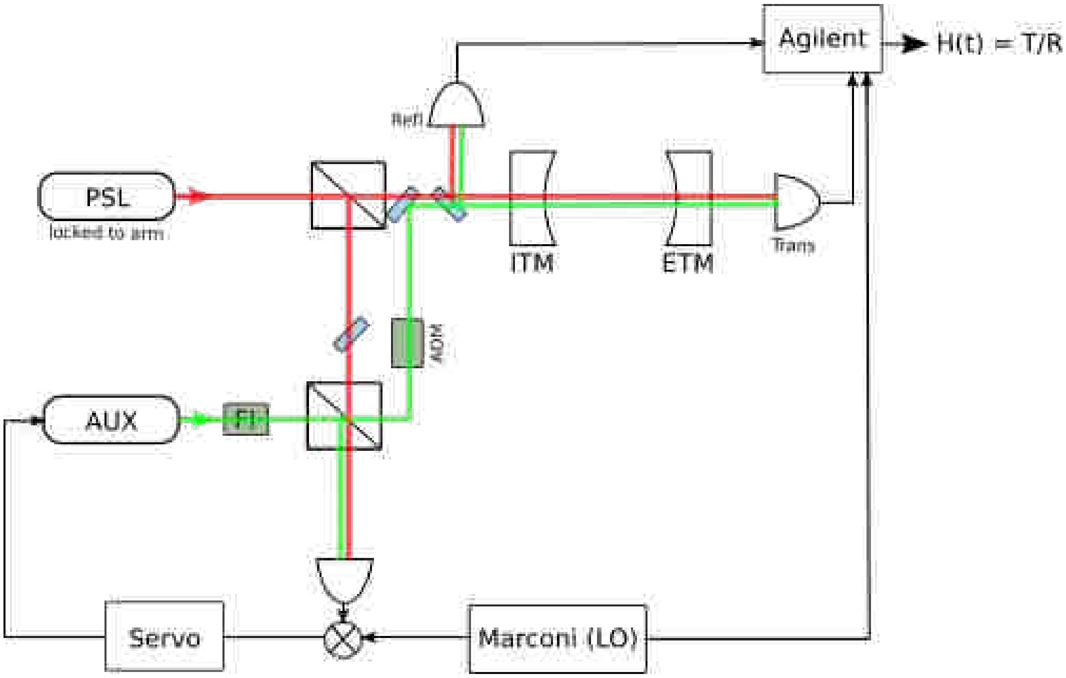

Figure 6.3. The optical topology of the experimental setup.

normal operation. The aux laser is then phase-locked to the PSL. It is important to note that the auxilary laser does not disturb the output of the interferometer, so this technique could be used in aLIGO detectors. The cavity scans are made by directly sweeping the aux laser frequency through a piezo, by introducing an offset in the local oscillator of the PLL between the aux and the input laser. The transmission/reflection transfer function is read out via a spectrum analyzer (Agilent). In order to get rid of the free running noise between Marconi and Agilent, the Marconi frequency was scanned and, point by point, the Agilent center frequency was changed accordingly. Phase data was cleanest by setting the Agilent bandwidth to 1 kHz. In order to speed up the process, the whole process was automated.

The input and output of the aux beam were intentionally clipped with razor blades to induce and better witness higher order mode content. Scans were taken over a full free spectral range and around each peak for higher resolution. A full free spectral range scan trans/refl transfer function bode plot before and after clipping is shown in Fig. 6.4. The first five higher order modes are clearly visible (HOM4 and HOM5 are wrapped).

Two heating set-ups were installed and tested, which we refer to as the cylinder and

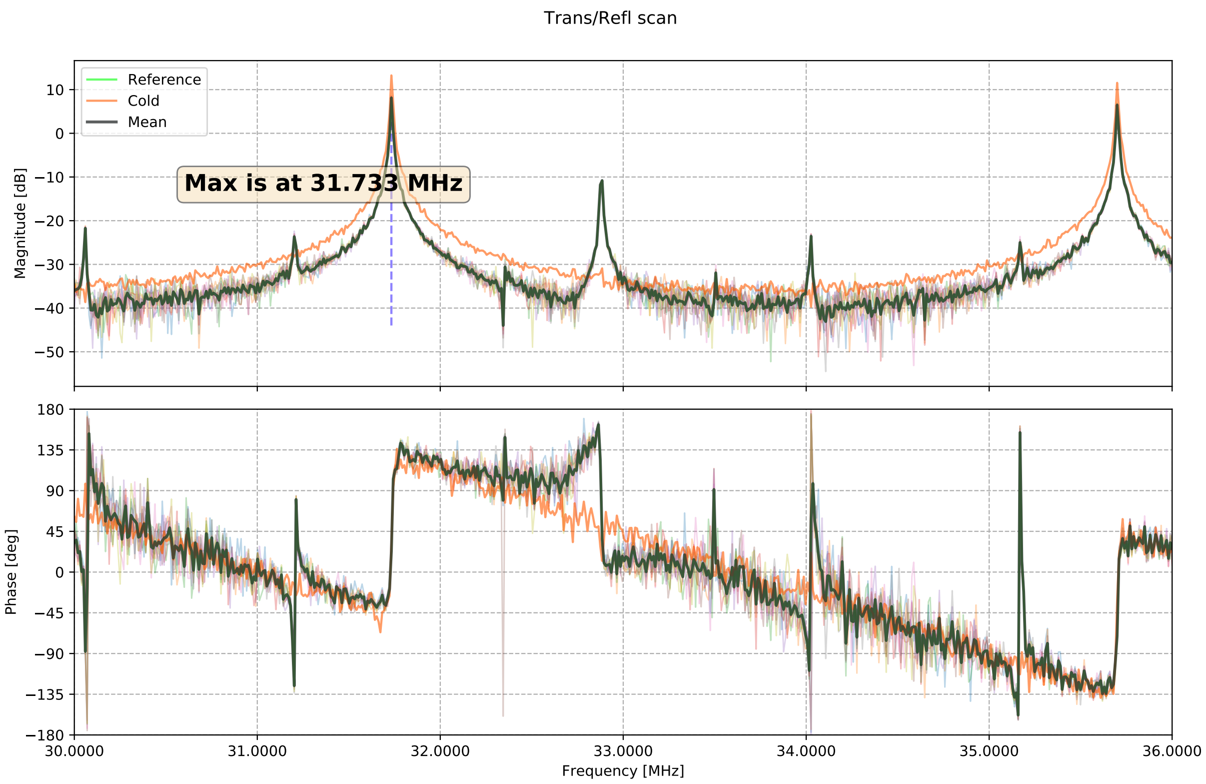

Figure 6.4. Bode plot of a full scan of a free spectral range of the Y-arm cavity, before (orange) and after (black) clipping the input and output beams. Each scan is a collective average of 10 consecutive measurements at each point of the scan. In the clipped scan, the carrier and 5 higher order modes are seen.

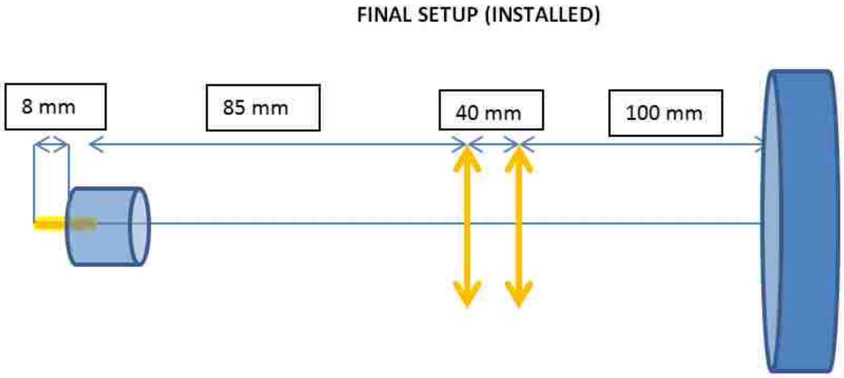

Figure 6.5. Cylinder heating set up. The final installed setup varied from modeled set-up due to spatial restraints in chamber, resulting in imperfect focus at the plane of the ETMY surface.

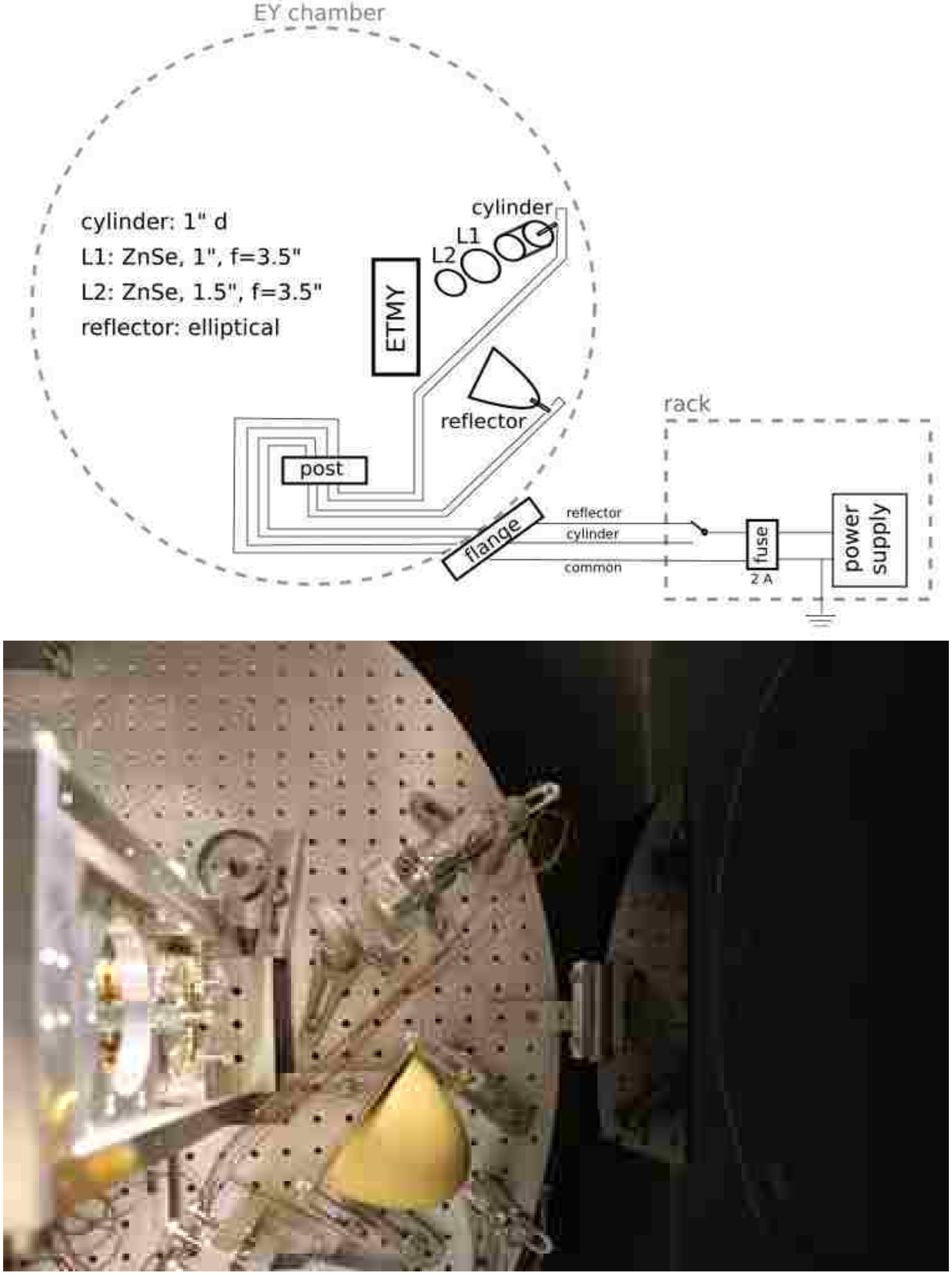

Figure 6.6. The installed set-up in the Yend vaccuum chamber. The reflector set up is closer to the bottom, and the lens setup above it; the IFO arm extend to the right. In the photo, the ETMY suspension cage and test mass are on the left.

reflector setup, respectively. The design layout and final in-vacuum setup are shown in Fig. 6.6. Both setups use a ceramic heating rod - 30 mm long, 3.8 mm diameter - as the heating element and are designed to project different heating patterns onto the test mass surface. The cylinder setup is shown in Fig. 6.5: the heating element sits inside of a metal cylinder and the heat field passes through two focusing lenses before hitting the test mass, ideally projecting a multiple-ring bullseye heating pattern on the optic. The reflector setup is an elliptical reflector with the tip of the heating rod placed at the first focus of the ellipse. This projects a point source pattern - see Fig. 6.7 - on the test mass with a different width than that of the central beam heating pattern.

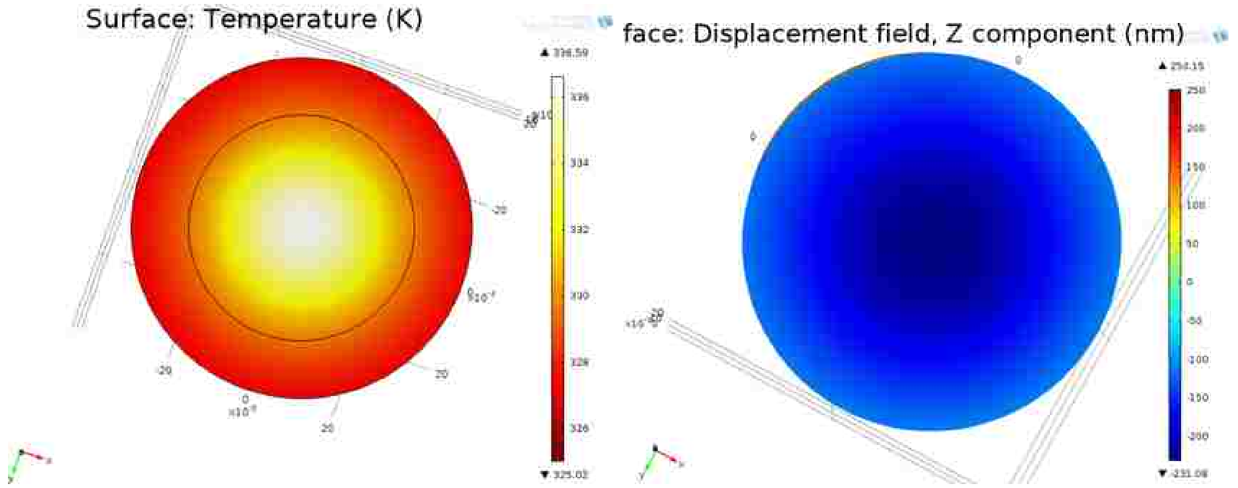

Figure 6.7. COMSOL simulation of temperature and displacement pattern on 40 m IFO ETM from reflector heating set-up, assuming 1 W absorbed power.

A simulation was made to study the change that the reflector setup could induce on the radius of curvature of the ETM. A non-sequential ray tracing software (Zemax) was used to calculate the heat pattern. An elliptical reflector with a radiative element inside it (simulating the real rod-heater, 30 mm long, 3.8 mm diameter) was drawn in CAD, placed in such a way that the heater tip is as close as possible to the ellipse first focus. Placing a screen at the second focus of the ellipse (where the mirror HR surface would sit), the projected heat pattern was found. In order to compute the mirror deformation induced by this kind of pattern, the map produced with Zemax was input as an absorption map in COMSOL. We considered ∼1 W total power absorbed by the mirror (just to have a unitary number). The mirror temperature and deformation maps induced by this heat pattern are shown in Fig. 6.7. To evaluate the RoC change, the RoC was fit over a circle of radius:

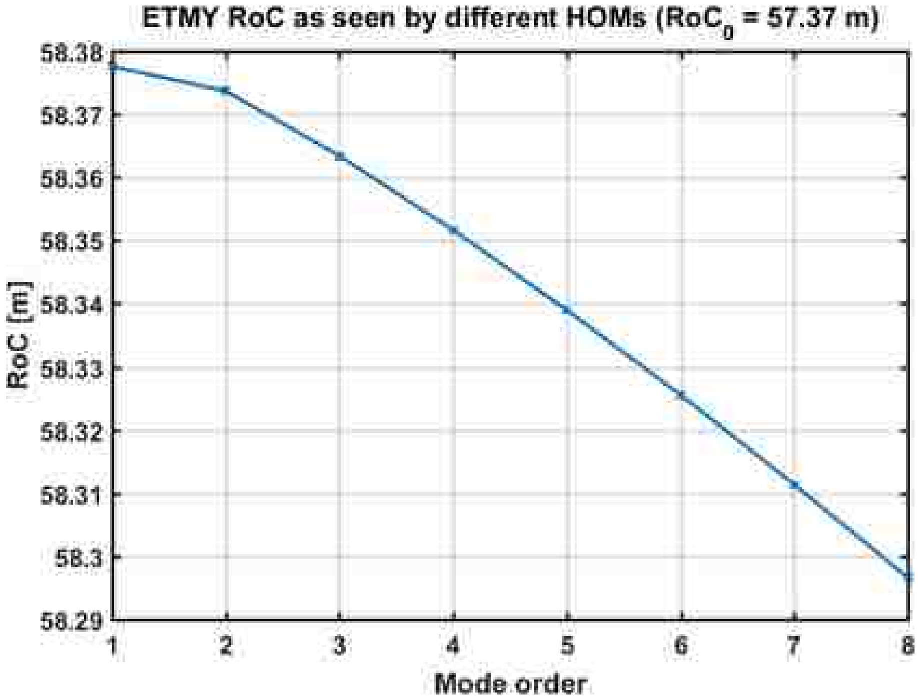

Figure 6.8. The radius of curvature as 'seen' by each HOM circulating in the cavity. The radius of curvature of the cold mirror is set to be 57.37 m.

$r = w_{00} \times \sqrt{n}$ where w_{00} is the waist of tha Gaussian mode on the ETMY (5 mm) and n is the mode order. This is a way to approximate the RoC as "seen" by each HOM, and is shown in Fig. 6.8 (the RoC of the cold mirror is set to be 57.37 m). Note that besides being very small (¡1%), the difference in RoC strongly depends on the heat pattern. Considering this absorbed power, the cavity Gouy phase variation between hot and cold state is roughly 15 kHz.

Prior to install, heating calibration measurements were performed with a power meter. Cold resistance of the heater was 3.5 Ohms. Power measurements are summarized in Table 6.2.

6.3 Results

The installed heating setups successfully induced deformation in the optic, particularly the reflector setup, and the arm cavity scans resolved higher order mode frequency shifts. We completed multiple scans at different heating powers for the reflector set up and witnessed

Table 6.2. Heater calibration measurements.

current [A]	voltage [V]	power [mW]	resistance [Ohm]
0.5	2.2	20	4.4
0.8	6	120	7.5
1	11	400	11
1.2	18	970	15

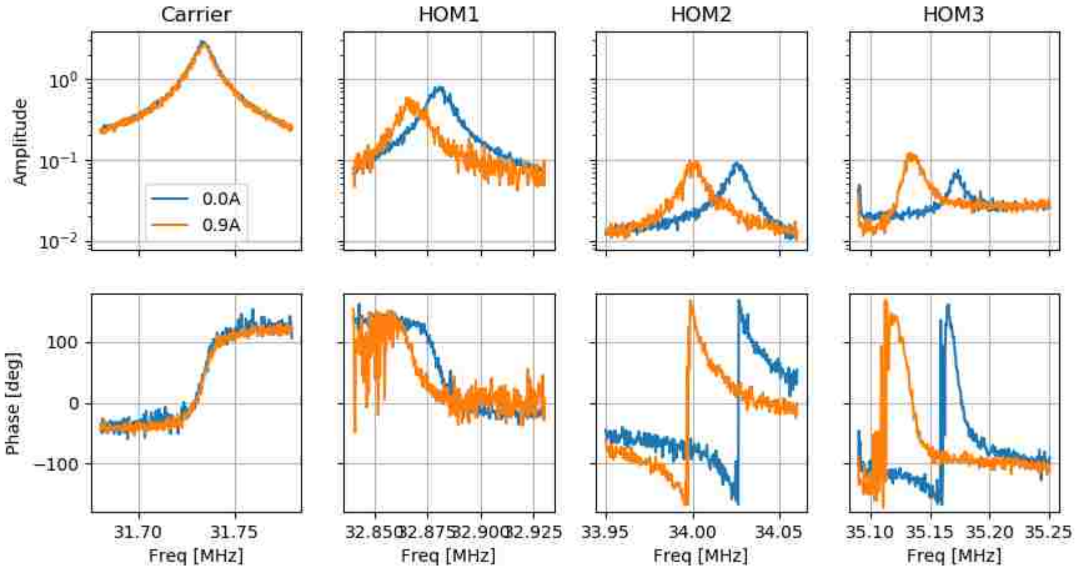

Figure 6.9. Example of shifting higher order mode peaks with and without projected heating (0 and 0.9 A driving the heating element) with the reflector setup. Scans with no projected heating pattern shown in blue. Scans with 9.0 A power on the reflector setup shown in orange.

HOMs shift down in frequency relative to cold by tens of kHz. An example of arm cavity scan transfer function around the carrier and first few HOMs is shown in Fig. 6.9, with 0.9 A powering the reflector setup. From heating calibration, this is about 260 mW incident on the test mass.

We also completed scans at cold and 0.9 A heating current to the cylinder setup. We witnessed only minimal (∼kHz) frequency shift, attributable to the poor focal plane location and large losses in the setup relative to the reflector setup.

Peak shift results from both setups are shown in Fig. 6.10, which plots the transverse mode spacing (TMS) divided by the mode order of scans up through HOM5. This presentation

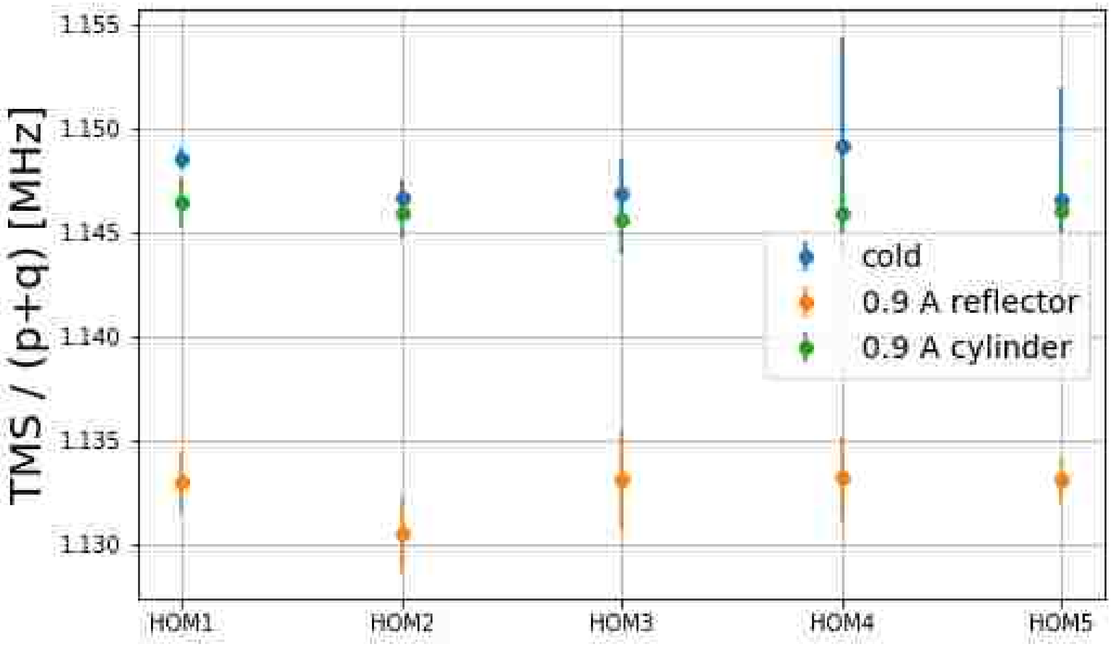

Figure 6.10. Results of scans up through HOM5 for cold, reflector, and cylinder setup.

allows us to see variations from a purely spherical optic, for which each mode in a given setup would have the same y-value. The overall shift - exemplified by the orange reflector data - shows the change in overall radius of curvature induced by the heater. From these measurements, the reflector setup increased the radius of curvature of the ETMY from 60.8 [60.6, 61.0] m to approximately 61.8 [61.6, 62.1] m. There is evidence of a unique shift of HOM2, but the uncertainty is still too large to make this claim.

Power to the reflector heater was increased in steps to find the minimum heater power required to see frequency shifts with the measurement setup. Lowest resolved was a shift in HOM3 with 1.7 W (0.5 A/3.4 V) power to the heater. According to Table 6.2, this is approximately 30-60 mW radiated power hitting the test mass.

In order to measure realistic in-situ mirror map deformations, much higher precision mode frequency measurement is required. For example, point absorbers currently in LIGO cause <10 nm distortion; this would require resolution on the order 10^{-4} Hz to resolve. The goal of this experiment is to determine the limit of mirror deformation resolution using this mode spectroscopy technique.

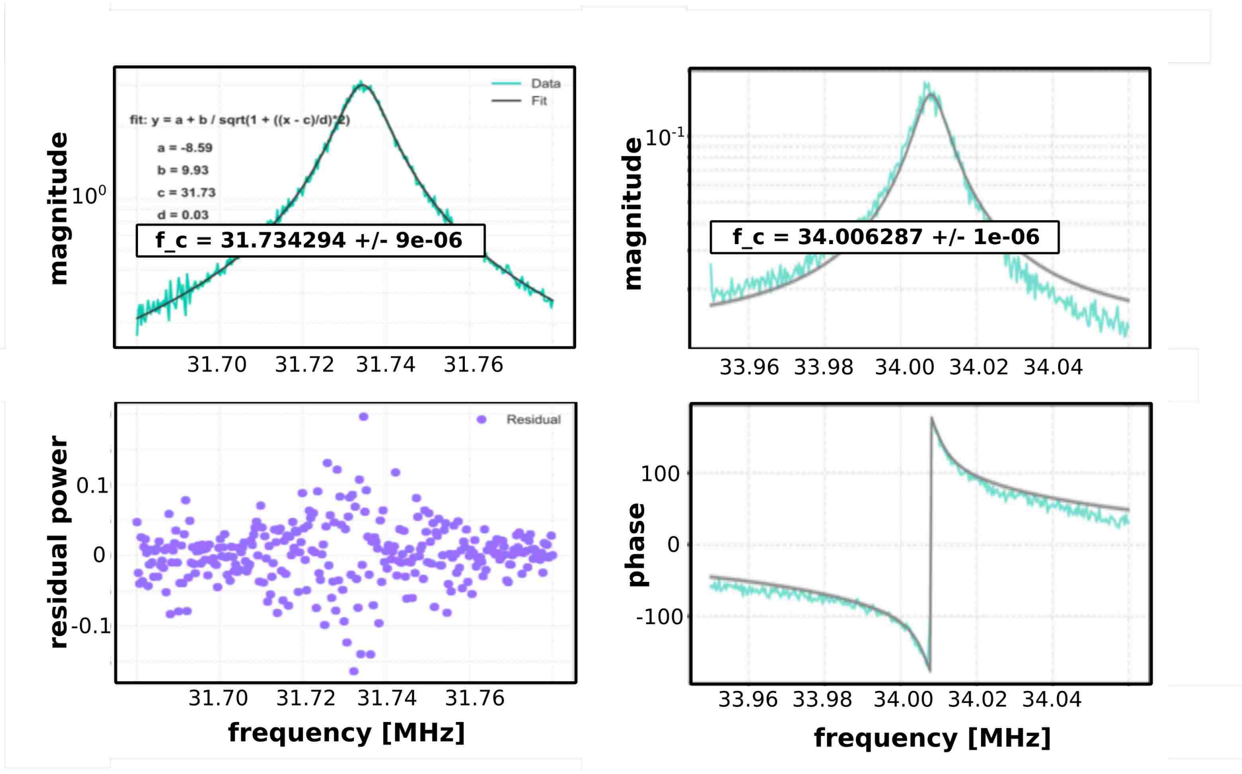

Figure 6.11. Left: Lorentzian fit to a HOM1 peak during the reflector setup measurement. Resolution of approximately 10 Hz is obtained. Right: Complex fit to a HOM2 peak during the same setup. Resolution of 1 Hz is obtained.

To decrease the uncertainty of measurements, multiple scans are merged and fit with resonance model. First, just the magnitude of the transfer function around each peak was fit with a Lorentzian, exemplified in Fig. 6.11. This fitting gives approximately 10 Hz resolution, which can detect changes up to around 10^{-3} m in radius of curvature. Fitting the full complex data of a HOM resonance has an uncertainty of approximately 1 Hz, which resolves radius of curvature variance to around 10^{-4} m. The fitting process is still underway, so we do not present a full analysis with this resolution here.

6.4 Future work

Finesse is an optical simulation software. An ideal 40 m arm cavity will be simulated in Finesse with no figure error and the same parameters as the 40m prototype interferometer.

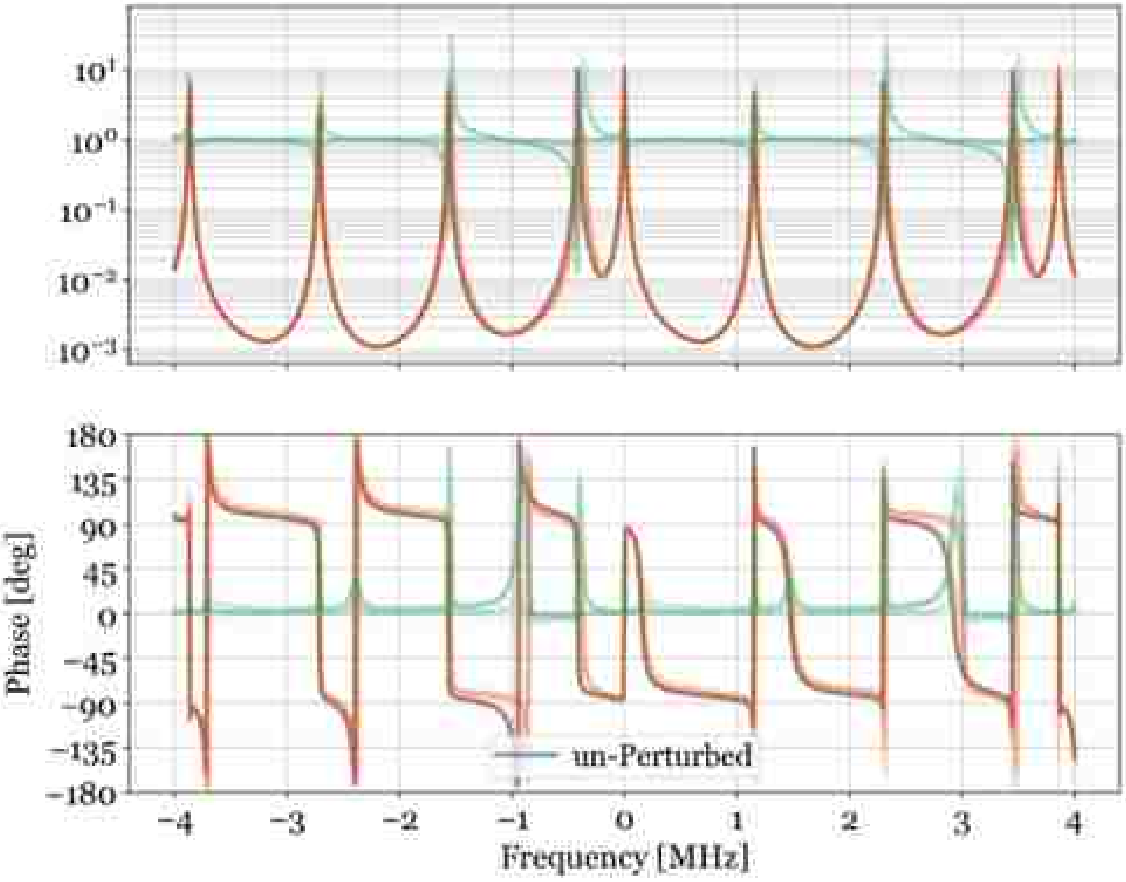

Figure 6.12. Simplified Finesse simulation of single arm 40 m cavity, with mirror map as input. The mirror map can consist of any combination of Zernike polynomials. An example Finesse scan output with and without additional perturbed mirror map inserted.

Zernike polynomials will be used to build a library of surface map models, which are then inserted into the ETMY model, the cavity is scanned, and we build a subsequent library of cavity scan simulations based on mirror error inputs, see Fig. 6.12. The simulated transverse mode spacings will be compared to the modes obtained experimentally to analyze the shift in the higher order modes and suggest a mirror map.

7 Conclusion

In this work we presented the need for increased power in the Advanced LIGO detectors to decrease quantum shot noise and increase the detectors' strain sensitivity above 100 Hz. To achieve this, we discuss the installation and successful commissioning of a new amplification system that provided 50 W input power to the interferometers during the third observing run, allowing a circulating arm power of approximately 250 kW. We confirm that the new system does not add significant additional laser noise that could otherwise pollute the sensitivity of the detector.

We discuss the thermal effects that arise with high circulating power impinging on the main optics in the interferometer. Uniform and point absorption lead to mode mismatch and scatter, both which cause loss in the optical system and decrease sensitivity and can increase laser noise coupling to differential length readout. We review the system in place to counter these effects and present measurements to minimize coupling.

We detailed three-mode opto-mechanical interactions that become unstable with increased power in the interferometer, called parametric instabilities. We step through the mitigation schemes that have been designed and successfully used during the past two observing runs, including the limits of each scheme and the projection of success to full aLIGO design sensitivity power.

Finally, we developed a test to measure cavity optical content dependence on mirror deformation. While results are still preliminary, they indicate the ability to control unique higher order mode resonances via controlled radiative heating. We demonstrate 1 Hz resolution of optical resonance peaks with the measurement and analysis technique.

Overall, the work presented here contributed to the successful operation of the aLIGO detectors during the third observing run, achieving a strain sensitivty better than $2 \times 10^{-20}\,\mathrm{m/Hz^{1/2}}$ during O3. Input power was increased from 25 W to 40 W, improving high frequency sensitivity by approximately ×1.3. With the broadband high frequency improvements from increased power and squeezing, combined with various noise mitigation, the binary neutron star inspiral range increased from ∼90 Mpc to 140 Mpc between O2 and O3.

References

[1] P.R. Saulson. *Fundamentals of Interferometric Gravitational Wave Detectors.* World Scientific, 1994.

[2] C. W. Misner, K. S. Thorne, and J. A. Wheeler. *Gravitation.* 1973.

[3] Nelson Christensen. Stochastic gravitational wave backgrounds. *Reports on Progress in Physics*, 82(1):016903, Nov 2018.

[4] J. Aasi, J. Abadie, B. P. Abbott, R. Abbott, T. Abbott, M. R. Abernathy, T. Accadia, F. Acernese, C. Adams, T. Adams, and et al. Gravitational waves from known pulsars: Results from the initial detector era. *The Astrophysical Journal*, 785(2):119, Apr 2014.

[5] B. P. Abbott, R. Abbott, T. D. Abbott, M. R. Abernathy, F. Acernese, K. Ackley, C. Adams, T. Adams, P. Addesso, R. X. Adhikari, and et al. First search for gravitational waves from known pulsars with advanced ligo. *The Astrophysical Journal*, 839(1):12, Apr 2017.

[6] B. Abbott and et al. Upper limits on gravitational wave bursts in ligo's second science run. *Phys. Rev. D*, 72:062001, Sep 2005.

[7] E. Hall. *Long-baseline interferometry for the detection of binary black-hole mergers.* PhD thesis, California Institute of Technology.

[8] D. Martynov. *Lock Acquisition and Sensitivity Analysis of Advanced LIGO Interferometers.* PhD thesis, California Institute of Technology.

[9] J Aasi et. al. Advanced LIGO. *Classical and Quantum Gravity*, 32(7):074001, Mar 2015.

[10] B. P. Abbott and et al. Observation of gravitational waves from a binary black hole merger. *Phys. Rev. Lett.*, 116:061102, Feb 2016.

[11] B.P. Abbott, R. Abbott, T.D. Abbott, S. Abraham, F. Acernese, K. Ackley, C. Adams, R.X. Adhikari, V.B. Adya, C. Affeldt, and et al. Gwtc-1: A gravitational-wave transient catalog of compact binary mergers observed by ligo and virgo during the first and second observing runs. *Physical Review X*, 9(3), Sep 2019.

[12] LIGO and Virgo Collaborations. https://gracedb.ligo.org/latest/.

[13] D. V. Martynov and E. D. Hall. Sensitivity of the advanced ligo detectors at the beginning of gravitational wave astronomy. *Phys. Rev. D*, 93:112004, Jun 2016.

[14] Tobin T Fricke, Nicols D Smith-Lefebvre, Richard Abbott, Rana Adhikari, Katherine L Dooley, Matthew Evans, Peter Fritschel, Valery V Frolov, Keita Kawabe, Jeffrey S Kissel, and et al. Dc readout experiment in enhanced ligo. *Classical and Quantum Gravity*, 29(6):065005, Feb 2012.

[15] Carlton M. Caves. Quantum-mechanical radiation-pressure fluctuations in an interferometer. *Phys. Rev. Lett.*, 45:75–79, Jul 1980.

[16] M. Tse and et al. Quantum-enhanced advanced ligo detectors in the era of gravitational-wave astronomy. In preparation.

[17] LIGO Collaboration. https://www.ligo.caltech.edu/LA/page/ligo-technology.

[18] E J Daw, J A Giaime, D Lormand, M Lubinski, and J Zweizig. Long-term study of the seismic environment at ligo. *Classical and Quantum Gravity*, 21(9):22552273, Apr 2004.

[19] Jan Harms. Terrestrial gravity fluctuations. *Living Reviews in Relativity*, 18(1), Dec 2015.

[20] S. Gras, H. Yu, W. Yam, D. Martynov, and M. Evans. Audio-band coating thermal noise measurement for advanced ligo with a multimode optical resonator. *Physical Review D*, 95(2), Jan 2017.

[21] R. Dolesi, M. Hueller, D. Nicolodi, D. Tombolato, S. Vitale, P. J. Wass, W. J. Weber, M. Evans, P. Fritschel, R. Weiss, and et al. Brownian force noise from molecular collisions and the sensitivity of advanced gravitational wave observatories. *Physical Review D*, 84(6), Sep 2011.

[22] M. E. Zucker and S. E. Whitcomb. Measurement of Optical Path Fluctuations due to Residual Gas in the LIGO 40 Meter Interferometer. In R. T. Jantzen, G. Mac Keiser, and R. Ruffini, editors, *Proceedings of the Seventh Marcel Grossman Meeting on recent developments in theoretical and experimental general relativity, gravitation, and relativistic field theories*, page 1434, 1996.

[23] L Barsotti, M Evans, and P Fritschel. Alignment sensing and control in advanced LIGO. *Classical and Quantum Gravity*, 27(8):084026, apr 2010.

[24] D. V. Martynov, V. V. Frolov, S. Kandhasamy, K. Izumi, H. Miao, N. Mavalvala, E. D. Hall, R. Lanza, B. P. Abbott, R. Abbott, and et al. Quantum correlation measurements in interferometric gravitational-wave detectors. *Physical Review A*, 95(4), Apr 2017.

[25] M. Heintze and T. Hardwick. LLO alog: `https://alog.ligo-la.caltech.edu/aLOG/index.php?callRep=36824`.

[26] M. Heintze. LLO alog: `https://alog.ligo-la.caltech.edu/aLOG/index.php?callRep=44607`.

[27] M. Heintze and T. Hardwick. LLO alog: `https://alog.ligo-la.caltech.edu/aLOG/index.php?callRep=43644`.

[28] A. Effler. LLO alog: `https://alog.ligo-la.caltech.edu/aLOG/index.php?callRep=46009`.

[29] T. Hardwick. LLO alog: `https://alog.ligo-la.caltech.edu/aLOG/index.php?callRep=47476`.

[30] A. Brooks. LLO alog: `https://alog.ligo-la.caltech.edu/aLOG/index.php?callRep=46090`.

[31] Aidan F. Brooks, Benjamin Abbott, Muzammil A. Arain, Giacomo Ciani, Ayodele Cole, Greg Grabeel, Eric Gustafson, Chris Guido, Matthew Heintze, Alastair Heptonstall, Mindy Jacobson, Won Kim, Eleanor King, Alexander Lynch, Stephen O'Connor, David Ottaway, Ken Mailand, Guido Mueller, Jesper Munch, Virginio Sannibale, Zhenhua Shao, Michael Smith, Peter Veitch, Thomas Vo, Cheryl Vorvick, and Phil Willems. Overview of advanced ligo adaptive optics. *Appl. Opt.*, 55(29):8256–8265, Oct 2016.

[32] R Lawrence. *Active wavefront correction in laser interferometric gravitational wave detectors*. PhD thesis, Massachusetts Institute of Technology, 2003.

[33] Kiwamu Izumi. Frequency response of the aligo interferometery, Dec 2015. LIGO technical document T1500461: `https://dcc.ligo.org/LIGO-T1500461/public`.

[34] G. Vajente. In situ correction of mirror surface to reduce round-trip losses in fabry–perot cavities. *Appl. Opt.*, 53(7):1459–1465, Mar 2014.

[35] Daniel Vander-Hyde. Conditioning ring heater actuator input to optimize thermo-optic response, Aug 2019. LIGO technical document T1900496: `https://dcc.ligo.org/LIGO-T1900496/public`.

[36] Aidan Brooks. LIGO Livingston alog: `https://alog.ligo-la.caltech.edu/aLOG/index.php?callRep=48796`.

[37] A. Alloca. *Thermal projection system for surface figure correction of core optics in Gravitational Waves interferometers*. PhD thesis, Universit'a degli Studi di Siena.

[38] Terra Hardwick. LIGO Livingston alog: `https://alog.ligo-la.caltech.edu/aLOG/index.php?callRep=48651`.

[39] T. Hardwick. LLO alog: `https://alog.ligo-la.caltech.edu/aLOG/index.php?callRep=48151`.

[40] Terra Hardwick. LIGO Livingston alog: `https://alog.ligo-la.caltech.edu/aLOG/index.php?callRep=43245`.

[41] Terra Hardwick Carl Blair. LIGO Livingston alog: `https://alog.ligo-la.caltech.edu/aLOG/index.php?callRep=43270`.

[42] Terra Hardwick. LIGO Hanford alog: `https://alog.ligo-wa.caltech.edu/aLOG/index.php?callRep=41490`.

[43] Carl Blair. LIGO Livingston alog: `https://alog.ligo-la.caltech.edu/aLOG/index.php?callRep=38445`.

[44] Aidan Brooks. LIGO Livingston alog: `https://alog.ligo-la.caltech.edu/aLOG/index.php?callRep=37793`.

[45] Carl Blair, Slawek Gras, Richard Abbott, Stuart Aston, Joseph Betzwieser, David Blair, Ryan DeRosa, Matthew Evans, Valera Frolov, Peter Fritschel, et al. First demonstration of electrostatic damping of parametric instability at advanced ligo. *Physical review letters*, 118(15):151102, 2017.

[46] S. Biscans, S. Gras, C. D. Blair, J. Driggers, M. Evans, P. Fritschel, T. Hardwick, and G. Mansell. Suppressing parametric instabilities in ligo using low-noise acoustic mode dampers, 2019.

[47] Terra Hardwick, Vahid Hamedan, Carl Blair, Anna Green, and Daniel Vander-Hyde. Demonstration of dynamic thermal compensation for parametric instability suppression in advanced ligo. *In preparation.*

[48] M Evans, L Barsotti, and P Fritschel. A general approach to optomechanical parametric instabilities. *Physics Letters A*, 374(4):665–671, 2010.

[49] J. Miller, M. Evans, L. Barsotti, P. Fritschel, M. MacInnis, R. Mittleman, B. Shapiro, J. Soto, and C. Torrie. Damping parametric instabilities in future gravitational wave detectors by means of electrostatic actuators. *Physics Letters A*, 375:788–794, January 2011.

[50] V Jaberian Hamedan, C Zhao, L Ju, C Blair, and D G Blair. Suppression of thermal transients in advanced LIGO interferometers using CO2 laser preheating. *Classical and Quantum Gravity*, 35(11):115006, may 2018.

[51] Comsol multiphysics reference manual. COMSOL, Inc, `www.comsol.com`.

[52] Jérôme Degallaix. OSCAR a matlab based optical FFT code. *Journal of Physics: Conference Series*, 228:012021, May 2010.

[53] Aidan F. Brooks. Results from thermal compensation system testing in the one arm test, Oct 2012. LIGO technical document T1200465: `https://dcc.ligo.org/LIGO-T1200465/public`.

[54] Slawomir Gras, Chunnong Zhao, DG Blair, and Li Ju. Parametric instabilities in advanced gravitational wave detectors. *Classical and Quantum Gravity*, 27(20):205019, 2010.

[55] AC Green, DD Brown, M Dovale-Álvarez, C Collins, H Miao, CM Mow-Lowry, and A Freise. The influence of dual-recycling on parametric instabilities at advanced ligo. *Classical and Quantum Gravity*, 34(20):205004, 2017.

[56] Daniel David Brown and Andreas Freise. Finesse, May 2014. You can download the binaries and source code at `http://www.gwoptics.org/finesse`.

[57] Anna Catriona Green. *When light gets pushy: radiation pressure effects in interferometric gravitational wave detectors.* PhD thesis, University of Birmingham, 2018.

[58] Patrice Hello and Jean-Yves Vinet. Analytical models of transient thermoelastic deformations of mirrors heated by high power cw laser beams. *J. Phys. France*, 51:2243–2261, 1990.

[59] Chunnong Zhao, Li Ju, Qi Fang, Carl Blair, Jiayi Qin, David Blair, Jerome Degallaix, and Hiroaki Yamamoto. Parametric instability in long optical cavities and suppression by dynamic transverse mode frequency modulation. *Phys. Rev. D*, 91:092001, May 2015.

[60] L Ju, C Zhao, D G Blair, S Gras, S Susmithan, Q Fang, and C D Blair. Three mode interactions as a precision monitoring tool for advanced laser interferometers. *Classical and Quantum Gravity*, 31(18):185003, aug 2014.

[61] David Blair, Li Ju, ChunNong Zhao, LinQing Wen, HaiXing Miao, RongGen Cai, JiangRui Gao, XueChun Lin, Dong Liu, Ling-An Wu, ZongHong Zhu, Giles Hammond, Ho Jung Paik, Viviana Fafone, Alessio Rocchi, Carl Blair, YiQiu Ma, JiaYi Qin, and Michael Page. The next detectors for gravitational wave astronomy. *SCIENCE CHINA Physics, Mechanics and Astronomy*, 58(12):120405, 2015.

[62] Slawek Gras, Peter Fritschel, Lisa Barsotti, and Matthew Evans. Resonant dampers for parametric instabilities in gravitational wave detectors. *Physical Review D*, 92(8):082001, 2015.

[63] Nesbitt W Hagood and Andreas von Flotow. Damping of structural vibrations with piezoelectric materials and passive electrical networks. *Journal of Sound and Vibration*, 146(2):243–268, 1991.

[64] Bernard Jaffe. *Piezoelectric ceramics*, volume 3. Elsevier, 2012.

[65] T. Hardwick. LLO alog: `https://alog.ligo-la.caltech.edu/aLOG/index.php?callRep=41520`.

[66] Patrick Biscan, Slawek Gras, Carl Blair, Jenne Driggers, Matthew Evans, Peter Fritschel, Terra Hardwick, and Georgia Mansell. *In preparation.*

[67] Craig Cahillane, Joe Betzwieser, Duncan A. Brown, Evan Goetz, Evan D. Hall, Kiwamu Izumi, Shivaraj Kandhasamy, Sudarshan Karki, Jeff S. Kissel, Greg Mendell, Richard L. Savage, Darkhan Tuyenbayev, Alex Urban, Aaron Viets, Madeline Wade, and Alan J. Weinstein. Calibration uncertainty for advanced ligo's first and second observing runs. *Phys. Rev. D*, 96:102001, Nov 2017.

[68] A. Allocca, A. Gatto, M. Tacca, R. A. Day, M. Barsuglia, G. Pillant, C. Buy, and G. Vajente. Higher-order laguerre-gauss interferometry for gravitational-wave detectors with in situ mirror defects compensation. *Phys. Rev. D*, 92:102002, Nov 2015.

[69] Zom-B at en.wikipedia. https://commons.wikimedia.org/w/index.php?curid=15880824.

[70] Fulda P. Bond C. Brueckner F. Brown D. Wang M. Lodhia D. Palmer R. Freise A. Carbone, L. The generation of higher-order laguerre-gauss optical beams for high-precision interferometry. *J. Vis. Exp.*, 78:e50564, 2013.

Vita

Terra Hardwick received her bachelor's degree from the University of Oregon, majoring in mathematics and physics. During her time there, she worked in Schofield's ant lab and spent summer and winter breaks working at the LIGO Hanford Observatory. She chose to pursue her PhD at Louisiana State University to work as a commissioner at the LIGO Livingston Observatory. Terra and her cat live in a self-made jungle and enjoy kayaking the bayou.